Terahertz Spectroscopy and Modelling of Biotissue

by

Gretel Markris Png

Bachelor of Engineering (Electrical and Electronics Engineering, First Class Honours),
The University of Edinburgh, Scotland, UK, 1997

Master of Science (Electrical Engineering and Computer Science),
University of California at Irvine, USA, 2003

Thesis submitted for the degree of

Doctor of Philosophy

in

School of Electrical and Electronic Engineering,
Faculty of Engineering, Computer and Mathematical Sciences
The University of Adelaide, Australia

June, 2010

Chapter 1

Introduction and Motivation

MEDICALLY inspired terahertz (THz) research has enormous potential but it faces tremendous challenges due to the inherent complexity of biological systems, such as human tissue. Furthermore, many well-established diagnostic tools cannot be adapted immediately to suit the THz frequency range, thus medical terahertz research often entails the extra challenge of either adapting existing medical tools using innovative ideas, or inventing novel ones. A melding of disciplines—engineering, mathematics, biology, physics and chemistry—is needed to push medical THz research towards robust, reliable, affordable and practical clinical use.

This Thesis brings together the fields of mathematical modelling, spectroscopic analysis of biological tissue, and the manufacture and tests of synthetic biological systems. The body of work covered in this Thesis details the novel preparation techniques needed to make repeatable experiments with biological tissue, and the mathematical modelling and signal processing techniques required to enhance the detected signal. The Thesis culminates with the presentation and discussion of a potential practical application of THz spectroscopy in understanding the pathology of Alzheimer's disease.

1.1 Introduction

In this chapter, an introduction to terahertz (THz) technology is first provided, followed by a brief history of medical and biological THz research. The motivation for the work presented in this Thesis is then presented, followed by an outline of the chapters in this Thesis. This chapter concludes with a concise summary of the novel contributions made to the field of medically inspired THz research.

1.2 What is Terahertz?

Terahertz radiation (THz or T-ray, 1 THz = 10^{12} Hz) is a type of electromagnetic radiation that spans the gap between microwave and infrared radiation. Although typically defined as the range between 100 GHz and 10 THz, frequencies up to 40 THz have sometimes been included in the THz range. As shown in Fig. 1.1, the upper and lower limits of the THz range overlap the microwave and infrared spectra, hence low-frequency THz is also referred to as submillimeter waves, whilst high-frequency THz is also referred to as far-infrared (FIR).

Terahertz shares some of the properties of microwave and infrared radiation, but also has benefits that the others lack. For example, like microwave radiation, pulsed THz signals have good temporal resolution. However pulsed THz has better spatial resolution than microwave radiation. Furthermore, as shown in Fig. 1.1, the photon energy of THz ($\approx 10^{-3}$ eV) is almost six orders of magnitude lower than radiation that is ionising, such as X-rays. At this low 10^{-3} eV photon energy level, provided power levels are below levels that cause heating, THz is considered safe for prolonged use on living biotissue. When THz transmits through (or is reflected from) a sample, the emerging signal contains coherent spectroscopic information about the sample at terahertz frequencies (Siegel 2004). This means that THz can capture the characteristic resonance *fingerprint* attributed by a sample's large-scale molecular structure (Fischer *et al.* 2005a).

1.3 The Historical Landscape of Terahertz Technology

"...standing on the shoulders of giants."

Sir Isaac Newton (1643–1727)

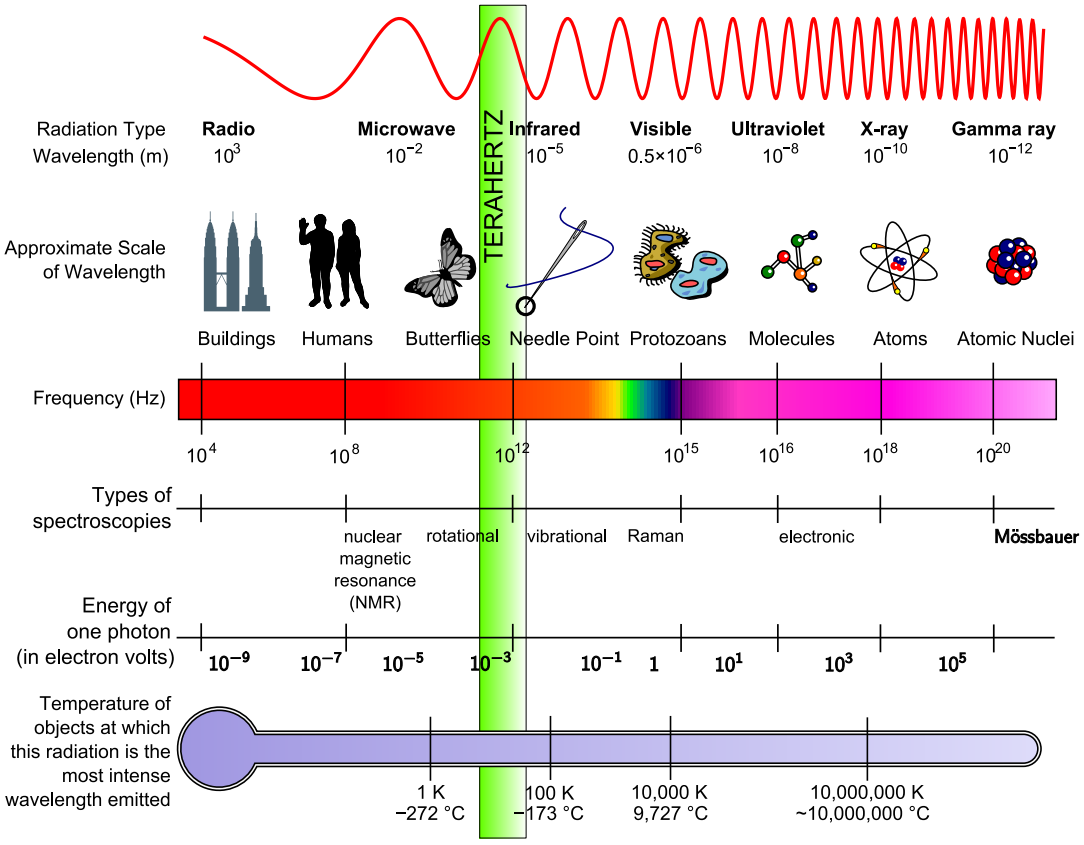

Figure 1.1: Electromagnetic spectrum. Electromagnetic spectrum showing a pictorial view of the relative size of the various wavelengths. Adapted from Wikipedia (2008a), Hore (1995), and the Advanced Light Source (ALS) (1996). Note that throughout the electronic version of this Thesis, the colour green is used to depict THz radiation; the choice of colour is for illustrative purposes only.

1.3.1 The Forebears of Terahertz Technology

The term *terahertz* is a relatively new moniker for a frequency range that has been of interest to astrophysicists since the advent of modern spectroscopic techniques in the mid 1920s. One of the first uses of the word *terahertz* was by Senitzky and Oliner (1970) in a review of submillimeter waves: the 100 GHz to 10,000 GHz frequency range that contains a wealth of information about the composition of interstellar bodies such as dust clouds. Astrophysicists at the time used (and continue to use) the term *submillimeter waves* to refer to this range of frequencies that have allowed humans to use spectroscopic techniques to examine celestial bodies millions of light years away.

Submillimeter wave spectroscopy is by no means limited to the astrophysical arena. The study of the composition of interstellar bodies requires a solid understanding of

molecular chemistry, hence many molecular spectroscopists have been and still are actively involved in submillimeter wave research. Molecular spectroscopy has a rich history dating to before the middle of the 19th century when Joseph von Fraunhofer created a crude spectrometer to study sunlight; his apparatus generated the first spectral fingerprints of chemical elements—a finding unfortunately unknown to Fraunhofer himself because he died before more studies could be carried out. However Fraunhofer's groundbreaking work was continued by Gustav Kirchhoff and Robert Bunsen in 1859. With the help of a very strong gas flame (the Bunsen burner), they discovered the unique spectrum of every chemical element known at the time. This heralded the birth of molecular/astronomical spectroscopy.

Interest in molecular spectroscopy after 1859 came unsurprisingly from astronomers because of the Sun's reliability as a bright light source. The field blossomed in the late 19th century with advancement in the engineering of spectroscopic hardware, such as Henry Rowland's diffraction grating. By 1933, molecular spectroscopy of gas had evolved into microwave gas spectroscopy when Claud Cleeton and Neal H. Williams from the University of Michigan obtained the first absorption spectrum of ammonia gas between 7.5 and 30 GHz through the use of a magnetron radiation source (Cleeton and Williams 1933, Cleeton and Williams 1934). The novelty of Cleeton and Williams' work was the frequency range that their microwave equipment could achieve, which hitherto was only available up to 3.33 GHz. Their work paved the development of microwave technology, which symbiotically benefited the study of molecules and their constituents in the microwave frequency range.

The pace of microwave spectroscopy accelerated significantly after the Second World War with the advent of masers and subsequently lasers. Charles Townes, who was one of several advocates of microwaves, pioneered the maser in 1954 while at Columbia University in New York. In 1958, Townes and Arthur Schawlow proceeded to theoretically extended masers into the optical and infrared range—the concept of the laser[1] was born. In 1960, Theodore Maiman from Hughes Research Laboratories demonstrated the first working laser (Maiman 1960a, Maiman 1960b). Laser technology would become instrumental in the development of terahertz technology: the discovery

[1]The first recorded use of the acronym LASER was by Gordon Gould, a student at Columbia University. Gould fought a controversial thirty-year battle over patents for laser and laser-related technologies. Although he largely won the battle, his claim as the inventor of the laser is still disputed (Bromberg 1991).

of optical harmonics in nonlinear materials in 1961 (Section 3.2), and 26 years later in David H. Auston's development of the first laser-based THz emitter (Section 1.3.2).

Spectroscopists from a non-microwave (and often non-astronomical) background were also interested in the infrared (IR) range. The IR range has a much longer history than submillimeter waves and can be traced back to Sir Frederick William Herschel, who in 1800 discovered IR radiation (Herschel 1800c, Herschel 1800a, Herschel 1800b). Spectroscopists working in the IR range in the 19th century were often interested in studying the interaction of common minerals with IR radiation, hence they were continually exploring experimental techniques to extend the boundaries of the IR range. Their efforts were limited by the intensity of the Sun until the development of artificial intense light sources, such as the quartz mercury arc. In 1897, Heinrich Rubens and Ernest Nichols utilised a zirconium burner to generate IR radiation with wavelengths in the range of 18 μm (Rubens and Nichols 1897a, Rubens and Nichols 1897b). Unbeknownst to them, this was the earliest report of far-infrared/terahertz generation.

Although the generation of IR radiation was possible by 1897, its detection was still a challenge. Grating-based detectors and heat sensitive bolometers that were introduced in the late 19th century were often cumbersome or required the use of complex conversion formulae (e.g. echelette grating). These detectors were deemed slow by Marcel Golay in 1949, who then proceeded to introduce a more responsive multi-slit, pneumatic-based spectrometer: the Golay cell. These detectors enabled the first exploration of the far-infrared range as early as 1950 (McCubbin Jr. and Sinton 1950). By 1957, research into the far-infrared had progressed to the extent that far-infrared interferometric telescopes mounted on balloons were being planned to sense the earth's atmosphere (Strong 1957).

Fifty-two years after the humble proposal of the far-infrared interferometric balloon telescope, the aptly named Herschel[2] Space Observatory, as shown in Fig. 1.2, was launched into space on the back of the Ariane 5 rocket in May 2009. Herschel carries a variety of spectrometers that covers the full far-infrared and submillimeter bands. Orbiting at 1.5 million kilometers away from the Earth until 2012, Herschel's spectroscopic measurements have begun arriving on earth for analysis, revealing spectacular spectroscopic information about the molecular chemistry of the early universe.

[2]Named after the 1800 discoverer of IR radiation, Sir Frederick William Herschel. In 1781, Herschel, with the help of his sister Caroline, discovered the planet Uranus—the first planet to be discovered using a telescope.

NOTE:
These figures are included on page 6 of the print copy of the thesis held in the University of Adelaide Library.

(a) (Left) Image of the completed Herschel spacecraft; (Right) Assembly process

(b) Cryostat inside telescope

(c) A single bolometer

NOTE:
These figures are included on page 6 of the print copy of the thesis held in the University of Adelaide Library.

(d) Terahertz spectral fingerprints of carbon monoxide from the Orion Bar

(e) Strong THz water resonance from Comet Garradd

Figure 1.2: The Herschel spacecraft. (a) (Left) A computer generated image of the entire Herschel spacecraft, with its telescope (antenna dish and mid portion), service module (base), sun shield/shade and solar panels; (Right) Assembly of the spacecraft. After the European Space Agency (2004). (b)The telescope contains a helium-cooled cryostat, on which the scientific instruments sit. After the European Space Agency (2007). (c) Scientific instruments consist of photodetector arrays and spectral/photometric imaging receivers sensitive in the far-infrared range. At the heart of this bolometer is a tiny crystal (the rectangle towards the bottom of the bolometer), which reacts to changes in temperature. After the SPIRE Consortium (2007). (d) Terahertz spectral fingerprints of carbon monoxide (CO) found inside the Orion Bar (a region in the Orion Nebula), detected by the SPIRE Fourier transform spectrometer onboard the Herschel spacecraft. Spectral fingerprints will be discussed in detail in Sections 4.2 and 4.3. After the European Space Agency and the SPIRE Consortium (2009b). (e) Detection of a strong water resonance in the THz frequency range from Comet Garradd, detected by the HIFI spectrometer onboard the Herschel spacecraft. After the European Space Agency and the HIFI Consortium (2009a).

Back on *terra firma*, the Atacama Large Millimeter Array (ALMA) as shown in Fig. 1.3 is scheduled for completion in 2012. It will consist of 66 interferometer antenna arrays built at an altitude of 5 km above sea level on the Chajnantor plateau in the Chilean Atacama Desert. ALMA's antennas will operate at wavelengths between 0.3 mm (1 THz) and 10 mm (0.03 THz), enabling scientists to detect "distant galaxies forming at the edge of the observable universe, which we see as they were roughly ten billion years ago" (the European Organisation for Astronomical Research in the Southern Hemisphere 2008b). The advancement of submillimeter wave research over the last five decades has been truly phenomenal.

NOTE:
These figures are included on page 7 of the print copy of the thesis held in the University of Adelaide Library.

(a) Site of ALMA in the Chilean Atacama Desert

(b) Transportation and docking of an interferometer array antenna

Figure 1.3: The ALMA interferometer antenna arrays. (a) Artist's impression of the ALMA site showing the interferometer antenna arrays. After the European Organisation for Astronomical Research in the Southern Hemisphere (2008a). (b) An antenna is placed with millimetric precision on a concrete docking pad. After the European Organisation for Astronomical Research in the Southern Hemisphere (2008c).

An excellent review of the rapid progress of astrophysical submillimeter wave technology can be found in Siegel (2007); a review of the history of millimeter and submillimeter development from 1890 to after 1965 can be found in Wiltse (1984), and a brief review of the history of THz sources from the 1890s to the 1970s can be found in Kimmit (2003) and Zhang and Xu (2010).

1.3.2 The Early Days of Terahertz Technology

Active research in the astrophysical submillimeter and far-infrared ranges has naturally spurred an interest in developing submillimeter/far-infrared emitters and detectors for use on Earth, with the purpose of probing chemical elements in order to

understand molecular motion and activation. As expected, many early pioneers were either trained in molecular spectroscopy, or in microwave engineering. However the hardware needed to generate submillimeter/far-infrared on Earth now required expertise from a new field: semiconductor physics. Submillimeter/far-infrared was now a multidisciplinary field and fittingly needed a new name: terahertz.

In the mid 1980s, New Jersey, USA was home to two active hubs of THz research: AT&T Bell Laboratories and IBM Watson Research Center. Bell Labs, with its long successful history in semiconductor physics, demonstrated the first photoconductive antenna in 1984. David H. Auston from Bell Labs, who had been researching switching effects (sampling) in electro-optic materials since 1972 (Glass and Auston 1972, Johnson and Auston 1975, Auston *et al.* 1978), first reported in 1983 on the generation of subpicosecond electro-optic shockwaves in nonlinear materials through the use of ultrafast laser pulses (Auston and Smith 1983). The next year, he and his colleagues successfully generated pulsed THz through electro-optic sampling when femtosecond optical pulses from a dye laser were propagated in lithium tantalate (Auston *et al.* 1984b, Auston and Cheung 1985). They then proceeded to utilise this new electro-optic sampling technique in a novel, compact coherent time domain detector that allowed the extraction of the optical properties of lithium tantalate without the need for the Kramers-Kronig relations (Cheung and Auston 1986). This new coherent time domain detector was a vast improvement to the existing bulky and less accurate spectrometers.

In the meantime, IBM Watson Research Center was involved, among other activities, in the development of fibre optics-based molecular spectroscopy (Grischkowsky 1980a, Grischkowsky 1980b). IBM's research included picosecond optoelectronics with emphasis on freely propagating optical pulses along transmission lines mounted on a dielectric substrate. In 1987, Daniel Grischkowsky *et al.* demonstrated the generation of electromagnetic shockwaves using the transmission line configuration—a benchmark validation of Auston's sampling technique. A year later, Christof Fattinger and Daniel Grischkowsky demonstrated the emission and detection of THz using their free propagation technique (Fattinger and Grischkowsky 1988).

The discoveries of Auston and Cheung, and Fattinger and Grischkowsky, were immensely important because there was a need to develop a new spectroscopic technique for the lower THz frequency range. Although microwave spectrometers and Fourier Transform Infrared (FTIR) spectrometers were already commonly used by the mid 1980s for detecting THz signals, neither technique is sensitive in the region between

0.1 THz and 10 THz. In 1989, the first significant demonstration of THz as a new time domain spectroscopic technique was performed by Martin van Exter *et al.* from IBM. Terahertz time domain spectroscopy (THz-TDS), which was then referred to as a "new high-brightness system", was used to measure the nine strongest lines of water vapour between 0.2 THz and 1.45 THz. The THz-TDS technique was a milestone in molecular spectroscopy because it enabled the calculation of absorption and dispersion of samples through Fourier analyses of time domain measurements. However it took another six years before the terahertz emission and detection techniques in THz-TDS would undergo a revolution: free-space electro-optic sampling of THz (Wu and Zhang 1995). While the idea of electro-optic sampling was not new, its use in the THz range was novel and exciting because hitherto there was a lack of appropriate optical hardware for the THz range. Zhang and Wu from Rensselaer Polytechnic Institute in New York introduced a new THz spectroscopic system that allowed the emitter and detector to be separated by 10 cm—a massive distance compared to the lithium tantalate-based systems of the late 1980s. The free-space THz system now rivalled FTIR spectrometers in terms of signal-to-noise ratio and ease of use, and an unprecedented interest in the THz regime by scientists from diverse technical backgrounds was unleashed.

One and a half decades later, interest in THz continues to flourish through the cutting-edge research work of a vibrant, international THz community. Although the bulk of THz research is still exploratory, a handful of THz applications are starting to emerge from behind the laboratory walls into the real-world. For example, security applications of THz have attracted immense interest with the global rise in terrorism, particularly post-September 11, 2001. The urgency to develop THz detection systems for hazardous chemicals and weapons concealed on the body led to a flurry of THz research activities across the world (Wang *et al.* 2002, Campbell and Heilweil 2003, Kemp *et al.* 2003, Choi *et al.* 2004, Min *et al.* 2004, Tribe *et al.* 2004, Shen *et al.* 2005a, Baker *et al.* 2005, Federici *et al.* 2005). Hidden weapons and illicit drugs embedded in soil or other buffer materials were also of interest (Kawase *et al.* 2003, Osiander *et al.* 2003, Dodson *et al.* 2005, Bosq *et al.* 2005). In 2008, the Department of Homeland Security in the USA contracted the development of a THz spectrometer for detecting hazardous chemicals in public places (THz Science and Technology Network 2008). Security-oriented THz applications have indeed matured, and THz detectors may in the very near future be used in everyday life.

Pharmaceutical THz applications are also gaining momentum particularly in non-destructive monitoring of the coatings of ingestible tablets (Fitzgerald *et al.* 2005, Zeitler *et al.* 2007, Spencer *et al.* 2008, Ho *et al.* 2008). Other non-destructive quality control applications involve polymer mixtures and cork enclosures for wine bottles (Rutz *et al.* 2006a, Rutz *et al.* 2006b, Wietzke *et al.* 2007, Hor *et al.* 2008). Non-destructive THz inspection has even been used in verifying authenticity in art (Jackson *et al.* 2008).

Terahertz research has also evolved beyond standard spectroscopy to encompass 2- and 3-dimensional imaging (Hu and Nuss 1995, Mittleman *et al.* 1996, Mittleman *et al.* 1999, Ciesla *et al.* 2000, Ferguson *et al.* 2002a, Crawley *et al.* 2003a, Crawley *et al.* 2003b, Nguyen *et al.* 2006, Fitzgerald *et al.* 2005, Zeitler *et al.* 2007), interferometric imaging (Johnson *et al.* 2001), tomography (Mittleman *et al.* 1997), computed tomography (Ferguson *et al.* 2002b), synthetic phased-array imaging (O'Hara and Grischkowsky 2002), and near-field microscopy (van der Valk and Planken 2004, von Ribbeck *et al.* 2008). The potential of earth-bound THz research is undoubtedly as limitless and exciting as its cosmic-gazing sibling, submillimeter waves.

1.4 Terahertz in Medicine and Biology

The broadband spectral features of chemical elements and solutions had been of interest to scientists before the advent of time domain THz spectroscopy in 1985. As highlighted in Section 1.3.1, molecular spectroscopists had been studying the infrared absorption properties of cosmic gases and chemical elements since the time of Fraunhofer in 1850. However it was only in 1900 that molecular activity, not atomic activity, was proposed by Knut Ångström as the cause of the unique spectral features of gases in the infrared frequency range (Ångström 1900). By measuring two gas compounds, each containing carbon and oxygen, Ångström obtained two differing infrared spectra. This led him to theorise that the difference must be attributed to vibrational-rotational activity of the oxygen and carbon molecules. This theory is still accepted today and is the basis of molecular and biological THz spectroscopy (Ogilvie 1989).

With the improvement in radiation sources in the early 20th century, the widening infrared range was loosely divided into four regions: near-infrared (780–3000 nm, 385–100 THz), mid-infrared (3000–6000 nm, 100–50 THz), far-infrared (6000–15000 nm, 50–20 THz), and ultra-far-infrared (15000–1 mm, 20–0.3 THz). The main far-infrared (FIR) sources before the mid-1950s were mercury arc lamps and harmonic generation from

high frequency oscillators such as klystrons, magnetrons and travelling-wave tubes (Yoshinaga *et al.* 1958, Ohl *et al.* 1959). Far-infrared spectroscopy of chemicals were conducted as early as 1930 when Czerny[3] extracted the optical properties of rock salt (sodium chloride) for the entire FIR range. By the 1950s, FIR transmission spectra had been reported for various materials including the atmosphere, solids (such as crystal quartz, paraffin, Teflon, and polyethylene), ammonia and hydrogen chloride (McCubbin Jr. and Sinton 1950). Despite these advances, there was still a need to improve the spectral resolution of the lower FIR region. The improvement arrived in the 1960s in the form of Fourier Transform Spectroscopy (FTS).

Fourier Transform Spectroscopy, a technique based on interferometry[4], was developed by P. B. Fellgett for his 1951 Thesis (Loewenstein 1966). It was extended into the far-infrared range by Randall (1954) and Strong (1957), and subsequently improved in 1964 by Richards to achieve high-resolution spectroscopy (Richards 1964). Fourier Transform Spectroscopy is present today in Fourier Transform Infrared (FTIR) spectrometers, which have evolved into affordable, compact, and reliable standard apparatus found in most molecular spectroscopy laboratories and security checkpoints. Modern FTIR spectrometers are capable of generating a wide range of infrared frequencies by selecting the appropriate emitter-detector crystal pair. Higher far-infrared frequencies above 12 THz are attainable but cooling of the emitter and detector with liquid helium is needed. Frequencies below 12 THz are not readily available in FTIR spectrometers due to the limited frequency sensitivity of existing hardware, such as beamsplitters. For example, potassium bromide (KBr)—a common material used in beamsplitters—is only sensitive down to $\approx$ 10.5 THz, whereas cesium iodide (CsI) is sensitive down to $\approx$ 6.75 THz (Perkin Elmer Inc. 2008, Varian Inc. 2008). Terahertz time domain spectroscopy (THz-TDS) is therefore still one of the most reliable techniques for generating broadband THz[5].

[3]It is interesting to note that Czerny used the German word *ultraroten* (the ultrared) to refer to his far-infrared work that included frequencies below 10 THz—a testament of the lack of a universal nomenclature for the infrared range.

[4]Interferometry has its own rich history dating back to 1862 when Armand Hippolyte Louis Fizeau demonstrated through the use of Newton's rings that yellow sodium radiation was a doublet (Fizeau 1862).

[5]Other THz generation techniques are described in Chapter 2.

1.4.1 Terahertz Sensing of Proteins

Terahertz sensing of proteins has been one of the most interesting applications of THz spectroscopy. *Sensing* is a term often used interchangeably with *detection*, however terahertz sensing of proteins is more closely associated with the study of the structural dynamics inside a protein crystal. Like in FTIR protein studies, samples used in THz-TDS systems usually contain small quantities of pure protein powder that are mixed with a filling material such as polyethylene, and then pressed into thin pellets. When a pure protein is illuminated by broadband THz, its internal molecular vibration acts like a filter in preventing certain THz frequencies from reaching the THz detector. As a result, these absent frequencies are apparent as distinct *absorption* peaks in the processed (detected) signal. This phenomenon is in complete agreement with Ångström's theory of molecular activity (Section 1.4), and is immensely useful in identifying subtle structural differences in proteins. For example, a racemic mixture containing enantiomers of a chiral molecule[6] has different absorption spectral peaks in the THz range from the individual enantiomers, allowing for distinction between racemic mixtures and pure enantiomers (Franz *et al.* 2006).

A detailed description of THz protein sensing is provided in Chapter 4. In summary, THz time domain spectroscopy has been used to study deoxyribonucleic acid (DNA) and ribonucleic acid (RNA) (Markelz *et al.* 2000, Brucherseifer *et al.* 2000, Fischer *et al.* 2002, Nagel *et al.* 2003, Globus *et al.* 2003, Fischer *et al.* 2005b, Parthasarathy *et al.* 2005, Globus *et al.* 2006), protein binding (Chen *et al.* 2007b), protein conformation modes (Castro-Camus and Johnston 2008), protein dynamics (Mourant *et al.* 2001, Walther *et al.* 2002, Markelz *et al.* 2007, Knab *et al.* 2007, Yamaguchi *et al.* 2007), and protein sequence (Ebbinghaus *et al.* 2008).

1.4.2 Terahertz Sensing of Biotissue

The success of THz protein studies has spurred the use of THz in more complex biological materials such as skin, organs, and teeth. Like pure powdered proteins, the proteins in complex biological materials should in theory also generate unique spectral peaks (fingerprints) in the THz frequency range. If a protein changes chemically

[6]Two proteins that share the same chemical composition but are non-superimposable mirror-images of each other are said to have opposite chirality, or left- and right-handedness. Such proteins are enantiomers.

and/or structurally due to a disease such as cancer, its THz fingerprint should alter, creating an identity marker for the disease. Markers for diseases are undoubtedly critical for medical diagnosis, with new disease markers constantly being sought to improve the quality of disease management. Terahertz has the potential to create new markers. If medically and commercially viable, THz imaging and spectroscopic tools could in the near future complement existing imaging modalities such as X-ray, magnetic resonance imaging (MRI) and computed tomography (CT).

Early THz research into biotissue and complex biological systems in the mid and late 1990s did indeed put an emphasis on THz as an imaging tool to rival X-ray, MRI and CT. The first 2-dimensional THz images of a biological sample (a fresh leaf) were presented by Bin Bin Hu and Martin C. Nuss[7] of AT&T Bell Laboratories (1995). These images are reproduced in Fig. 1.4. This was the first demonstration of the use of THz transmission spectroscopy in conjunction with a x-y stage to achieve raster scanning. As seen in Fig. 1.4, the resolution of the images is sufficient to distinguish between the various parts of the leaf, hence providing convincing proof of the viability of THz imaging. In addition, changes in water content over time were also captured in the images because of terahertz radiation's extreme sensitivity to water, demonstrating the usefulness of THz as a monitoring tool for quality control. These properties of THz were further emphasised by Daniel Mittleman *et al.* in 1996 when THz transmission imaging was applied to molded plastic sheets interleaved with foam (Mittleman *et al.* 1996). Bubbles inside the foam, which cause mechanical failure, cannot be picked up by X-ray inspection but convincingly appear as regions of contrast in the terahertz frequency range. Mittleman *et al.* also went on to show the application of THz imaging to a gaseous sample, and proposed the use of THz in monitoring the recovery progress of burn wounds (Mittleman *et al.* 1996).

In 1997, Mittleman *et al.* extended the use of THz imaging to include reflection-mode inspection, specifically tomography (Mittleman *et al.* 1997). Reflection-mode inspection is particularly beneficial for samples that are either very thick or have very high water content (both properties cause strong THz absorption). The same year, a report in the *Laser Focus World* magazine described Rensselaer Polytechnic Institute's THz imaging work of the internal organs of a ladybird (Appell 1997). By 1999, THz imaging had been successfully applied to many novel biological scenarios: detection of dental

[7] The term *T-rays* was coined by Hu and Nuss (1995).

NOTE:
This figure is included on page 14 of the print copy of the thesis held in the University of Adelaide Library.

Figure 1.4: Study of leaf hydration using THz. Contrast between the two terahertz images of a leaf is due to differences in water content over time. The right image is that of the leaf after drying for 48 hours. After Hu and Nuss (1995).

caries inside a tooth (Fig. 1.5(b)); examination of enamel thickness of a tooth; differentiation between muscle, fat, and organ in pork; and three dimensional tomographic mapping of skin surfaces (Arnone *et al.* 1999). A separate study of excised chicken, beef and pork samples showed distinction between the meat samples in the THz frequency range (Mittleman *et al.* 1999). The resolution of THz imaging was also shown to be sufficient to identify small masses in a sample, such as almonds in a chocolate bar (Fig. 1.5(a)), and cancerous masses in a mammographic phantom (Chen *et al.* 1999). These exciting discoveries of the late 1990s ensured that medical THz imaging was on its way to becoming a *bona fide* medical imaging modality.

The lessons learnt from medical THz research in the 1990s paved the way for more ambitious work in the new millennium. Terahertz's sensitivity to water coupled with low power from existing free-space THz-TDS systems makes it unviable for transmission through samples with high water content, such as the human body. With the development of higher power systems in the future, full body THz imaging may be possible; this will be discussed in Chapter 9.

Given THz-TDS's current capability, medical THz research has focused on two types of biotissue: that close to the surface of the body (namely skin), and excised. The aim of many bodies of work was to demonstrate the contrast between excised biotissue types when imaged with THz, thus providing a means of optically analysing the health of a biotissue (Knobloch *et al.* 2001, Löffler *et al.* 2001, Fitzgerald *et al.* 2002, Knobloch

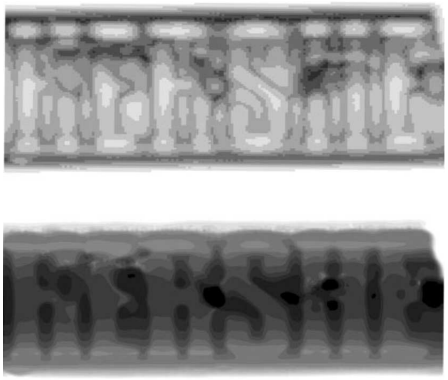

(a) Transmitted THz amplitude (top) and phase (bottom) information through a chocolate bar

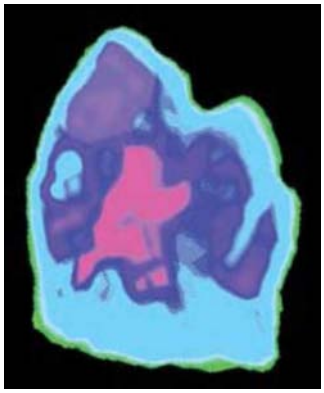

(b) Three-dimensional THz tomograph of a human tooth

Figure 1.5: Chocolate causes cavity? (a) One of the most well-known THz images is this Hershey chocolate bar containing almonds. After Mittleman *et al.* (1999). (b) Pink pseudocolour highlights a region of strong THz absorption, indicative of the presence of pulp in a dental cavity. After Arnone *et al.* (1999), coloured image after Mueller (2003).

et al. 2002, Siebert *et al.* 2002b, Siebert *et al.* 2002a, Löffler *et al.* 2004). An example is presented in Fig. 1.6. Differences between the THz spectroscopic signal from THz-TDS systems was also used to study differences between optical properties of biotissue types (Berry *et al.* 2003a, Fitzgerald *et al.* 2003). Another area of interest was classifying excised biotissue types with the aim of developing automated THz inspection systems (Ferguson and Abbott 2001, Ferguson *et al.* 2002a, Handley *et al.* 2002, Löffler *et al.* 2002).

NOTE:
These figures are included on page 15 of the print copy of the thesis held in the University of Adelaide Library.

(a) Optical image

(b) Terahertz image

Figure 1.6: Identification of tumours in formalin-fixed liver. (a) Two-dimensional terahertz images of formalin-fixed liver with several tumours. (b) The tumours can be identified from the darker regions. After Knobloch *et al.* (2001).

The discoveries highlighted in the previous paragraph all involved excised biotissue, which poses several challenges for THz measurements. These challenges will be highlighted in Section 1.5 and discussed in detail in Chapter 4. In order for THz to complement X-ray, MRI and CT, a non-invasive technique had to be developed. One such technique was introduced in 2001 by Cole *et al.* who demonstrated the inspection of human skin with a THz-TDS system in reflection mode. Differing spectroscopic measurements and 2-dimensional images were obtained from dry and hydrated skin. This technique now provided a means of *in vivo* inspection of skin and its disorders, such as skin cancer, thus spurring an interest in the interaction of THz with skin cancer. In 2002, Woodward *et al.* successfully applied (transmission-mode) THz imaging to excised human skin samples and showed (Fig. 1.7) that regions containing basal cell carcinoma (BCC) could be clearly identified in the THz frequency range (Woodward *et al.* 2002, Woodward *et al.* 2003a, Woodward *et al.* 2003b). The prospect of developing a reflection-mode THz scanning system for skin diseases and other diseases close to the surface of the skin became extremely promising.

NOTE:
These figures are included on page 16 of the print copy of the thesis held in the University of Adelaide Library.

(a) Optical image of excised human biotissue

(b) THz images reveal diseased regions

Figure 1.7: Identification of skin cancer. (a) The diseased biotissue is on the left and is outlined by the solid boundary. The healthy biotissue on the right is outlined by the dashed boundary. (b) THz measurements reveal regions where the time domain signals are broadened more significantly than usual. These regions, marked by the squares labelled d1 and d2, correspond to regions on the diseased side of the biotissue. After Woodward *et al.* (2003b).

A reflection-mode hand-held scanning tool as shown in Fig. 1.8 has indeed been developed commercially by TeraView Ltd. in Cambridge, UK (Baker *et al.* 2004). This system has been reported to successfully detect hidden weapons and drugs under clothing. Its fibre-coupled hand-held wand is suited for scanning the surface of the skin in order to

inspect the health of moles. With further advancement in the miniaturisation of THz hardware, this system could eventually be compact, light, and robust enough for use in hospitals and clinics.

Figure 1.8: Portable THz technology. Terahertz scanning system with a hand-held fibre-coupled wand. After Baker *et al.* (2005).

1.5 Motivation for Thesis

From the first 2-dimensional THz image of a leaf in 1995 (Hu and Nuss) to the development of a hand-held scanning system in 2004 (Baker *et al.*), bio-inspired THz research has evolved and continues to attract strong interest worldwide. New THz applications continue to be reported alongside novel measuring techniques such as synthetic phased-array imaging (O'Hara and Grischkowsky 2002), computed tomography (Ferguson *et al.* 2002b), and near-field microscopy (van der Valk and Planken 2004, von Ribbeck *et al.* 2008). Past discoveries have also been repeated and refined in order to improve the reliability of measurements. For example, research into THz spectroscopy and imaging of basal cell carcinoma (BCC) has evolved and improved to incorporate histological verification (Wallace *et al.* 2004, Pickwell *et al.* 2005, Wallace *et al.* 2006).

Researchers are also seeking a deeper understanding of the fundamental interaction of THz with biotissue so as to interpret empirical results. This is paramount because of the complex nature of biotissue which contains structures that can alter or occlude the detected THz signal. These structures include stratified biotissue layers, blood vessels, and hair follicles.

Understanding the fundamental interaction of THz with biotissue is the first motivation for this Thesis. The second motivation for this Thesis is to contribute towards the pool of new medical THz applications.

1.5.1 Motivation 1: Interaction of Terahertz with Biotissue

A small number of studies have been conducted by other authors on the interaction of THz with matter. Duvillaret *et al.* (1996, 2001) have created several models of THz interaction with matter. The focus of their work was in parameterisation of measured THz data, i.e. the extraction of the complex refractive index. Dorney *et al.* (2000) looked into multiple internal reflections of THz in a sample, where the reflections are described by the Fabry-Pérot effect. Their work focused on interferometric methods of removing background reflection as well as the parameterisation of measured THz data. Their work is important for the understanding of THz, but it does not fully address how THz interacts with heterogeneous media.

Mathematical models have also been designed to simulate the transmission of THz through water and biological layers (Walker *et al.* 2003, Pickwell *et al.* 2004a, Pickwell *et al.* 2004b, Walker *et al.* 2004, Pickwell *et al.* 2005). Modelling techniques include thin film matrix, Monte Carlo, Cole-Cole, and Finite Difference Time Domain. This Thesis will expand on mathematical modelling to elucidate THz transmission, reflection and scattering. Novel techniques for removing reflections embedded in the THz signal will also be presented.

Analysis of the simpler synthetic analogues of biotissue has also been performed. Hydration of a burn dressing containing collagen, a component of skin, has been studied with THz in order to ascertain if the burn dressing is a suitable skin phantom in the THz frequency range (Corridon *et al.* 2006). This Thesis will present original THz analysis of simple cultured biological systems containing layered structures. Hydration changes in excised biotissue have also been studied and will be presented in this Thesis. This includes novel work on the effect of necrosis in biotissue on the measured THz signal.

1.5.2 Motivation 2: Sensing the Pathogens of Alzheimer's Disease

Alzheimer's disease (AD) is caused by an abnormal, accelerated accumulation of large quantities of assorted proteins in the brain. The protein clumps (or *senile plaques*) usually congregate on the outermost surface of the brain, blocking the electrical signals passed between synapses. Severe blockage causes symptoms such as memory loss and reduced motor skills. Over time, an AD-afflicted brain also shrinks in size and when combined with acute loss in motor skills, death eventuates.

The proteins that are present in senile plaques are known to medical science and can be synthesised *ex-vivo* individually. Either collectively or individually, unique THz fingerprints would in theory exist for these proteins. By probing these proteins with THz, we may be able to establish a deeper understanding of the triggers that transform normal proteins into senile plaques, and possibly also identify potential antigens that could be introduced into the body to slow, stop or alter these undesirable transformations.

Novel THz sensing work will be presented in this Thesis involving excised AD-afflicted brain cores as well as one protein, β-lactoglobulin (β-lg), which can be synthesised into structures similar to that of senile plaques.

1.6 Outline of Thesis

The overarching theme of this Thesis is improved understanding of biotissue through THz spectroscopic studies of biotissue, with the aim of broadening the application of THz in medicine. The resulting research encompasses multiple fields that initially appear disparate: from mathematically modelling based on the the fundamentals of Maxwell's laws of electromagnetics, to the biology of the brain; from nonlinear optics, to designing recipes for manufacturing synthetic protein structures. This Thesis aims to weave these fields together to create a body of work where a synthesis between the fields is evident, and where THz spectroscopy is the common thread running through each Chapter. A structural flow chart of this Thesis is presented in Fig. 1.9.

In this Chapter, the historical landscape of THz, current state of knowledge of medical and biological THz research, motivations and key contributions of this Thesis are given. The historical landscape is an attempt to pay homage to the pioneers of THz, but many pioneers involved in developing the hardware and detection techniques used in THz science have not yet been acknowledged. Therefore Chapters 2 and 3 aim to meld

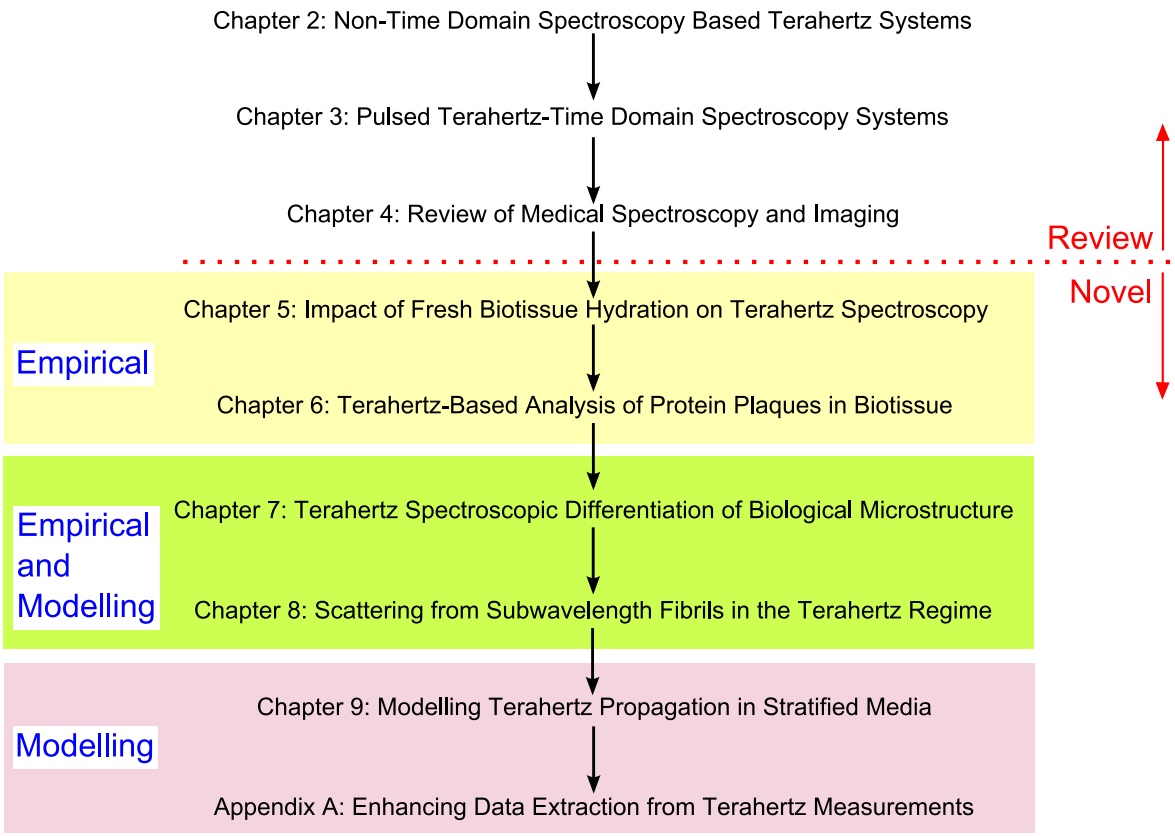

Figure 1.9: Thesis structural flow chart. This flow chart highlights the flow of Chapters in this Thesis. The Thesis begins with a thorough literature review of existing work related to this Thesis; the review is covered by the Chapters depicted above the dotted line. Original contributions are presented in the Chapters and one Appendix depicted below the dotted line. This chart also indicates if the emphasis of each novel Chapter is on empirical findings, or on modelling, or both.

history into the presentation of specialised THz hardware and detection techniques, including THz generation techniques distinct from the terahertz time domain system (THz-TDS) mentioned earlier in Sections 1.3.2 and 1.4.

Having highlighted the tools of THz science, an introduction to past and present medical and biological applications of THz, infrared and microwaves is fitting. Chapter 4 presents the methodology and samples used in these applications, and discusses the implications of their results. Chapter 4 also includes a brief histological description of biotissue and salient histopathological information on diseases encountered in THz studies.

Novel THz experiments are presented from Chapter 5 onwards. In Chapter 5, a thorough investigation involving excised rat biotissue is presented. This investigation

monitors the effect of biotissue hydration and freshness on measurements. Fresh and necrotic biotissue samples are compared to identify spectral differences. Lyophilisation (freeze drying) is then introduced as a viable solution for overcoming hydration, thickness, freshness, structural-preservation, and handling problems.

From the experience gained from handling fresh biotissue in Chapter 5, this Thesis proceeds to investigate healthy and diseased excised human brain tissue for the purpose of ascertaining if THz spectroscopy can be used to post-identify protein plaques associated with Alzheimer's disease (AD). In Chapter 6, snap-frozen human brain samples are obtained from a brain bank. Diseased samples are neuropathologically diagnosed as containing abnormally high numbers of protein plaques consistent with AD. Measurement of frozen samples have reduced uncertainties caused by the presence of water, aiding in revealing possible collective vibrational modes of the protein plaques in the THz frequency range. Results show some distinction in the THz absorption spectra, which could be attributed to pathological changes in the diseased tissue.

Although the results in Chapter 6 are encouraging, the complexity and variability of biotissue raises questions with regards to the accuracy and repeatability of THz measurements. Questions also arise with regards to identifying which specific component(s) of a diseased biotissue actually distinguishes it from a healthy sample in the THz frequency range; the collective response of all components in biotissue appears to be the determining factor. To gain a deeper insight into the pathogenesis of Alzheimer's disease, Chapter 7 narrows the focus down to one of the alleged pathogens of Alzheimer's disease: protein plaques. The unique β-pleated structure of protein plaques is one of its most distinguishable features, thus this Chapter investigates whether this biological microstructure can be differentiated using THz spectroscopy. The results reveal differences between spherical and fibrillar microstructures, which have several exciting implications for THz spectroscopy as the fibrillar microstructures contain β-pleated sheets resembling those in Alzheimer's disease. This means that it is possible to use THz spectroscopy to identify protein plaques in brain tissue if the tissue is devoid of blood vessels and other granular matter. Isolating protein plaques is realistically possible, but will require large quantities of biotissue. Before embarking on such an endeavour, it is useful to first gain an understanding of how THz radiation interacts with fibrillar structures.

Chapter 8 presents a study of fibrillar (cylindrical) sub-wavelength structures. Such structures occur frequently in either natural or artificial forms, such as in protein

plaques and as strands of hair and fabric. The prevalence of fibrillar structures raises the question of how THz radiation interacts with these structures, specifically the extent of scattering. Understanding scattering is crucial in many potential THz applications which rely on the detection of reflected/scattered THz signals, such as *in vivo* skin cancer detection, quality control, and security. Analytical (exact) models and a full-wave electromagnetic field numerical solver are presented to elucidate novel THz measurements of arrays of fibreglass strands with known alignment, allowing for the characterisation of a generic fibrillar structure in the THz frequency range. Although the full-wave electromagnetic field simulator adds an extra dimension of information to THz-TDS measurements, its use can have drawbacks. The pros and cons of utilising a full-wave electromagnetic field simulator is discussed in this Chapter.

Chapter 9 is also related to the simulation of THz interaction with matter, but utilises a simple yet effective analytical model instead of a full-wave electromagnetic field simulator. This Chapter explores THz propagation in stratified heterogeneous media akin to those in biotissue, particularly the head. The interest in THz propagation through layers of the head stems from the earlier work involving Alzheimer's disease in order to explore the possibility of performing *in vivo* THz sensing of protein plaques in the brain. This study requires biological optical properties that are scarce in the THz frequency range, hence this study delves into the material parameters available in the infrared and microwave frequency ranges, revealing the rich body of biologically inspired work carried out at these frequencies. This study closes the link the connects THz, infrared and microwave medical research.

Finally, Chapter 10 concludes this Thesis with a summary of outcomes from the novel work presented in Chapters 5–9, and recommendations are proposed for future extension of the work presented here. Four novel case studies that aim to improve the extraction of information from THz measurements are included in Appendix A as part of the recommendations for future work.

1.6.1 Summary of Contents in Appendices

Eight appendices are included in this Thesis to supplement the materials presented in Chapters 1–10. In Appendix A, four small preliminary studies are presented as part of the recommendations for future work in Chapter 10.

In Appendix B, provides a brief overview of the terms and conventions used to describe nonlinearity, which is introduced in Chapter 3. Appendix B also gives an overview of THz-related crystals that have nonlinear properties. The dependence of THz electro-optic (EO) generation on the geometries and orientations of nonlinear crystals is highlighted.

Appendix C lists the equipment used in the various THz-TDS systems used to conduct the experiments reported in Chapters 5–8.

Appendix D presents the mathematical derivation of the complex refractive index, which is introduced in Chapter 5. The mathematical derivation is given in the context of polar molecules.

Appendix E supplements the discussion on dementia in Chapter 6 by reproducing one popular neuropsychological test, the Modified Mini Mental State (3MS) Examination. This is done to highlight some of the difficulties in catering to all demographics. Examples of dementia types are also provided in this Appendix.

Appendix F presents the derivations of scattering-related equations used in Chapters 7 and 8. Other scattering models highlighted in Chapter 8 are also discussed briefly. In addition, an example of the use of one such model to study the impact of skin surface roughness in the THz regime is presented.

Appendix G presents the derivation of the general solution of the Helmholtz equation as required in Chapter 9.

Appendix H provides a list of the filenames of the MATLAB source code used to generate results in Chapters 5–9, and Appendix A of this Thesis. The purpose of the different MATLAB files, and the related Chapters in this Thesis are highlighted. The full code is available in the enclosed CD-ROM. Where applicable, extracts of the full code are presented in this Appendix to highlight notable steps undertaken in data processing.

1.7 Original Contributions

This Thesis makes several original contributions towards understanding the fundamental interaction of THz with biotissue and expanding the pool of new medical THz applications.

The study in Chapter 5, which explores hydration and storage issues in freshly excised biotissue, is important as it highlights the susceptibility of THz biotissue measurement

to changes in environmental conditions and measurement duration (Png *et al.* 2008a). This study is the first of its kind to highlight the need for storage and handling protocols in the area of THz biotissue measurements. This work was performed in collaboration with Jin-Wook Choi, a medical doctor in Xi-Cheng Zhang's Center for Terahertz Research, at Rensselaer Polytechnic Institute, USA. Samples were obtained from Ian Guest at the Wadsworth Center (NYS Department of Health, Albany, USA).

Based on the experience gained from the study in Chapter 5, Chapter 6 presents a study that is novel in two aspects: the use of snap-frozen biotissue , and the investigation of the plausibility of utilising THz sensing for distinguishing between healthy and Alzheimer's disease-afflicted human brain tissue (Png *et al.* 2009c, Png *et al.* 2009b). Samples from this study are obtained from the South Australian Brain Bank at Flinders University.

In order to focus the study of Alzheimer's disease down to one of its pathogens, the study in Chapter 7 required expertise in the field of biochemistry. In collaboration with Anton Middelberg's team at the Australian Institute of Nanotechnology at the University of Queensland, we were able to meld our THz and biochemistry expertise into demonstrating, at the University of Adelaide, that THz spectroscopy can be used to non-destructively differentiate between soft protein microstructures containing features of one of the known fibrillar pathogens of Alzheimer's disease (Png *et al.* 2009a).

Following the observation of fibrillar (cylindrical) and spherical distinction with THz spectroscopy, questions were raised with regards to the interaction of THz radiation with fibrillar microstructures. Well-controlled THz measurements of fibreglass arrays were conducted using Robert Miles' THz facility at the Institute of Microwaves and Photonics, the University of Leeds, UK. As shown in Chapter 8, these measurements revealed these arrays to have interesting optical properties. In order to elucidate these measurements, analytical and numerical models were applied to study scattering from cylindrical scatterers (Png *et al.* 2008b).

Chapter 9 presents a mathematical study of THz propagation through stratified heterogeneous media (Png *et al.* 2005b, Png *et al.* 2005a, Withayachumnankul *et al.* 2007). This study utilises a simple yet effective analytical model to elucidate THz propagation, and aids in the determining the plausibility of conducting *in vivo* THz sensing of diseased biotissue located several millimeters beneath the skin.

Finally, four novel short preliminary studies are presented in Appendix A as part of the recommendation for future work. These four studies are conducted with two aims:

(i) to improve the extraction of information from THz measurements (Png *et al.* 2004), and *(ii)* to improve the modelling of THz propagation and scattering from biotissue.

The original contributions of this Thesis, including those in collaboration with others, serve to advance the goal of developing potentially ground-breaking THz medical diagnostic tools that are robust, reliable and preferably non-invasive, with the aim that these tools will one day complement existing imaging and spectroscopic modalities.

Chapter 2

An Overview of Terahertz Systems: Part 1

TERAHERTZ (THz) radiation can be generated as either a pulsed or a continuous wave (CW) signal. A pulsed THz signal is broadband, i.e. the application of the Fourier transform on its temporal form produces a spectral waveform containing a wide range of frequencies, typically between 0.1 and 4 THz for laser-based THz systems. Conversely, CW THz radiation only contains one frequency, but a CW THz system can include tuning components that allow it to operate at one of several discrete CW frequencies.

The fundamental generation and detection techniques behind pulsed and CW THz systems are very different, hence each system type deserves a dedicated Chapter of its own. This Chapter focuses on CW THz systems, but also includes pulsed THz systems that do not rely on electro-optic (EO) or photoconductive (PC) THz generation, such as synchrotrons. The depth of coverage in this Chapter is less thorough than in Chapter 3, where pulsed THz-time domain spectroscopy (TDS) systems based on EO and PC THz generation/detection are discussed. This is because all measurements presented in this Thesis are conducted on pulsed EO/PC THz-TDS systems, necessitating discussion of the EO/PC techniques to a far greater extent. Nonetheless, this Chapter highlights the variety, scope, and history of CW and non EO/PC pulsed THz systems in order to show that these systems are integral to the modern THz landscape.

Acronyms related to THz systems

BBO	beta barium borate
BWO	backward-wave oscillator
CO_2	carbon dioxide
CW	continuous wave
DFG	difference frequency generation
DNA	deoxyribonucleic acid
EO	electro-optic
FEL	free electron laser
FIR	far-infrared
FTIR	Fourier Transform Infrared
GaP	gallium phosphide
HeNe	helium-neon
ITER	(formerly) International Thermonuclear Experimental Reactor
JET	Joint European Torus
OPO	optical parametric oscillator
OPTL	optically pumped THz lasers
PC	photoconductive
QCL	quantum cascade laser
RF	radio frequency
RNA	ribonucleic acid
RPI	Rensselaer Polytechnic Institute
SEM	scanning electron micrograph
SFG	sum frequency generation
TDS	time domain spectroscopy
YAG	yttrium aluminium garnet

2.1 Systems Not Based on EO/PC THz Generation

Terahertz systems that do not rely on electro-optic (EO) or photoconductive (PC) THz generation are extremely varied in their size, operating conditions (e.g. output power, frequency), and applications. This Chapter introduces non-EO/PC-based systems that range from the tiny (quantum cascade lasers a few hundred microns in size) to the

massive (synchrotrons the size of a sports playing field). Many of these systems generate either continuous wave (CW) THz radiation, or pulsed THz radiation. A handful of systems can generate both CW and pulsed THz radiation. This Chapter also includes an overview of the hardware and respective measurement techniques used in generating and detecting THz radiation from these non-EO/PC-based systems.

2.2 Continuous Wave THz Generation

The THz generation process in many continuous wave (CW) THz systems is based on similar principles to CW technology operating at other frequencies, such as CW microwave radar and infrared spectroscopy. Instruments that were originally developed to emit either microwave or infrared radiation have been extended to generate THz radiation. For example, solid-state devices commonly used in the microwave frequency range (e.g. Gunn diodes) can today operate in the low THz frequency range. High-frequency oscillators, such as magnetrons, that are typically found in microwave radar can now also operate in the THz frequency range.

Unlike commercial pulsed THz-time domain spectroscopy (TDS) systems (to be discussed in Section 3.1.2), CW THz generators can be purchased separately from CW THz detectors. The choice of CW generator usually depends on the frequencies of interest, available space, cost, and output power. In this Chapter, five types of CW THz generators will be introduced:

1. Tunable gas lasers (Section 2.3)
2. Solid-state systems: tunable and non-tunable (Section 2.4)
3. Wave generation via difference frequency generation (Section 2.5)
4. Systems based on high-frequency oscillation (Section 2.6)
5. Systems based on electron acceleration, which can also operate in pulsed mode (Section 2.7)

Many types of CW generators are tunable over a wide range of frequencies. Tuning components, such as diffraction gratings, allow such CW systems to operate at one of several discrete frequencies. The gaps between available frequencies are usually wide

(several hundred GHz), but the range of tunable frequencies can reach 7 THz, as in the case of gas lasers. Wave generators and backward-wave oscillators (a type of high-frequency oscillator) are continuously tunable over a wide frequency range, i.e. there are no gaps between frequencies.

The non-continuous bandwidths of most CW THz systems (excluding wave generators and backward-wave oscillators) make them less favoured for broadband spectroscopic studies of the resonant modes in materials. However they are still useful in imaging applications where visual contrast between material types is desired. Many materials of interest (e.g. packaging foam, hidden weapons, illicit drugs) respond differently to THz radiation even when only one THz frequency is present. Non-destructive imaging is therefore one niche application for CW THz systems. An example of a three-dimensional CW imaging system is shown in Fig. 2.1.

Figure 2.1: A commercial THz imaging system. The PB7100 Frequency Domain THz Spectrometer from Loeffler Technology is reported to have a tunable bandwidth from 0.1 THz to 2 THz, and frequency resolution of less than 0.25 GHz. The system has 5-axes translation stages that allow for various scanning positions. After Loeffler Technology GmbH (2008).

2.2.1 Continuous Wave THz Detection

The detection processes utilised by CW THz systems are often similar to those used in non-THz CW applications, such as temporal measurements to calculate the Doppler shift, and pyroelectric measurements to convert a detected signal's heat to a voltage measurement. As a result of this wide variety of possible detectors, CW THz systems tend to be more varied in their design than pulsed THz-TDS systems (Chapter 3).

Many CW THz detectors are based on heat detection: Golay cells, bolometers, pyroelectric cameras (Fig. 2.2), and Schottky diodes. Ancillary devices, such as chopper[8] modulators, can be used to improve the signal to noise ratio of the detector. Software accompanying detectors, such as that shown in Fig. 2.3, simplifies data processing and

[8] Choppers will be formally introduced in Section 3.7.2.

allow immediate analysis of the detected THz signal, the beam shape, and diffraction pattern.

Figure 2.2: A THz pyroelectric camera. This pyroelectric camera captures CW THz radiation on its 124×124 pixel array of pyroelectric detectors. The 100×100 μm array is made from a type of ferroelectric material, and is housed behind the polyethylene window that limits the spectrum of unwanted incident light. A built-in chopper further improves the signal integrity. Equipment courtesy of X.-C. Zhang at RPI.

2.3 Tunable Gas Laser

Gas lasers came into existence very shortly after the first laser—a ruby laser—was unveiled in 1960. Ali Javan, William Bennett Jr., and Donald Herriott from Bell Labs invented the helium-neon (HeNe) gas laser (Javan *et al.* 1961) based on Ali Javan's idea of "collisions of the second kind" (Javan 1959). As its name implies, a HeNe laser uses a mixture of helium and neon gases as the gain medium in the optical cavity. By changing the gain medium, the operating frequency of the gas laser can be altered. This simple concept has led to the development of three classes of gas lasers with operating frequencies spanning from the THz to the ultraviolet range. The three classes of gas lasers are: neutral gas[9] (Willett 1971), ionised gas or ion gas[10] (Bridges and Chester 1971), and molecular gas (Pollack 1971). In the field of THz, molecular gas lasers are used to generate CW THz radiation; neutral gas lasers—the HeNe laser in particular—is often used for alignment purposes, such as aligning mirrors and lenses.

As with other lasers, molecular gas lasers that emit THz radiation need to be pumped in order to achieve population inversion. The pumping source is usually an optical one, such as an optical CO_2 laser[11], hence CW THz gas lasers are also known as optically pumped THz lasers or OPTLs (Mueller 2003). A CW THz gas laser's tunability is achieved in two ways: using an appropriate type of gas as the gain medium, and

[9] The HeNe laser is a neutral gas laser.
[10] Examples are argon and krypton lasers.
[11] The invention of the CO_2 laser is credited to C. K. N. Patel (Patel 1964).

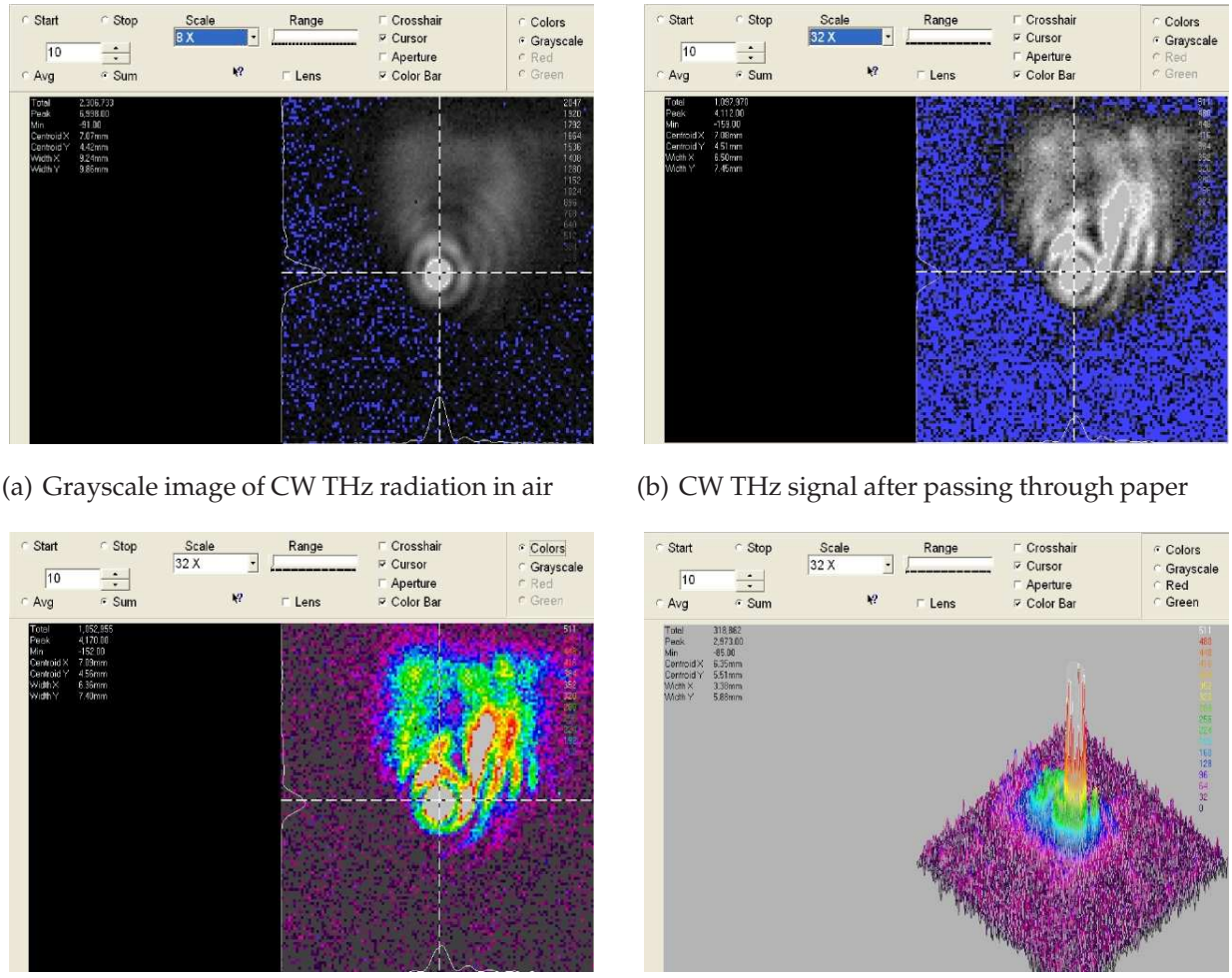

(a) Grayscale image of CW THz radiation in air

(b) CW THz signal after passing through paper

(c) Pseudocolour version of Fig. 2.3(b)

(d) Three dimensional view of Fig. 2.3(b)

Figure 2.3: Continuous wave THz images. Software used with the pyroelectric camera shown in Fig. 2.2 allows the user to visualise the THz signal in a variety of rendering options—grayscale, pseudocolour, and three dimensional. Although pyroelectric cameras are less sensitive than Golay cells and bolometers, due to the small sensing area of the camera array, they are useful for beam alignment and characterisation. (a) The intensity level of this grayscale image is scaled up by 8 times so that the bright region in the middle is distinct from the background noise—shown in blue in the electronic version of this Thesis. (b) The decrease in the signal strength is evident by the additional scaling (32 times) required. The diffraction pattern caused by the paper is clearly visible. (c–d) Pseudocolour and three dimensional rendering allows the user to access more information about the detected THz beam. Equipment courtesy of X.-C. Zhang at RPI.

varying the optical pump frequency through the use of diffraction gratings inside the optical pump laser.

The gain medium of an OPTL is a molecular gas that has a rotational energy gap, analogous to the band gap of electrons, which matches the photon energy of the optical pump. When photons from the optical pump excite the molecules of the gain medium, the molecules physically rotate from their ground rotational state to the first excited rotational state. When population inversion is achieved, the molecules begin to rotate back to their ground state; this transitional rotation causes the emission of CW THz photons from the molecules. In summary, OPTLs rely on molecular rotational transitions of low pressure gas for THz emission (Mueller 2008).

Figure 2.4 shows an example of an OPTL from Coherent Inc. This system includes a CO_2 pump laser and uses three types of molecular gases for generating CW THz radiation over a wide bandwidth (1.04 to 6.86 THz). The peak output power of this system is over 100 mW, allowing the propagation of CW THz over longer distances than most other THz systems. This is seen in Fig. 2.4 where the THz beam travels up from the benchtop level to an elevated x-y stage where the sample and detector are mounted. Despite their advantages, the large size and high cost of OPTLs have limited their popularity. Smaller and cheaper solid-state systems have overtaken OPTLs as the instruments of choice in the realm of CW THz imaging. Solid-state systems will be introduced in the next Section.

2.4 Solid-State Semiconductor Systems

The range of solid-state THz systems available today makes this group the largest in the family of CW THz generators. Solid-state THz systems can be described as THz systems that contain THz emitters and/or detectors made entirely out of semiconductor materials. This characteristic may initially appear similar to that of pulsed photoconductive antenna-based systems (to be introduced in Section 3.8), but the difference between them is that solid-state THz systems emit monochromatic THz radiation whereas pulsed photoconductive antenna-based systems are broadband. Tunable solid-state THz systems do exist and will be introduced later in this Section.

The appearance of solid-state THz systems can be divided into two groups: those that resemble microwave components, and those that resemble semiconductor chips. The former group is indeed an extension of the technology used in radio frequency (RF) applications, where the upper limit of the microwave frequency range has been pushed

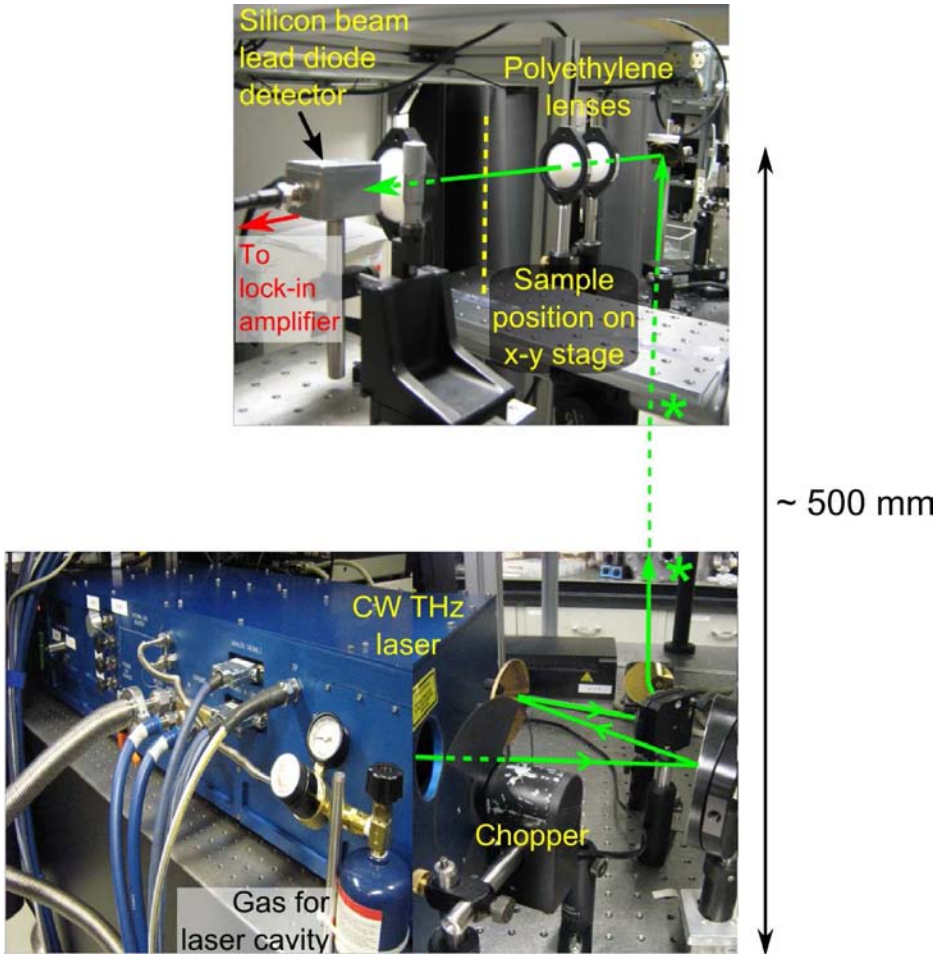

Figure 2.4: Continuous wave THz system based on a gas laser. This gas laser produces CW THz radiation from 1.04 to 6.86 THz, at discrete frequency intervals of around 0.24 THz. The laser contains an internal CO_2 laser that pumps a low pressure gas cavity. In order to attain a desired frequency, the correct type of gas needs to be released into the laser's cavity. Additionally, the correct pressure, relative to the gas type, needs to be maintained in the cavity. The CO_2 laser is then tuned to the correct pump frequency using external micrometer dials connected to a diffraction grating. Gases used in this laser are (in ascending order of frequency): difluoromethane (CH_2F_2), methanol (CH_3OH), and CD_3OH. Equipment courtesy of X.-C. Zhang at RPI.

up into the millimeter wave and THz frequency ranges. For example, the Gunn diode[12] is a common source of low frequency monochromatic microwave radiation. It can be found today, among other places, in motion sensors above automatic sliding doors. As shown in Fig. 2.5(a), a THz version of the Gunn diode exists in the low frequency range, where a Schottky diode is used as a detector. In keeping with typical RF fashion,

[12]The Gunn diode was invented in 1963 by yet another IBM employee, John Battiscombe Gunn.

both the emitter and detectors in this system are encased in metal chassis, with horn antennas used for emitting/detecting THz radiation.

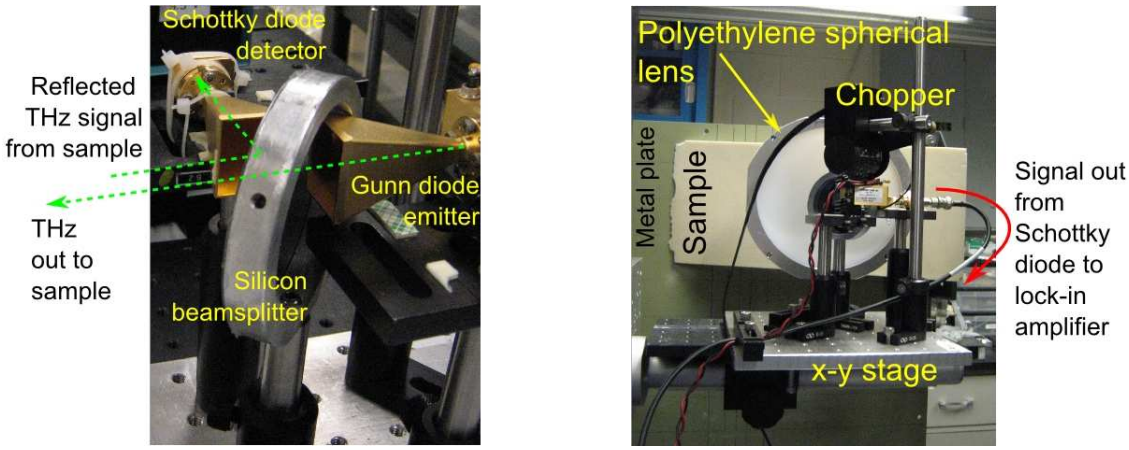

(a) Side view of a solid-state Gunn diode CW system (b) Back view of the same system

Figure 2.5: Continuous wave THz system based on a Gunn diode. (a) This CW system consists of a Gunn diode which emits THz radiation at 0.1 THz. The radiation is directed at a sample, which reflects the THz back to a Schottky diode detector. The silicon beamsplitter is transparent to the outgoing THz radiation, but acts as a mirror to the returning radiation. (b) Back view of the same system being used to examine hidden defects inside a piece of foam used in NASA space shuttles. A chopper is used to modulate the signal in order to decrease the influence of noise. The polyethylene lens focuses the THz signal onto a metal sheet behind the foam. This metal sheet reflects the THz signal back to the Schottky diode. The entire system is mounted on a x-y stage so that the entire piece of foam can be raster scanned. Equipment courtesy of X.-C. Zhang at RPI.

Unlike conventional RF oscillators, RF-derived THz emitters and detectors are not usually frequency or intensity tunable, but they have high peak output powers. They are therefore usually used in imaging applications as shown in Fig. 2.5(b). In addition, the high cost of these systems[13] has limited their widespread use.

A more popular alternative to RF-based THz devices is a semiconductor chip-like solid-state THz emitter that is used in conjunction with a suitable THz detector, such as those introduced in Section 2.2.1. Systems that contain both solid-state semiconductor emitters and detectors are currently being developed (Plusquellic *et al.* 2003, Crowe *et al.* 2004), as well as new solid-state semiconductor detectors based on pulsed

[13]Examples of manufacturers are Virginia Diodes, Wasa Millimeter Wave, and Spacek Labs. An emitter typically costs over US$20,000.

THz systems: electro-optic (EO) detection (Nahata *et al.* 2002), full EO (Siebert *et al.* 2002b, Siebert *et al.* 2002a), and log-periodic photoconductive emitters (Mendis *et al.* 2004). The following Subsection will briefly introduce solid-state THz emitters.

2.4.1 Solid-State Semiconductor THz Emitters

One major type of solid-state THz emitter is the injection laser, which is a type of diode laser. It is a distant relative of the early rudimentary semiconductor diode laser (Hall *et al.* 1962, Nathan *et al.* 1962, Holonyak Jr. and Bevacqua 1962, Quist *et al.* 1962). The diode laser was distinct from other lasers at the time in that it was electrically pumped instead of optically pumped. This distinction was made more pronounced by the progeny of the diode laser, the double-heterostructure injection laser (Kressel and Nelson 1969, Hayashi *et al.* 1970), which is pumped by an injected electrical current.

The benefit of the double-heterostructure injection laser is that it is more energy efficient than the early diode laser. This means it can emit CW radiation without damage. Terahertz lasers based on the double-heterostructure have been developed: tunable hot-hole semiconductor laser (Bründermann *et al.* 1999, Gousev *et al.* 1999, Bründermann *et al.* 2000, Bergner *et al.* 2005), and the THz-heterostructure laser (Köhler *et al.* 2002). The double-heterostructure injection laser has also spurred the development of quantum well lasers (Dingle *et al.* 1974), which is the foundation of the THz quantum cascade laser as shown in Fig. 2.6(a) (Faist *et al.* 1994, Faist *et al.* 2004), and quantum cascade photonic crystal lasers as shown in Fig. 2.6(b) (Colombelli *et al.* 2008).

The operation of a quantum cascade laser (QCL) is eloquently described by Bell Labs: "Consider it an electronic waterfall: When an electric current flows through a quantum-cascade laser, electrons cascade down an energy staircase emitting a photon at each step," (Bell Laboratories Physical Sciences Research 2000). As shown in Figs. 2.6(a) and 2.6(b), all QCL-based devices are physically extremely small but they operate at very low temperatures: below 117 K (-156°C) in CW mode (Worrall *et al.* 2006). As a result, a QCL needs to be encased in a refrigeration apparatus, such as a cryostat, making the overall setup fairly large as shown in Fig. 2.7. However an initiative exists to integrate QCLs into smaller refrigerated modules, as shown in Fig. 2.6(c), for operation at room temperature (Bründermann *et al.* 2006).

NOTE:
These figures are included on page 37 of the print copy of the thesis held in the University of Adelaide Library.

(a) Mid-IR QCL with 32 lasers

(b) Surface emission from a photonic crystal QCL

(c) The turnkey Quanta-Tera tunable THz QCL

Figure 2.6: Quantum cascade laser (QCL). (a) Although this QCL operates in the mid-IR range, it is a good example of the small scale of most QCLs, including THz QCLs. The top picture shows 32 individually tunable lasers on a single chip that is less than 4×5 mm in size. The bottom SEM image shows the individual laser ridges. Radiation is emitted at the end of each ridge. After Lee *et al.* (2008). (b) Photonic crystals (PC) are an alternative to the ridged QCL structure, but most PC QCLs only emit one dominant frequency per structure, thus are in theory not tunable. The top image is a schematic of a photonic crystal QCL showing surface emission of radiation from the array of holes. The bottom SEM image of the plan view of a photonic crystal QCL clearly shows the hole array. After Colombelli *et al.* (2008). (c) The small size of QCLs make it possible to integrate them into small, turnkey systems, such as this Quanta-Tera system which contains not one but two QCLs installed inside the liquid nitrogen-cooled dewar. The external pulse driver allows the QCLs to emit pulsed THz radiation between 3.5 to 4 THz at 0.2 mW peak power at 77 K through the dewar's quartz window. This window, which has a diameter of 25 mm, has a THz output aperture of 20 mm. After Bründermann *et al.* (2006).

The THz quantum cascade laser (QCL) is a popular THz source for CW imaging applications (Darmo *et al.* 2004, Nguyen *et al.* 2006, Kim *et al.* 2006). A typical setup for imaging is as shown in Fig. 2.8(a). Examples of images derived from a QCL system are shown in Figs. 2.8(b) and 2.8(c).

Most existing QCLs operate in CW mode and are not tunable, however pulsed THz QCLs are being investigated (Williams *et al.* 2005), and a tunable QCL operating in the

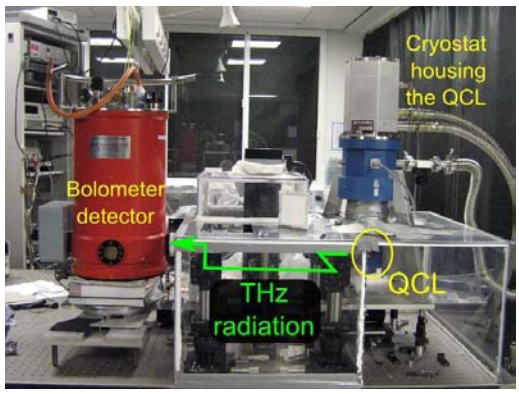

Figure 2.7: Continuous wave THz spectroscopic system based on a QCL. Although the QCL is physically small, the cryostat that houses it results in an overall QCL THz system that is considerably larger. A bolometer is used as a detector in this example. Equipment courtesy of R. E. Miles at the University of Leeds.

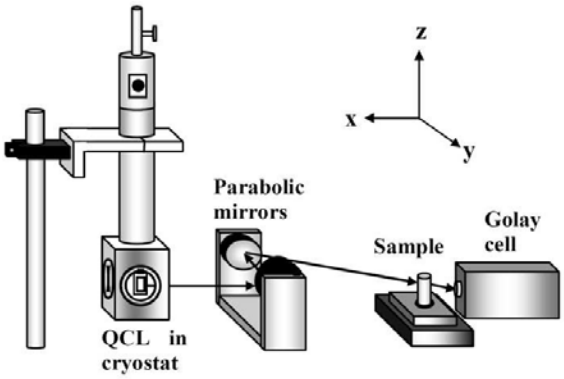

NOTE:
These figures are included on page 38 of the print copy of the thesis held in the University of Adelaide Library.

(a) QCL-based CW imaging system (b) Image capture using a Golay cell (c) Image capture using a bolometer

Figure 2.8: Continuous wave THz imaging system based on a QCL. (a) Typical CW imaging setup with a QCL as the THz source. (b) (Top) Optical image of polystyrene foam with a triangular cross-sectional shape and an internal cavity; (Bottom) Using a QCL as the CW THz source, the image is captured with a Golay cell. After Nguyen *et al.* (2006). (c) (Top) Optical image of a slice of rat brain; (Bottom) With a QCL as the CW THz source, the 1394-pixel image of the brain slice is captured with a bolometer. After Kim *et al.* (2006).

mid-infrared frequency range has been reported (Lee *et al.* 2008). The pace of QCL research has gained tremendous momentum in recent years, thus QCLs may one day be as ubiquitous as pulsed THz-TDS systems.

2.5 THz Sources Based on DFG

Difference frequency generation (DFG) is a technique that was initially utilised to study nonlinearity in materials, specifically the second order susceptibility $\chi^{(2)}$ from second

harmonic generation (Dick *et al.* 1985). Difference frequency generation, together with sum frequency generation (SFG), were subsequently used to study new materials for THz generation (Zhang *et al.* 1994). As their names imply, DFG and SFG involve the use of two pump lasers, operating at frequencies ν_1 and ν_2 respectively, to generate a third frequency that is either the sum or difference of ν_1 and ν_2. Details of DFG and SFG can be found in Boyd (2003).

Difference frequency generation-based THz sources utilise the process of DFG inside a semiconductor crystal for generating CW THz radiation that is tunable continuously (i.e. no gaps between frequencies) from 0.3 THz to above 7 THz. In these THz sources, DFG occurs inside an undoped semi-insulating gallium phosphide[14] (GaP) crystal so that the outgoing radiation has a frequency equal to the difference of ν_1 and ν_2. By choosing suitable values of ν_1 and ν_2, the outgoing radiation will be in the THz frequency range. A yttrium aluminium garnet (YAG) laser[15] provides a frequency of ν_1 = 281.9 THz, and a beta barium borate- (β-BaB_2O_4 or BBO) based optical parametric oscillator[16] (OPO) provides a frequency of ν_2 between 282.2 and 285.7 THz. The YAG laser and OPO signals are incident non-collinearly on the GaP crystal, i.e. a small angle exists between the two signals. By tuning ν_2, continuous THz frequencies between 0.3 and 3.8 THz can be measured using a bolometer (Tanabe *et al.* 2003b).

Improvements to the THz DFG process has allowed an extension of the upper frequency range to 7 THz (Tanabe *et al.* 2003a, Tanabe *et al.* 2003c), and an increment of the peak power level to 800 mW (Nishizawa *et al.* 2008). A simpler THz DFG process was also devised using two chromium forsterite (Cr:forsterite) lasers instead of the more cumbersome YAG laser/OPO setup (Nishizawa *et al.* 2006). The spectral resolution from THz DFG is comparable to that of pulsed THz systems, hence they have been used in spectroscopic studies of biomolecules such as proteins, DNA, RNA, and liquid crystals (Nishizawa *et al.* 2003, Nishizawa *et al.* 2005, Nishizawa *et al.* 2008). The THz DFG process is now being developed to suit rod-type THz waveguides that are a few hundred microns in thickness (Nishizawa *et al.* 2007). Given its high peak power, THz DFG appears to have a promising future, and could eventually be a viable alternative to pulsed THz systems.

[14] GaP is used in green and red light emitting diodes.
[15] The YAG laser is pumped by a laser diode.
[16] The OPO is pumped by a neodymium-doped YAG (Nd:YAG) laser.

2.6 THz Sources Based on High-Frequency Oscillation

This Section introduces terahertz sources based on the fundamental technology of high-frequency oscillation in vacuum chambers. This technology, which has been in use since the early half of the 20th century, involves the acceleration of electrons with a strong magnetic or electric field along a long cavity such that the electrons 'bunch up' and induce standing waves—a process akin to electronic resonant oscillation. Examples of high-frequency oscillators are cyclotrons[17], klystrons[18], magnetrons[19], travelling-wave tubes[20], and backward-wave oscillators (BWOs).

2.6.1 Gyrotron

Most high-frequency oscillators invented in the 20th century are capable of generating microwave frequencies at high output power (tens of kilowatts), hence they are used extensively in radars. The difference between them lies primarily in whether a linear or a circular accelerator path is employed. Linear accelerators (e.g. klystron) tend to be large in scale owing to the long cavity length needed for oscillation. Circular accelerators (e.g. cyclotron) are more compact in size because a spiral oscillation path is employed instead. The gyrotron, a type of circular accelerator, can typically produce frequencies in the low terahertz range (below 300 GHz) with output power of a few megawatts, although frequencies up to 889 GHz at lower output power of several hundred watts have been reported (Idehara *et al.* 2006). An example of a gyrotron is shown in Fig. 2.9(a).

[17] Invented in the late 1920s by Ernest Orlando Lawrence of the University of California at Berkeley (UCB) (Lawrence and Livingston 1932). The Lawrence Berkeley National Laboratory at UCB, and the Lawrence Livermore National Laboratory outside San Francisco are named after him (American Institute of Physics 2008).

[18] Invented in the late 1930s by brothers Russell and Sigurd Varian from Stanford University. The Varians founded Varian Associates, which today has business interests in semiconductors (Varian Semiconductors), medical instruments (Varian Medical Systems) such as computed tomography and radiography, and non-destructive testing.

[19] Invented in the 1920s by Albert Hull of the General Electric Research Laboratory in Schenectady, New York.

[20] Attributed to Rudolf Kompfner during World War II at the Allied forces' radar development laboratory in Britain.

NOTE:
These figures are included on page 41 of the print copy of the thesis held in the University of Adelaide Library.

(a) Example of a large-scale gyrotron

(b) Example of a modern gyrotron that is significantly smaller

Figure 2.9: Gyrotrons. (a) Gyrotrons are typically large, such as this 95 GHz, multi-megawatt continuous wave gyrotron being developed at Communications and Power Industries in Palo Alto, California. After Felch *et al.* (2008). (b) The push to develop compact terahertz sources has resulted in the miniaturisation of gyrotrons. The compact disk (CD) shown in this Subfigure gives the impression of scale. After Glyavin *et al.* (2008).

Gyrotrons utilise the principle of electron cyclotron maser instability in vacuum tubes (oscillator tubes) to achieve high power and high efficiency operation in the submillimeter and terahertz frequency ranges (Mitsudo *et al.* 2006). Gyrotrons operating below 100 GHz at low power (below 100 kW) have been in existence since the late 1970s. High power gyrotrons operating above 100 kW were introduced in 1982 by Temkin *et al.* The impetus behind gyrotron research at the time was primarily in developing high frequency microwave radiation for heating magnetically confined plasma in tokamaks[21] (Temkin *et al.* 1982). Since most tokamak facilities are large in scale, miniaturisation of large gyrotrons was not critical.

The push for compact and reliable terahertz sources in the late 20th century ignited interest in high frequency gyrotron development and miniaturisation. As shown in Fig. 2.9(b), some modern gyrotrons are significantly smaller in size than their predecessors. Today's submillimeter and terahertz frequency range gyrotrons can produce output powers of several megawatts in both tunable continuous wave as well as pulsed mode (Litvak 2008). In pulsed gyrotron systems, the coherent terahertz pulses have

[21] In thermonuclear fusion power, hydrogen plasma is heated and squeezed by a magnetic field that is confined inside a toroidal vacuum chamber. The (large) machine that does this is called a tokamak.

lengths of several tens of microseconds (Glyavin *et al.* 2008), which is longer than that from a conventional pulsed THz-TDS system described in Section 3.8.2 (typically several hundred picoseconds), therefore pulsed gyrotrons are sometimes referred to as *long-pulsed* gyrotrons.

Gyrotron Applications

When compared to conventional electro-optic pulsed THz systems, the output power of gyrotrons is extremely high. This makes gyrotrons an ideal high frequency industrial and plasma heating source. Applications that utilise gyrotrons usually require massive quantities of heat. For example, gyrotrons are used to heat plasma in nuclear fusion experiments, such as those being conducted at the Joint European Torus (JET), and in the future at *ITER*[22]. Pictures of JET and *ITER* are shown in Fig. 2.10. The *ITER* project has been a driving force in the development of high power gyrotrons (Westra 2008, Popov *et al.* 2008, Rzesnicki *et al.* 2008). Gyrotrons are also used industrially in annealing, and melting hard composites containing glass and/or ceramic (Gyrotron Tehcnology Inc. 2008).

2.6.2 Backward-wave oscillator (BWO)

Another type of high-frequency oscillator used as a terahertz source is the backward-wave oscillator (BWO). The BWO, which is also known as a backward wave tube[23] or carcinotron, is a type of travelling-wave tube. It therefore contains an anode and a cathode. By varying the voltage between these electrodes, a BWO can be tuned over a narrow frequency range to generate monochromatic submillimeter and terahertz radiation with tens of milliwatts in output power. The typical tunable frequency range is between 0.2 to 1.4 THz.

BWO Applications

BWOs operating in the terahertz range tend to be small enough to be used as a benchtop terahertz source. This is shown in the main picture in Fig. 2.11. The drive for

[22] *ITER* is a joint international tokamak project involving the European Union, Japan, China, India, South Korea, Russia, and the USA. *ITER*, which means 'journey' in Latin, used to be the acronym for the "International Thermonuclear Experimental Reactor", but the acronym is now defunct; the project is now simply called *ITER*, with no specific interpretation for its name.

[23] The backward-wave oscillator was invented independently by Epsztein (1952) and Kompfner (1952).

NOTE:
These figures are included on page 43 of the print copy of the thesis held in the University of Adelaide Library.

(a) Scale of *ITER* (right) compared to JET (left), and to man

(b) Heated plasma inside the JET vacuum chamber

Figure 2.10: JET and ITER tokamaks. The high output power of gyrotrons make them suitable for heating plasma in nuclear fusion experiments in tokamaks. (a) The Joint European Torus (JET) is, as of 2008, the world's largest tokamak. It can deliver up to 30 MW of power. Situated in Oxfordshire in the UK, JET is an initiative of the European Fusion Development Agreement (EFDA). JET will be dwarfed by *ITER* in size when *ITER* is completed in 2015. (b) Split image showing the interior of the JET vacuum vessel (left) with a superimposed image of an actual JET plasma (right), taken with an infrared camera in 2005. Caption text and photographs after EFDA-JET (the European Fusion Development Agreement 2008).

the miniaturisation of terahertz sources has also influenced BWO design, resulting in micro-BWOs such as that shown in the inset of Fig. 2.11. Like other CW terahertz systems, BWO-based systems tend to be used in conjunction with either a radiometer (e.g. Golay cell) or a thermal detector (e.g. bolometer, pyroelectric detector).

Figure 2.11: Backward-wave oscillator. (Main picture) An example of a terahertz BWO used at Georgia Institute of Technology, USA. After Anbarasu (2008); (Inset) A micro-BWO manufactured by Teraphysics Inc. It is quoted as being able to generate >40 mW output power. After Teraphysics Inc. (2008).

NOTE:
This figure is included on page 43 of the print copy of the thesis held in the University of Adelaide Library.

2.7 THz Sources Based on Electron Acceleration

In Section 2.6, linear and circular accelerators introduced were for the purpose of generating radiation and heat through high-frequency oscillation of electrons. This Section also deals with accelerators but purely for accelerating electrons to almost the speed of light in order to capture intensely bright light at a wide range of electromagnetic frequencies, including terahertz light. These accelerators however still require the use of the high-frequency oscillators introduced in Section 2.6 as high energy electron sources.

The THz light produced in by electron acceleration can be both CW and pulsed. Pulsed THz radiation generated by electron acceleration can be utilised in the same way as pulsed THz emitted by electro-optic (EO) rectification or a photoconductive antenna (PCA) to be introduced in the next Chapter.

2.7.1 Synchrotrons

Like a tokamak (Section 2.6.1), a synchrotron[24] also utilises a circular acceleration path, but the cross-section of a synchrotron path is shaped less like a torus and more like a rectangular waveguide. As illustrated in Figs. 2.12(a) and 2.12(b), the scale of most synchrotrons around the world is comparable to that of tokamaks.

Electrons are accelerated in the circular acceleration path to almost the speed of light. As the path of the accelerating electrons bends, light is emitted tangentially and channelled into a pipe-like device called a *beamline*, exiting from outlets as shown in Fig. 2.13(a). Depending on the acceleration of the electrons prior to a bend, light at a specific frequency can be captured in a beamline, hence many beamlines are distributed along the periphery of the circular path in order to capture the various frequencies. This allows scientists to utilise specific frequencies by simply choosing the beamline of interest. As shown in Figs. 2.13(b)–2.13(d), frequencies available at a synchrotron range from X-ray (Fig. 2.13(a)) to the THz range (FIR), where THz frequencies from 1.5–13.5 THz have been reported (Falconer *et al.* 2009).

Given the large range of frequencies available at a synchrotron, it is not unusual for a host of multidisciplinary activities to be conducted simultaneously at a synchrotron.

[24] Sometimes known as a *Light Source* (e.g. the Canadian Light Source, and the Advanced Light Source at the Lawrence Berkeley National Laboratory in Berkeley, California), or a *Photon Source* (e.g. the Advanced Photon Source at the Argonne National Laboratory outside Chicago).

NOTE:
These figures are included on page 45 of the print copy of the thesis held in the University of Adelaide Library.

(a) Plan view of the Advanced Photon Source in Illinois, USA

(b) Aerial and interior views of the Australian Synchrotron

Figure 2.12: Examples of synchrotrons. (a) This plan shows the large number of beamlines that can exist simultaneously at a single synchrotron facility; various research sectors are colour coded according to discipline. After Argonne National Laboratory (2008). (b) The Australian Synchrotron, which began operation in 2007, has a mid-infrared beamline with a nominal beam size (at a sample) of 8×8 μm, and a high frequency terahertz beamline (>10 THz) for high-resolution Fourier Transform Infrared (FTIR) studies. The bottom picture, taken at the synchrotron's Community Open Day in 2005, clearly shows the outline of the circular acceleration path. After the Australian Synchrotron (2008).

Figure 2.12(a) illustrates the number of beamlines and variety of research at the Advanced Photon Source at the Argonne National Laboratory outside Chicago, USA. An excellent resource on synchrotrons is at `www.lightsources.org`.

Synchrotron-Based Biological Applications

The broad range of frequencies available from a synchrotron is particularly beneficial for biological applications because of the numerous biologically relevant frequencies from the infrared through to the terahertz range. Furthermore, a synchrotron is capable of generating these frequencies at intense brightness (irradiance or photon flux), thus

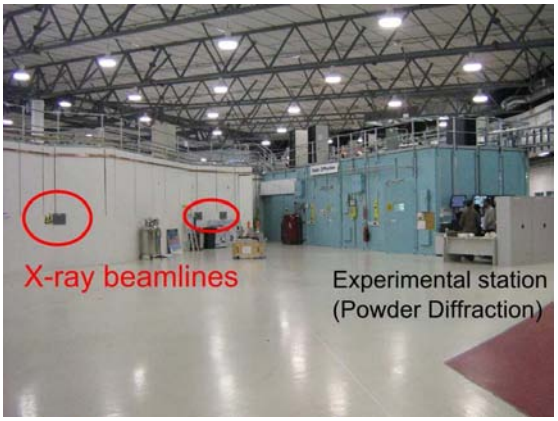

(a) An example of an experimental station with three adjacent untapped X-ray beamlines

(b) Upon exiting the beamline, the FIR beam is split into two paths

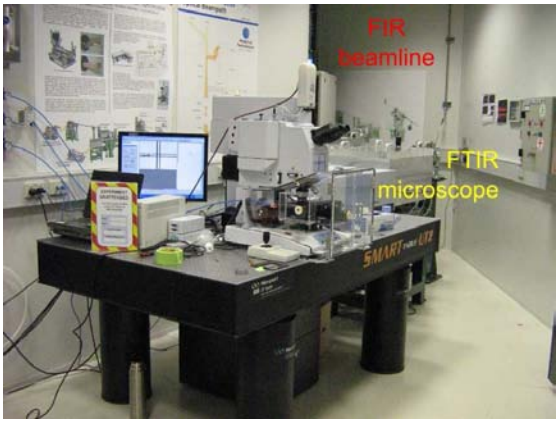

(c) One FIR path is used for FTIR microscopy

(d) The other FIR path is used for high-resolution FTIR spectroscopy

Figure 2.13: The Australian Synchrotron. (a) X-ray powder diffraction is conducted in the experimental station shown. Three untapped beamlines with frequencies in the X-ray range are clearly visible, with ample floor space for more experimental stations. (b) Upon exiting the beamline, the FIR beam is split into two paths. (c) One path is directed into a FTIR microscope. (d) The other path is directed into a high-resolution FTIR spectrometer. Equipment courtesy of the Australian Synchrotron in Clayton, Victoria.

improving the signal-to-noise ratio. This means that in the realm of microscopy and imaging, frequency and spatial resolutions have been improved to an unprecedented level of a few microns, therefore creating new possibilities in studying cells and biotissue (Miller *et al.* 2003). Figure 2.14 shows an example of the fine spatial resolution attainable from synchrotron microspectroscopy.

NOTE:
These figures are included on page 47 of the print copy of the thesis held in the University of Adelaide Library.

(a) 3D reconstruction of the blood vessels in a mouse brain

(b) Microtomography of the mouse brain

Figure 2.14: High resolution images from a synchrotron. (a) The high spatial resolution attainable from synchrotron light is demonstrated in this 3D reconstruction of the blood vessels in the brain of a transgenic mouse. After the Swiss Light Source (2008). (b) Microtomography of the mouse's brain allows the viewer to zoom into a specific location in the brain, revealing fine details of the smallest vascular features that are 1.4 μm in size. After the Paul Scherrer Institut (2008).

It is interesting to note that the intense brightness of synchrotron beamlines is not related to high power generation. This is as opposed to the intense brightness in a tokamak (Section 2.6.1) where high power generation is the goal. A synchrotron generates light that is spatially shaped like a cone (analogous to the sweeping action of a search light); the cone narrows as the electron acceleration increases, eventually producing an intensely tight (and therefore bright) cone of light (Carr 1999).

2.7.2 Free Electron Laser

A free electron laser (FEL) is similar to a synchrotron in that it can also generate radiation with intense brightness, but a FEL uses a linear electron acceleration path and is smaller in scale. However, as shown in Fig. 2.15(a), most free electron lasers are still extremely large when compared to benchtop terahertz sources.

Referring to Fig. 2.15(b), a FEL consists of a high energy electron source, such as a klystron (Section 2.6), which emits a beam of electrons into a linear accelerator where the electrons' velocity is increased. At the end of the linear accelerator, the electrons

NOTE:
These figures are included on page 48 of the print copy of the thesis held in the University of Adelaide Library.

(a) FEL at the Jefferson Lab in Virginia, USA

(b) Components of a FEL

Figure 2.15: Examples of free electron lasers. (a) Although smaller than synchrotrons, most free electron lasers are still large when compared to benchtop terahertz systems. After Jefferson Lab (2008). (b) A FEL is similar to a conventional laser in that it too has a laser cavity, but it lacks a lasing medium which means it is capable of generating high power radiation with fewer problems due to cavity heating. After Williams (2007a).

pass into a laser cavity containing an insertion device, such as a wiggler or a magnetic undulator. The insertion device periodically deflects the beam of electrons in the cavity, which over time causes all the electrons to bunch up and oscillate in unison. This oscillation produces coherent radiation, which intensifies in power if the electrons form tighter bunches in the cavity. Once the coherent radiation is detected, the electrons are fed back to the start of the linear accelerator and the process repeated, resulting in a highly efficient system. A FEL can either operate in CW or pulsed mode. In the CW mode, it can be tuned precisely over a wide range of frequencies, including the terahertz range. At the Jefferson Lab in Virginia, USA, beamlines between 0.1–10 THz are available with a total output power of 150 W (Williams 2007b).

The electron source and linear accelerator in a FEL are responsible for the FEL's large size. A more compact terahertz FEL has been developed by ENEA-Frascati[25] through the use of a microtron[26], but the apparatus as shown in Fig. 2.16(a) is still large.

The high terahertz output power from a FEL makes it particularly useful in applications requiring high power, such as in the study of liquids. Additionally, liquid samples can be measured *in situ* in commercial liquid holders such as cuvettes and culture dishes. This is shown in Fig. 2.16(b) where terahertz channelled from the FEL through

[25] The Italian National Agency for New Technologies, Energy and the Environment (ENEA) has a research centre in the town of Frascati, just outside Rome. This centre is referred to as ENEA-Frascati. Frascati is also home to the Frascati Tokamak Upgrade (FTU).

[26] A microtron is a type of cyclotron.

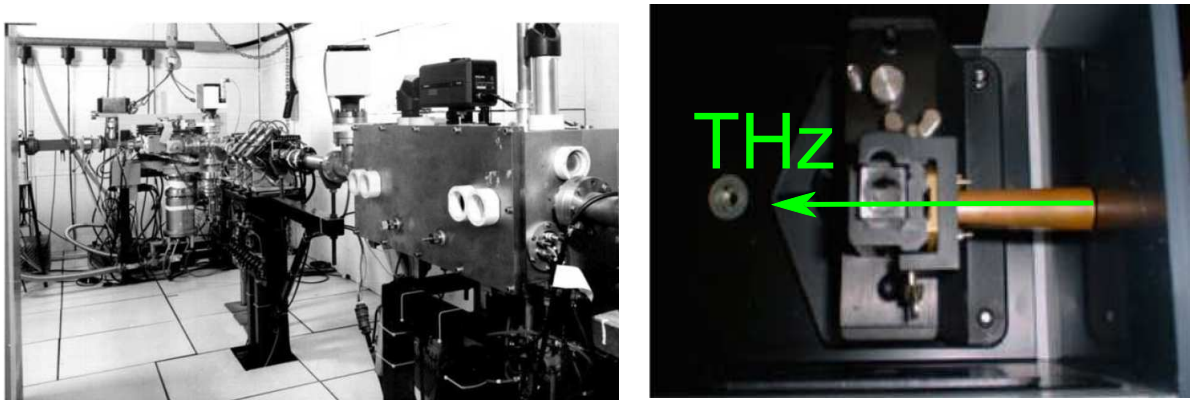

(a) Compact THz FEL at ENEA-Frascati, Italy

(b) CW terahertz from the compact FEL is channelled inside copper tubes to the sample

Figure 2.16: Continuous wave THz system based on a FEL. (a) The compact FEL at ENEA-Frascati generates CW terahertz between 70-200 GHz, with a centre/peak frequency at 120 GHz. (b) By channelling the high power CW terahertz from the FEL through copper tubes, samples can be analysed in the same way as in a desktop terahertz system, with the added advantage of high terahertz power. Free electron lasers are therefore frequently used in the study of liquids. After Doria *et al.* (2004).

copper pipes is transmitted through a cuvette. Examples of samples that have been successfully measured with a FEL are: cells and bio-tissue (Grosse 2002), blood and serum (Giovenale *et al.* 2003, Scarfí *et al.* 2003), liposomes (Doria *et al.* 2004), water and buffers (Xu *et al.* 2006a), and protein in liquid water (Xu *et al.* 2006b, Xu *et al.* 2006c).

2.8 Chapter Summary

An overview of THz systems that are not based on electro-optic (EO) or photoconductive (PC) THz generation has been presented in this Chapter. These systems vary considerably in terms of their sizes, types of hardware used, the THz generation and detection techniques utilised, and their real-world applications. Although smaller systems, such as quantum cascade lasers (QCLs) and backward-wave oscillators (BWOs), are gaining popularity in THz research laboratories, their lack of frequency tunability (QCLs) and narrow bandwidth (BWOs) have limited their use. A survey of THz literature past and present reveals that the bulk of THz research involves broadband THz frequencies, hence pulsed THz systems are most widely used.

As discussed in this Chapter, pulsed THz systems that do not rely on EO/PC THz generation tend to be large in size (e.g. synchrotron, free electron laser); space and

cost considerations are obvious limitations to their widespread use in a typical THz research laboratory. Pulsed THz systems that do rely on EO/PC THz generation offer a good compromise between technical fidelity, cost effectiveness, and economical use of laboratory space. The broad bandwidth and high signal-to-noise ratio of these pulsed EO/PC THz systems make them ideal for spectroscopic studies. Furthermore, their low average power allow for non-destructive inspection of fragile biological materials, such as biotissue. These favourable properties of pulsed EO/PC THz systems are the reasons why they are utilised for all THz measurements presented in this Thesis.

The next Chapter presents an in-depth discussion of pulsed EO/PC THz systems. Since *time domain spectroscopy* (TDS) is usually performed by these systems, they shall henceforth be referred to as *pulsed THz-TDS systems*.

Chapter 3

An Overview of Terahertz Systems: Part 2

THE generation and detection of pulsed terahertz (THz) from a time domain spectroscopy (TDS) system depends on one of two underlying mechanisms: optical rectification of crystals with second order nonlinearity, or transient photoconductivity. This Chapter will first introduce the different types of pulsed THz-TDS systems available today that rely on optical rectification or transient photoconductivity. It will then provide the necessary theory required to understand optical rectification and transient photoconductivity. The individual optical components in these systems are then described.

Acronyms and symbols related to THz systems

AC	alternating current
CW	continuous wave
DAST	dimethyl amino 4-N-methylstilbazolium tosylate
DC	direct current
EO	electro-optic
FIR	far-infrared
FWHM	full width at half maximum
GaAs	gallium arsenide
GVM	group velocity mismatch
HWP	half wave-plate
In	indium
InAs	indium arsenide
InP	indium phosphide
ITO	indium tin oxide or tin-doped indium oxide
LIA	lock-in amplifier
$LiNbO_3$	lithium niobate
$LiTaO_3$	lithium tantalate
Nb	niobium
NL	nonlinear
NLTL	nonlinear transmission lines
OR	optical rectification
PCA	photoconductive antenna
QWP	quarter wave-plate
RPI	Rensselaer Polytechnic Institute
SOS	silicon-on-sapphire
TDS	time domain spectroscopy
TEM	transverse electric and magnetic
WP	Wollaston prism
YBCO	$YBa_2Cu_3O_{7-\delta}$
ZnTe	zinc telluride

e	*extraordinary*-axis
o	*ordinary*-axis

p	parallel polarisation
s	perpendicular polarisation
c	speed of light *in vacuo*
t	continuous time
ν	frequency
ω	angular frequency = $2\pi\nu$
μ	magnetic permeability
$\sigma(t)$	conductivity
r	radial distance
Δx_1	depth
l_1	depletion depth
$\delta(t)$	unit impulse function
I	current
V	voltage
$v(t)$	velocity
$i(t)$	transient current
$\chi^{(1)}$	linear electric susceptibility
$\chi^{(2)}$	second-order nonlinear electric susceptibility
$\chi^{(3)}$	third-order nonlinear electric susceptibility
∇^2	Laplacian
n	refractive index
$\boldsymbol{\eta}_{ij}$	relative impermeability tensors
r_{ijk}	Pockels coefficient or linear electro-optic coefficient
E	scalar electric field
$\mathbf{E}$	electric field vector
$\tilde{\mathbf{E}}(t)$	rapidly time-varying electric field vector
$\tilde{E}(t)$	rapidly time-varying electric field
$\mathbf{P}$	electric polarisation vector
$\tilde{\mathbf{P}}$	rapidly time-varying electric polarisation vector
$\tilde{P}$	rapidly time-varying electric polarisation
$\mathbf{p}(t)$	dipole moment
$\mathbf{J}$	electric current density

3.1 Overview of Pulsed THz-TDS Systems

Pulsed THz-time domain spectroscopy (TDS) systems are possibly the most common systems in THz research laboratories around the world. The underlying setup of most pulsed THz systems is the same, based on the groundbreaking work in the 1980s and 1990s of THz pioneers such as David H. Auston, Christof Fattinger, Daniel Grischkowsky, Bin Bin Hu, Gerard Mourou, Peter Smith, Janis Valdmanis, and Xi-Cheng Zhang.

Pulsed THz systems are so named because the THz radiation emitted from these systems is pulsed. Additionally, the range of frequencies contained in each THz pulse is often in practice between 0.1 and 4 THz (typically 0.1–2 THz when a sample is in place), hence pulsed systems are broadband. This differs from the continuous wave (CW) radiation emitted from CW systems described in Chapter 2. The range of frequencies from a pulsed system is equal to the classical vibrational frequency range of polar molecules. This makes pulsed THz ideal for studying molecular dynamics, such as rotational and vibrational modes of molecules. Pulsed THz systems are therefore suitable for spectroscopic studies. The interaction of THz radiation with molecules is further described in Chapter 4.

There are two common configurations (modes) in which pulsed THz systems can operate: transmission and reflection. Most systems are built to operate in one mode only, however both modes can exist in a single system where flip-mirrors are used to switch between modes. Although both modes have their merits, transmission mode systems tend to be more popular, in part because they are easier to align.

In the following Subsection, an overview of custom-built pulsed THz systems is provided. This is followed by a quick review of commercial pulsed THz systems which are attracting increasing interest from both THz novices and experts. From Section 3.2 onwards, the fundamental physics behind THz generation and detection is explained in detail.

3.1.1 Custom-Built Systems

Fig. 3.1 shows two types of common custom-built pulsed THz systems. Both systems are fundamentally very similar except for the types of THz emitter/detector used. Photoconductive antenna (PCA) emitters/detectors are described in Section 3.8, while

electro-optic (EO) emitters/detectors are described in Sections 3.9 and 3.10. It should be noted here that pulsed THz systems need not be purely EO or photoconductive. A mixture of EO and photoconductive is commonplace (e.g. EO emitter and photoconductive antenna detector, or *vice versa*).

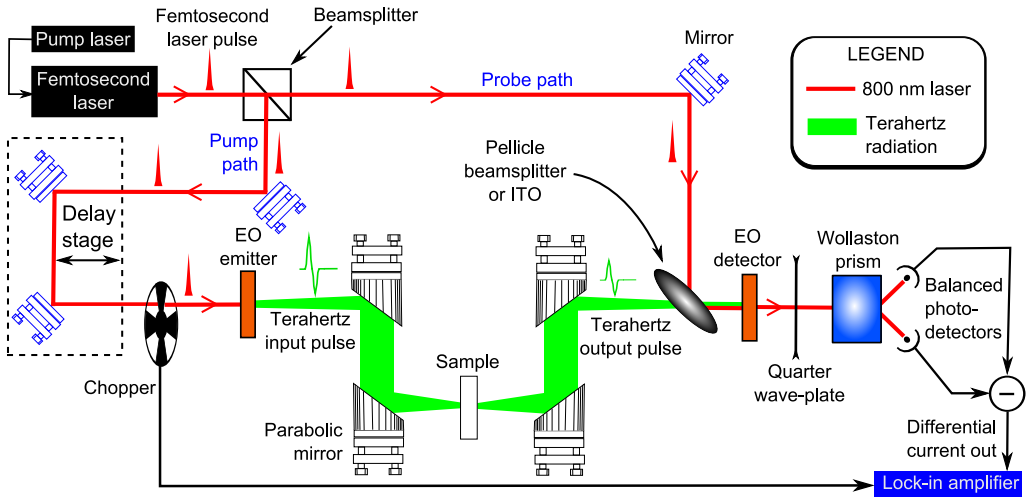

(a) EO pulsed THz system in transmission mode

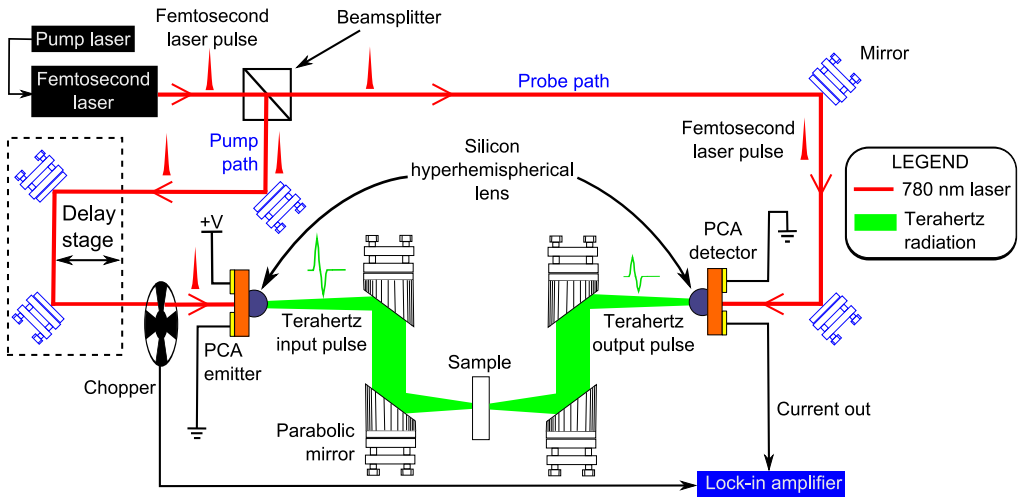

(b) PCA pulsed THz system in transmission mode

Figure 3.1: Types of pulsed THz systems. (a) Pure electro-optic (EO) system containing both EO emitter and detector. (b) Pure photoconductive antenna (PCA) system containing both PCA emitter and detector.

The steep learning curve combined with the labour required to custom-build a new system has prompted the emergence of commercial proprietary systems. A few commercial systems will be introduced in the following Subsection. However it should be noted that all pulsed THz systems, both custom-built and commercial, share an

optical framework consisting of mostly similar optical components, but each is ingeniously arranged to out-perform the others. The crux of any pulsed THz system is still the generation and detection of pulsed THz radiation—this is introduced in detail in Sections 3.2–3.5. A quick overview of optical components commonly used in pulsed systems is then given in Section 3.7.

3.1.2 Commercial Systems

An alternative to custom-building a THz system is to purchase a commercial system. There are several companies today that sell turn-key systems that are literally 'plug-and-play'. These systems are often comparable to custom-built systems in their spectral bandwidth and signal-to-noise ratio, and are usually more compact in size enabling their potential use outside the laboratory, such as at security check-points and hospitals.

NOTE:
These figures are included on page 56 of the print copy of the thesis held in the University of Adelaide Library.

(a) PB7100 Frequency Domain THz Spectrometer from Emcore Corp.

(b) Compact THz Spectrometer from Microtech Instruments Inc.

Figure 3.2: Examples of commercial pulsed THz systems. (a) This system is reported to have a spectral range from 0.1 THz to 2 THz, and has a frequency resolution of less than 0.25 GHz. The components of the system are: (1) THz source head; (2) THz detector head; (3) Control electronics; (4) Lock-in amplifier; (5) Control and data acquisition computer; (6) Optical breadboard with 2 parabolic mirrors on 5-axes translation stages. After Emcore Corporation (2008). (b) The spectral range of this system is reported to be between 0.1 THz to 1.5 THz, and its frequency resolution between 0.001–0.01 GHz. After Microtech Instruments Inc. (2008).

Examples of commercial pulsed THz systems available today are shown in Figs. 3.2–3.4. The components and layout of the custom-built system is still evident in the underlying setup of most of these commercial systems.

NOTE:
These figures are included on page 57 of the print copy of the thesis held in the University of Adelaide Library.

(a) Modular THz Spectrometer from T-ray Science (b) TPS Spectra 3000 from TeraView

Figure 3.3: Examples of portable commercial pulsed THz systems. (a) This modular system resembles a custom-built system but is extremely compact. It has a spectral range from 0.1 THz to 3 THz. After T-Ray Science (2008b). (b) This fully enclosed system, which is the size of an office photocopying machine, resembles a Fourier Transform Infrared (FTIR) system in both its appearance and ease of use. After TeraView Ltd (2008).

NOTE:
These figures are included on page 57 of the print copy of the thesis held in the University of Adelaide Library.

(a) Picometrix's T-Ray 4000 System operating in reflection mode

(b) Multiplexed Picometrix system with multiple THz sensor heads

Figure 3.4: Example of a fibre-coupled commercial pulsed THz system. (a) The THz sensors of this system are fibre-coupled to the controller. This makes it very versatile for use in both transmission and reflection modes. This picture shows a security application where a concealed weapon is detected. After Federici *et al.* (2008). (b) Accessories such as this multiplexer allows an array of sensor heads to perform simultaneous scans of different sites, such as on a production line. After Duling III and Zimdars (2007).

The obvious disadvantage of a commercial system is the lack of access to the components inside the system, as well as lack of access to software source-code. Users run the risk of nullifying a system's warranty if a sealed unit is opened. Nonetheless, commercial systems undoubtedly provide a launching pad to broaden the range of THz applications.

3.2 Nonlinear Materials

In order to understand how pulsed THz radiation is emitted and detected, it is necessary to delve into each of the fundamental physical phenomena that plays a role in the generation of pulsed THz radiation. Note that the detection of pulsed THz radiation often utilises the same techniques as generation, but in reverse. A good starting point for discussing THz generation and detection is nonlinear materials.

Prior to 1961, it was believed that all optical materials were linear. This means that if a vector field, such as an electric field $\mathbf{E}$, is incident on an optical medium, then the outgoing vector field has a linear relation to the input vector field. This should also hold true for an incoming electric field $\tilde{\mathbf{E}}(t)$ that varies rapidly over time:

$$\tilde{\mathbf{P}}(t) \;=\; \chi^{(1)}\,\tilde{\mathbf{E}}(t)\,, \tag{3.1}$$

where $\tilde{\mathbf{P}}$ is the outgoing polarisation vector that also varies rapidly over time, and $\chi^{(1)}$ is a scalar constant called the linear electric[27] susceptibility. Furthermore, the propagation of light in linear materials is governed by the linear three-dimensional wave equation:

$$\nabla^2\tilde{\mathbf{E}}(t) \;-\; \frac{1}{c^2}\frac{\partial^2\tilde{\mathbf{E}}}{\partial t^2} \;=\; 0, \tag{3.2}$$

which implies that the strict rules of classical optics, such as superposition, cannot be broken in linear optical media.

The existence of nonlinear materials was unconfirmed at the time because of the lack of high intensity, monochromatic light sources. Nonlinearity could not be observed with low intensity light sources, hence the belief in the linearity of all materials held fast and true.

However, this belief was turned on its head as a result of the invention of the maser in 1954, and subsequently the laser (Section 1.3.1). High intensity, monochromatic optical

[27] See Appendix B for more information on $\chi^{(1)}$.

masers (i.e. lasers) were available by 1960 and scientists were quick to utilise this new source of high intensity light to investigate optical materials. The exact discovery date of nonlinear media is vague because nonlinearity was never reported *per se*, however the first indirect confirmation of nonlinearity was reported by Franken *et al.* in 1961 through the observation of optical harmonics in quartz.

Nonlinear optical materials do not obey Equation (3.1). The relationship between an outgoing field vector and the incoming field vector in a nonlinear material is given by the following power series instead

$$\tilde{P}(t) \;=\; \chi^{(1)}\,\tilde{E}(t) + \chi^{(2)}\,\tilde{E}^2(t) + \chi^{(3)}\,\tilde{E}^3(t) + \chi^{(4)}\,\tilde{E}^4(t) + \cdots, \tag{3.3}$$

where the scalar quantities of $\tilde{\mathbf{E}}$ and $\tilde{\mathbf{P}}$ are used in Equation (3.3) for simplicity (Yariv 1989, Boyd 2003). Note that $\chi^{(2)}$ and $\chi^{(3)}$ are the second- and third-order scalar electric susceptibility[28] respectively (Boyd 2003). Equation (3.3) can be used to derive a version of the wave equation for nonlinear media (Boyd 2003, Saleh and Teich 1991):

$$\nabla^2\tilde{\mathbf{E}}(t) \;-\; \frac{1}{c^2}\frac{\partial^2\tilde{\mathbf{E}}}{\partial t^2} \;=\; \frac{1}{\mu}\frac{\partial^2\tilde{\mathbf{P}}}{\partial t^2}, \tag{3.4}$$

which implies that the principle of superposition does not hold inside a nonlinear medium, the ramifications being that:

- The dielectric properties (e.g. refractive index, and therefore the speed of light) inside a nonlinear medium can change nonlinearly according to the intensity of the incoming field $\tilde{E}(t)$.
- The frequency of $\tilde{E}(t)$ can be altered after passing through a nonlinear medium.
- Light can be used to control light; photons can interact with each other (Saleh and Teich 1991).

3.2.1 Noncentrosymmetrical Crystals

The family of nonlinear materials is large and is comprised of both organic and non-organic[29] materials: crystals, glasses, nanoparticles, polymers, liquids, metals, air, and vacuum.

[28] See Appendix B for sample values of $\chi^{(2)}$ and $\chi^{(3)}$.
[29] See Appendix B for a more comprehensive list.

The family of nonlinear crystals is itself varied, consisting of 32 distinct classes which can be divided into two subgroups: those with a centre of symmetry (*centrosymmetrical*, i.e. having inversion symmetry), and those without one (*noncentrosymmetrical*, i.e. lacking inversion symmetry). Noncentrosymmetrical crystals[30] are of interest in this Thesis because:

1. Second harmonic generation occurs in noncentrosymmetrical crystals, which is needed for optical rectification.
2. Noncentrosymmetrical crystals exhibit the Pockels effect, which in conjunction with second harmonic generation and optical rectification, is the basis for THz generation and detection in both photoconductive antenna and electro-optic THz systems.

Second harmonic generation, optical rectification, and the Pockels effect will be introduced in the following Sections.

3.3 Optical Harmonics: Second Harmonic Generation

In 1961, Franken *et al.* discovered that optical harmonics can be generated in materials that (i) have nonlinear dielectric coefficients, (ii) are noncentrosymmetrical, and (iii) exhibit transparency to both the fundamental frequency and the harmonics of the incident optical light.

To explain the generation of optical harmonics, Equation (3.3) is reproduced here for convenience:

$$\tilde{P}(t) = \chi^{(1)}\,\tilde{E}(t) + \chi^{(2)}\,\tilde{E}^2(t) + \chi^{(3)}\,\tilde{E}^3(t) + \chi^{(4)}\,\tilde{E}^4(t) + \cdots . \quad \text{[Equation (3.3)]}$$

If the incident light source is monochromatic, then $\tilde{E}(t)$ is sinusoidal with fundamental angular frequency $\omega_0 = 2\pi\nu_0$ (where ν_0 is the fundamental frequency in Hertz). This means $\tilde{P}(t)$ in Equation (3.3) contains harmonics of ω_0 because of the nonlinear terms $\tilde{E}^2(t), \tilde{E}^3(t), \tilde{E}^4(t), \cdots$:

$$\tilde{P}(t) = \underbrace{\chi^{(1)}\,\tilde{E}(t)}_{\omega_0 \text{ term}} + \underbrace{\chi^{(2)}\,\tilde{E}^2(t)}_{2\omega_0 \text{ term}} + \underbrace{\chi^{(3)}\,\tilde{E}^3(t)}_{\omega_0 \text{ and } 3\omega_0 \text{ terms}} + \underbrace{\chi^{(4)}\,\tilde{E}^4(t)}_{4\omega_0 \text{ term}} + \cdots . \quad \text{[Equation (3.3)]}$$

[30] Of the 32 classes of nonlinear crystals, 20 lack a centre of symmetry. These 20 classes are also piezoelectric (Hecht 2002).

In centrosymmetrical crystals, the even harmonics vanish ($\chi^{(2)} = \chi^{(4)} = 0$), leaving behind only odd harmonics. Therefore, second harmonic generation cannot occur in centrosymmetrical crystals. Detailed reasons as to why the even harmonics vanish can be found in Boyd (2003) and will not be elaborated here.

In noncentrosymmetrical crystals, neither the even nor odd harmonics vanish. The second harmonic is most important amongst all the harmonics in Equation (3.3) because it has been shown mathematically, through the use of quantum-mechanical perturbation theory, that all power from the incident light source can be converted into the second harmonic term (Armstrong *et al.* 1962). As a result, Equation (3.3) simplifies to

$$\tilde{P}^{\mathrm{NL}}(t) = \chi^{(2)}\,\tilde{E}^2(t)\,, \tag{3.5}$$

where NL denotes nonlinearity.

The second and other even harmonics in Equation (3.3) are of interest because direct-current (DC) polarisation accompanies them. This means that the induced polarisation $\tilde{P}$ of the even harmonics are constant over time, akin to current produced in an electronic AC-to-DC rectifier (Bass *et al.* 1962). This process, called optical rectification, will be explained in the next Subsection but only the second harmonic will be considered.

3.3.1 Optical Rectification (OR)

When the incident light source is monochromatic, $\tilde{E}(t)$ will be sinusoidal with fundamental angular frequency ω_0:

$$\tilde{E}(t) = E\,\cos(\omega_0 t) = \frac{1}{2}\left(E\,e^{-i\omega_0 t} + E\,e^{i\omega_0 t}\right) = \frac{1}{2}E\,e^{-i\omega_0 t} + \frac{1}{2}E\,e^{i\omega_0 t}. \tag{3.6}$$

Substituting Equation (3.6) into Equation (3.5) gives:

$$\begin{aligned}
\tilde{P}^{\mathrm{NL}}(t) &= \chi^{(2)}\left[\frac{1}{2}E\,e^{-i\omega_0 t} + \frac{1}{2}E\,e^{i\omega_0 t}\right]^2 \\
&= \chi^{(2)}\left[\frac{2}{4}E^2 + \frac{1}{4}E^2\,e^{i2\omega_0 t} + \frac{1}{4}E^2\,e^{-i2\omega_0 t}\right] \\
&= \underbrace{\frac{1}{2}\chi^{(2)}E^2}_{\text{DC term}} + \underbrace{\frac{1}{2}\chi^{(2)}E^2\cos(2\omega_0 t)}_{2\omega_0\text{ term}}\,.
\end{aligned} \tag{3.7}$$

The existence of two frequency components in Equation (3.7) is now apparent: the $\chi^{(2)}E^2$ term is the DC component; the $\chi^{(2)}E^2\cos(2\omega_0 t)$ term has a frequency of $2\omega_0$, hence is the second harmonic component. The implications of Equation (3.7) are:

1. The input frequency ω_0 has doubled in the process of passing through a nonlinear, noncentrosymmetrical crystal, thus second harmonic generation is also referred to as *frequency doubling*. As will be seen in Section 3.4, the second harmonic component affects the refractive index encountered by the extraordinary (e) ray.

2. The nonlinear medium has effectively rectified the sinusoidal in the same way as an AC-to-DC electronic rectifier converts AC voltage to a DC one. This process is called optical rectification (OR). This DC term creates a DC potential across the crystal, hence it is not emitted from the crystal.

Optical rectification is a precursor for THz generation. However the OR process that occurs in THz systems is slightly different from that described above because a pulsed laser is used instead of a monochromatic laser. Terahertz optical rectification will be introduced in Section 3.5.

For completeness, three other requirements are needed for high quality second harmonic generation in addition to nonlinearity, noncentrosymmetricity, and transparency to the fundamental optical frequency and its harmonics (He and Liu 1999):

- $\chi^{(2)}$ should be large so that both the DC and second harmonic terms will be large.
- High optical damage threshold in order to withstand high incident power.
- Good phase matching so that the refractive indices at DC and the second harmonic are similar.

3.4 The Pockels Effect (Linear Electro-Optic Effect)

The discovery of nonlinearity in optical media may have arrived late in history, but this certainly did not hinder the discovery of electro-optics, which has been studied extensively since the 19th century. Electro-optics is the study of the modification of a material's optical properties when an electric field is applied. The history trail can be traced even further back when birefringence is considered. The Pockels effect is based on the concept of birefringence, which was observed in the 17th century by Erasmus Bartholinus (Rasmus Bartholin) and Christiaan Huygens.

Birefringence means that a material has two refractive indices. Birefringence can occur in materials that are *uniaxial*—having one axis of rotational symmetry, which is called the *optical axis* or *Z-axis* or *c-axis* of the crystal (Dmitriev *et al.* 1999). For example, calcite (Iceland spar), has two refractive indices in the visible frequency range of 589 nm: 1.658 along its optical axis, and 1.486 along its unique *extraordinary axis*. At 589 nm, the extraordinary axis is offset from the optical axis by 6.2° (Hecht 2002).

The mechanism for birefringence is as follows. A typical incoming single wavefront has two orthogonal polarisation components: parallel ('*p*'), and perpendicular ('*s*', which stands for *senkrecht* in German). In a non-birefringent material, the *p* and *s* components travel along the optical axis together, and exit the material simultaneously. In calcite however, the *p* and *s* components 'split up' to travel either along the optical axis or the extraordinary axis. Since the refractive indices of the axes are not equal, the *p* and *s* components travel at different velocities and exit the calcite at different times and locations. In other birefringent materials, the polarisation of the two exiting beams can also differ. In summary, a simple birefringent material splits the incident *p* and *s* components into two wavefronts called the *ordinary*-ray (*o*-ray) and *extraordinary*-ray (*e*-ray).

In 1893, Friedrich Pockels discovered that noncentrosymmetrical crystals are birefringent, but they differed from other birefringent crystals in three ways:

- In order to induce birefringence in the crystal, an electric field needs to be applied across the crystal when the incident beam of light enters the crystal. The applied field can either be constant (DC) or varying (AC).
- The extent of birefringence is proportional to the 'first power' of the electric field (hence the Pockels effect is considered a linear electro-optical effect, not nonlinear).
- In the absence of the electric field, the crystal has only one refractive index n_o that is orientation-independent (note the subscript is an 'o' to denote the *o*-ray).

The second point listed above can be explained in the context of second harmonic generation. Consider the application of an incident monochromatic light source $\tilde{E}(t)$ and an externally applied DC electric field with amplitude E_{ext} on a noncentrosymmetrical crystal. Substituting this input into Equation (3.5) gives:

$$\begin{aligned}\tilde{P}^{\mathrm{NL}}(t) &= \chi^{(2)}\left[E_{\mathrm{ext}} + E\,e^{-i\omega_0 t} + E\,e^{i\omega_0 t}\right]^2 \\ &= \underbrace{\chi^{(2)}\left(E_{\mathrm{ext}}^2 + 2E^2\right)}_{\text{DC term}} + \underbrace{4\chi^{(2)}E_{\mathrm{ext}}E\cos(\omega_0 t)}_{\omega_0\text{ term}} + \underbrace{2\chi^{(2)}E^2\cos(2\omega_0 t)}_{2\omega_0\text{ term}} \\ &= P^{\mathrm{NL}}(0) + P^{\mathrm{NL}}(\omega_0) + P^{\mathrm{NL}}(2\omega_0).\end{aligned} \tag{3.8}$$

If the optical field $\tilde{E}(t)$ is much weaker than E_{ext} (e.g. monochromatic laser), then $P^{\mathrm{NL}}(2\omega_0)$ can be ignored, resulting in a system consisting of only a DC term and a linear first-order term. Since the DC term's role is to create a DC potential across the crystal and it is not emitted from the crystal, the polarisation of the emitted field is only influenced by the linear first-order term, hence the Pockels effect is a linear EO effect.

3.4.1 Influence of the Pockels Effect on the Polarisation Axes

A generic example of a noncentrosymmetrical, uniaxial crystal is shown schematically by the cube in Fig. 3.5. The applied external electric field $\mathbf{E}_{\mathrm{ext}}$ with amplitude E_{ext} is applied along the optical axis, which is the z-axis in this example.

The optical properties of this crystal can be described by a set of *relative impermeability tensors* $\boldsymbol{\eta}_{ij}$, where the Cartesian indices $i, j = 1, 2, 3$. The tensor $\boldsymbol{\eta}_{ij}$ is a function of $\mathbf{E}_{\mathrm{ext}}$. In the absence of $\mathbf{E}_{\mathrm{ext}}$, $\boldsymbol{\eta}_{ij}$ generates a geometrical shape that is either spherical (isotropic crystals) or elliptical (anisotropic crystals). The shape is called the refractive index spheroid (or ellipsoid). In the field of THz, both isotropic and anisotropic crystals are used. However, the isotropic crystals used in THz experiments become uniaxial under the influence of the Pockels effect. Examples of isotropic crystals commonly used in THz experiments are zinc blende crystals, such as gallium arsenide (GaAs) and zinc telluride (ZnTe); anisotropic crystal frequently used in THz studies are lithium niobate ($LiNbO_3$) and lithium tantalate ($LiTaO_3$) (Kaminow and Turner 1971).

Let the example shown in Fig. 3.5 be GaAs (Saleh and Teich 1991). In the absence of $\mathbf{E}_{\mathrm{ext}}$, the refractive index n_{o} of GaAs is the same along all three axes: $n_x = n_y = n_z = n_{\mathrm{o}}$. The relationship between n_x, n_y and n_z is therefore given by the equation of a sphere:

$$\frac{x^2}{\text{radius}^2} + \frac{y^2}{\text{radius}^2} + \frac{z^2}{\text{radius}^2} = 1 \quad \Rightarrow \quad \frac{x^2}{n_x^2} + \frac{y^2}{n_y^2} + \frac{z^2}{n_z^2} = 1.$$

Using only x notation for the Cartesian coordinates:

$$\frac{x_1^2}{n_1^2} + \frac{x_2^2}{n_2^2} + \frac{x_3^2}{n_3^2} = 1, \tag{3.9}$$

and in tensor form:
$$\sum_{i=j} \eta_{ij}\, x_i\, x_j \;=\; 1, \quad i,j = 1,2,3 \tag{3.10}$$

$$\text{where} \quad \eta_{ij} \;=\; \frac{1}{n_i n_j}\,. \tag{3.11}$$

The tensors $\boldsymbol{\eta}_{ij}$ can therefore be thought of as generating a refractive index spheroid as shown by the yellow sphere in Fig. 3.5. For anisotropic crystals, i is not necessarily equal to j in Equation (3.10).

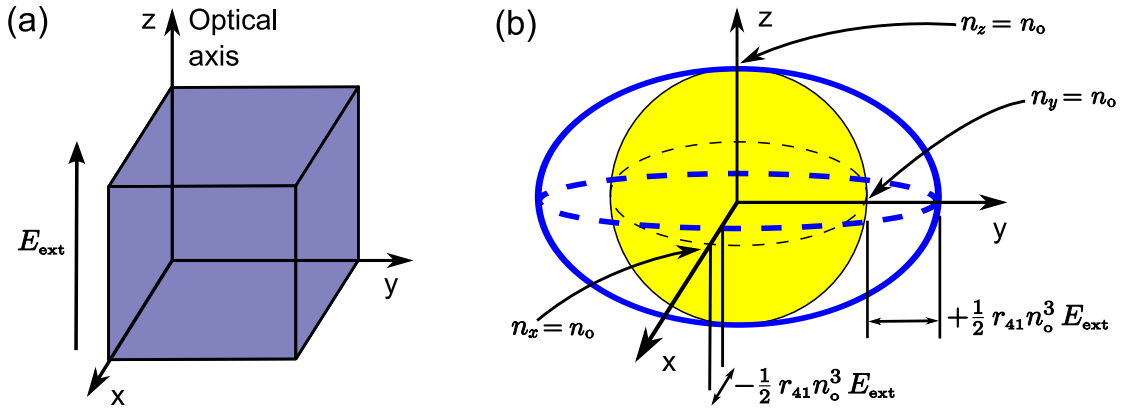

Figure 3.5: The Pockels Effect in a noncentrosymmetrical crystal. (a) A cubic $\bar{4}$3m ('m' does not mean meters; it is a convention used in crystallography to describe crystal symmetry—see Appendix Section B.3.3) crystal, such as GaAs or InAs, has the same refractive index in all 3 axes ($n_x = n_y = n_z = n_o$) in the absence of an applied electric field $\mathbf{E}_{ext}$ with amplitude E_{ext}, hence the crystal behaves isotropically. (b) Without $\mathbf{E}_{ext}$, the tensors $\boldsymbol{\eta}_{ij}$ of the crystal generate a refractive index spheroid (illustrated by the yellow sphere). This spheroid intersects the 3 axes at n_x, n_y, and n_z. A light source passing through the crystal along the optical axis (z axis for this example) will intersect the spheroid on a plane that is shaped like a disk (dotted thin black line inside spheroid). The light emerging from the crystal is linearly polarised and only contains one ray: the *o*-ray. If $\mathbf{E}_{ext}$ is now applied in the z direction, the refractive indices along the x and y axes are altered such that the shape of refractive index spheroid is distorted to become an ellipsoid (thick blue line). This ellipsoid intersects the x and y axes at new locations as shown; only the original n_z is preserved. The crystal is now birefringent; when an incident light source travels through the crystal along the optical axis (z axis), its x and y components will encounter two different refractive indices, hence will travel through the crystal at different speeds. A second ray, the *e*-ray, is now present in addition to the *o*-ray. The plane on which the incident light intersects with the ellipsoid is shaped like an ellipse (dotted thick blue ellipse), hence the emerging *e* and *o*-rays are elliptically polarised. After Saleh and Teich (1991).

When a constant or varying $\mathbf{E}_{\text{ext}}$ is applied to a noncentrosymmetrical crystal along its optical axis (the z axis for the example shown in Fig. 3.5), the refractive index along all 3 axes may change. In this example, GaAs becomes uniaxial, so only n_x and n_y are altered; n_z remains the same. The changes in n_x and n_y are unequal, resulting in the refractive index spheroid being distorted into an ellipsoid. The ellipsoid intersects the x and y axes at the new values of n_x and n_y respectively. The extent at which n_x and n_y change is determined by the properties of a crystal's class (Saleh and Teich 1991):

$$n(E_{\text{ext}}) \approx n_{\text{o}} - \frac{1}{2}\mathbf{r}_{ijk}\, n_{\text{o}}^3\, E_{\text{ext}} \quad \Rightarrow \quad \Delta n = -\frac{1}{2}\mathbf{r}_{ijk} n_{\text{o}}^3 E_{\text{ext}}\,, \tag{3.12}$$

where r_{ijk} is the frequency dependent, crystal-class dependent property known as the Pockels coefficient (or linear electro-optic coefficient), and $i,j,k = 1,2,3$. For GaAs, $r_{ijk} = r_{321} = 1.6 \times 10^{-12}$ m/V at 28.3 THz (Yariv 1989), and the modified refractive indices along the x and y axes due to the Pockels effect are:

$$\begin{aligned}
n_x(E_{\text{ext}}) &\approx n_{\text{o}} - \frac{1}{2}\mathbf{r}_{321}\, n_{\text{o}}^3\, E_{\text{ext}} \quad &\Rightarrow \quad \Delta n_x &= -\frac{1}{2}\mathbf{r}_{41}\, n_{\text{o}}^3\, E_{\text{ext}} \\
n_y(E_{\text{ext}}) &\approx n_{\text{o}} + \frac{1}{2}\mathbf{r}_{321}\, n_{\text{o}}^3\, E_{\text{ext}} \quad &\Rightarrow \quad \Delta n_y &= +\frac{1}{2}\mathbf{r}_{41}\, n_{\text{o}}^3\, E_{\text{ext}} \\
n_z(E_{\text{ext}}) &= n_{\text{o}} = 3.34 \quad &\Rightarrow \quad \Delta n_y &= 0,
\end{aligned}$$

where r_{41} is equivalent to r_{321} but written in single index notation. The Pockels effect may change the refractive indices in all 3 axes for other crystal classes, such as in lithium niobate ($LiNbO_3$), which is affected by its r_{113} and r_{333} Pockels coefficients. More in-depth discussion of crystallography and the Pockels coefficients of various crystals is outside the scope of this Thesis. Additional information can be found in Kaminow and Turner (1971), Kaminow (1974) and Yariv (1991).

In the presence of $\mathbf{E}_{\text{ext}}$, the x and y components of an incident light source passing through the crystal along the optical axis (z axis) will encounter the new n_x and n_y values. Since n_x and n_y are not usually equal, the x and y components will propagate through the crystal at different speeds, hence birefringence ensues with the emergence of an *e*-ray in addition to the original *o*-ray.

The plane of intersection between the incident light and the ellipsoid is an ellipse, hence the emerging *e* and *o*-rays are elliptically polarised. However, in the absence of $\mathbf{E}_{\text{ext}}$, the sole *o*-ray is linearly polarised. The elliptical plane is of most interest because it exists only when the Pockels effect occurs. In the context of pulsed THz-TDS systems, the absence of THz radiation results in a refractive index spheroid, whereas the existence of the elliptical plane indicates the presence of THz radiation (Section 3.10.2). In

Sections 3.10.3–3.10.5, it will be shown that the major and minor axes of this elliptical plane is sampled/detected during EO THz detection.

3.4.2 Absence of Applied External Field in EO Systems

In EO THz generation, $\mathbf{E}_{\text{ext}}$ is absent, but the ultrafast laser pulses incident on the non-centrosymmetrical crystal create shock waves inside the crystal (Auston 1983, Kleinman and Auston 1984). The shock waves manifest as high voltage electrical transients (spikes), which move through the material with a wavefront that has a Čerenkov-like cone shape (Auston *et al.* 1984b). These electrical transients are therefore analogous to $\mathbf{E}_{\text{ext}}$, and are responsible for the creation of the (applied) electric field needed for the Pockels effect. Čerenkov-like shockwaves will be discussed in Section 3.6.

3.5 Generation and Detection of Subpicosecond Pulses

The confirmation of nonlinearity in optical media in 1961 unfurled many new and exciting research projects into the properties and uses of nonlinear materials. However one obstacle existed: poor understanding of the theoretical formulation of the physical mechanisms of second harmonic generation, particularly with respect to changes in polarisation. Conjectures were presented and debated for several years (Kleinman 1962, Armstrong *et al.* 1962, Bloembergen and Pershan 1962, Franken and Ward 1963). In 1965, Nicolaas Bloembergen bravely published the first text book on nonlinear theory.

The theory in Bloembergen's book provided a spring-board for more sophisticated nonlinear research, such as the generation of far-infrared (FIR) radiation in nonlinear crystals through the use of continuous-wave lasers (Zernike Jr. and Berman 1965, Faries *et al.* 1969, Zernike 1969). With the advent of dye and mode-locked (pulsed) lasers in the late 1960s, laser pulses were subsequently used to generate short bursts of FIR radiation from nonlinear crystals.

Pulse laser technology was progressing quickly at the time: laser pulsewidths decreased dramatically from 10 ns (Yarborough *et al.* 1969) to 5 ps (Yang *et al.* 1971) within a few years. However detection of FIR radiation pulses was still a challenge due to slow response time of existing detectors; spectrometers and FIR interferometers were

still relied upon (Yarborough *et al.* 1969, Auston 1971, Yang *et al.* 1971). Picosecond optoelectronic detectors were therefore highly sought after.

3.5.1 Photodetectors for Picosecond Pulses: the Auston Switch

The development of picosecond optoelectronic detectors is very much intertwined with that of the picosecond switch. David H. Auston, who in the 1960s was instrumental in developing mode-locking in lasers (Auston 1968b, Auston 1968a) and current generation in semiconductor transmission lines (Auston and Glass 1972), pioneered the first picosecond switch in 1975 using semiconductor microstrip technology. This switch, as shown in Fig. 3.6, is commonly known as the Auston switch. It is a structurally simple device that cleverly relies on *photoconductivity*, i.e. the resistivity of a semiconductor in a strong electric field can be modified to a certain physical depth that is dependent on the wavelength of the incident laser light.

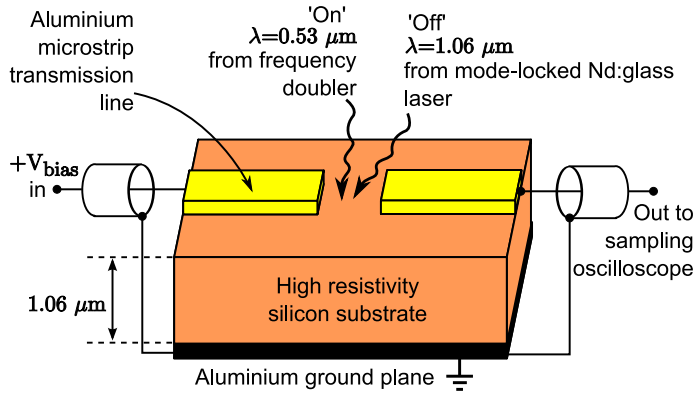

Figure 3.6: The Auston switch. A conducting channel forms at a depth similar to the 0.53 μm wavelength of the incident optical light pulse, bridging the gap between the microstrip transmission lines. This effectively closes the switch ('on'). The second light pulse opens the switch ('off') because a new conducting channel forms at a depth equal to the 1.06 μm, which is the depth of the ground plane. This means the transmission line is shorted to ground, hence conduction across the gap ceases. After Auston (1975).

Although the principle of photoconductivity will be explained later in Section 3.8 in the context of photoconductive antennas, the brilliance of the Auston switch can still be appreciated here: one optical light pulse, at a wavelength of 0.53 μm, turns the switch on because a highly conducting thin layer forms under the surface of the silicon at a depth of ≈ 0.53 μm. This thin layer contains a high density of carriers with conductivity of quasimetallic properties, but with a lifetime of only a few picoseconds. This

means a conductive channel is bridged across the microstrip transmission line gap for only a few picoseconds, closing the switch (switch is on).

A second delayed optical light pulse at double the wavelength of the first pulse, turns the switch 'off' because the conducting thin layer at depth ≈ 1.06 μm is now on the ground plane; this shorts the transmission line and stops conduction across the gap. The overall optical gating effect allows rapid switching of the semiconductor with ultrafast laser pulses.

The optical gating technique was quickly adopted and extended by other researchers (Lee *et al.* 1977, Leonberger and Moulton 1979). One useful extension is the sampling of the impulse response of fast photodiodes (Antonetti *et al.* 1977b). This work was further extended to high voltage picosecond switching in a Pockels cell (Antonetti *et al.* 1977a)—the impact of this work will be evident in Section 3.5.2.

In 1980, a high-speed photodetector based on the concept of the Auston switch was unveiled (Auston *et al.* 1980b). The semiconductor material of the photodetector was modified from the original Auston switch so as to achieve faster switching time. The physics behind the photodetector was the formation and dissipation of very short electrical pulses called *electrical transients* in the semiconductor material. These electrical transients produce the detection effect, hence the faster the transition time, the faster the detection.

The photodetector's switching time however was severely limited by the speed of the sampling oscilloscope that measured the rapidly changing voltage across the microstrips. The sampling time of the oscilloscope was ≈ 25 ps—too slow to accurately capture the electrical transients, which were calculated to be 8 ps. In order to bypass the sampling oscilloscope, new microstrip patterns were explored in order to perform pulse sampling and autocorrelation within the confines of the photodetector (Auston *et al.* 1980a). This latter technique would become the basis for photoconductive antenna-based THz detection, which is described in Section 3.8.2.

3.5.2 Subpicosecond EO Sampling System

A solution to Auston's sampling oscilloscope problem arrived in 1982. The early work of Antonetti *et al.* in 1977 and of Mourou *et al.* in 1981, provide the foundation of the novel picosecond electro-optic (EO) sampling system devised by Valdmanis *et al.* This system is shown in Fig. 3.7.

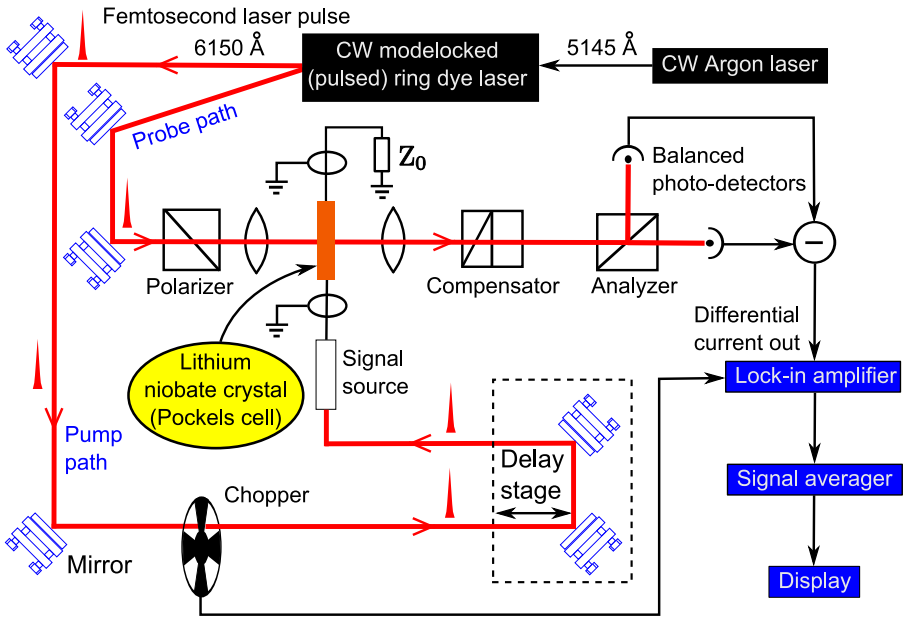

Figure 3.7: Electro-optic sampling system for detecting electrical transients. This EO sampling system was originally designed to detect and measure electrical transients in nonlinear media. However, it proved to be the solution for EO detection of THz radiation. It is now commonly seen in THz systems utilising EO detection. After Valdmanis *et al.* (1982).

The EO sampling system circumvents the picosecond lower limit of electrical transients by using a Pockels cell. A Pockels cell utilises the Pockels effect in a crystal (Section 3.4) to achieve ultrafast switching because the Pockels effect occurs within femtoseconds—3 orders of magnitude faster than electrical transients in semiconductors. Additionally, birefringence from the Pockels effect causes asymmetry in polarisation (Section 3.4.1), which can be detected using balanced photodiodes (Section 3.8.2). Picosecond switching can therefore be monitored by observing the differential current from balanced photodiodes, removing the need for further signal processing.

The temporal resolution achieved was under 4 ps in 1982; a year later, subpicosecond temporal resolution was attained (Valdmanis *et al.* 1983, Valdmanis and Mourou 1986). Electro-optic sampling became the preferred detection technique for ultrafast electromagnetic radiation until the maturity of photoconductive antenna-based detection in 1988. The layout of the original subpicosecond EO sampling system is still preserved

in EO detection THz systems of today. The Auston switch[31] and EO sampling are milestones in the history of THz technology.

3.6 Terahertz in Nonlinear Material: Čerenkov Sampling

The early work in the 1960s and 1970s on the generation of FIR radiation in crystals (Section 3.5) evolved with the availability of new semiconductor materials and sampling techniques. For example, microwave pulses could be generated and detected using EO sampling (Mourou *et al.* 1981a, Mourou *et al.* 1981b); Auston's photodetector could work as both a generator and detector of millimeter waves through the use of dielectric resonators (Auston and Smith 1983); electromagnetic emission of pulsed radiation was possible using Auston's photodetectors through the use of photoconducting Hertzian dipoles, hence Auston's photodetectors were now *photoconductive-emitters* (Auston *et al.* 1984a). The arrival of pulsed THz was imminent.

Earlier in 1981, Auston's team discovered that radiation damage (Section 3.8.3) in semiconductors could reduce electrical transient times (Smith *et al.* 1981). This work would become instrumental in the historical 1984 experiment where radiation damaged lithium tantalate ($LiTaO_3$) crystal provided the ideal conditions for the generation of Čerenkov-like cone shaped shockwaves (Kleinman and Auston 1984, Auston *et al.* 1984b, Auston and Nuss 1988).

The 1984 breakthrough experiment produced the inaugural pulsed THz signal with a bandwidth of 4 THz. The generation of THz radiation in this experiment occurs when a beam of laser pulses with femtosecond pulsewidth are incident on radiation damaged $LiTaO_3$—this beam is called the pump beam. This causes very short electrical transients to be generated in the crystal, resulting in the emission of extremely fast electromagnetic radiation pulses. The emitted radiation has polarisation with a Čerenkov-like cone shape, and has frequencies in the THz range. Although the emitted radiation moves together with the pump beam, the polarisation cone fans out behind the wavefront, resulting in birefringence in the region enclosed by this cone. This birefringence is vital in the detection of the THz radiation.

A second incident beam of laser pulses—the probe beam—is slightly offset in position from the pump beam and is also slightly delayed. The probe beam is affected by

[31] The Auston switch is also used in other non-THz related fields, such as picosecond scanning tunnelling microscopy (Steeves *et al.* 1997).

the birefringence caused by the pump beam, therefore the polarisation of the emerging probe beam is distorted accordingly (Section 3.4.1). By using Valdmanis' fast EO sampling technique (based on the concept of birefringence in a Pockels cell), the extent of distortion provides a direct measure of the strength of the THz radiation, hence coherent detection of THz radiation is achieved, albeit performed inside the crystal.

The experiment, formally known as EO Čerenkov[32] sampling, indeed heralded the generation and detection of pulsed THz radiation in nonlinear materials.

By 1985, a coherent time-domain FIR spectroscopic technique based on EO Čerenkov sampling was developed (Auston and Cheung 1985). This coherent system allowed the extraction of the optical properties of semiconductor materials without the need for the Kramers-Kronig relation (Cheung and Auston 1986). The EO Čerenkov sampling system however had one drawback: total internal reflection of THz radiation at the crystal boundaries. Coherent detection had to be performed inside the crystal because it was not always possible to couple the THz radiation out into free-space. There was now a need to develop a free-space pulsed Čerenkov sampling system. However, this need was somewhat overshadowed (though not forgotten) by the introduction of the Hertzian dipole in 1984, also by Auston (Section 3.8), which paved the way for the photoconductive antenna (PCA). It would take another 4 years before the debut of the first free-space pulsed Čerenkov sampling system.

In 1989, Fattinger and Grischkowsky addressed the problem of total internal reflection in Čerenkov sampling by using cylindrical lenses, allowing the emission of THz radiation into free-space. This technique was subsequently improved by changing the incident angle of the femtosecond laser pulses into the nonlinear crystal (Hu *et al.* 1990b). The success of Čerenkov sampling renewed interest in the 1960s' and 1970s' work on the generation of FIR radiation in crystals (Section 3.5) as alternatives to the blossoming PCA-based THz emission and detection. The alternative that emerged is electro-optic (EO) THz generation and detection.

The next Section will introduce the common components in the front end of both PCA and EO pulsed THz systems. The PCA system is then presented in Section 3.8, followed by the EO system in Sections 3.9 and 3.10.

[32] Also spelled Cherenkov. Named after the Russian physicist Pavel Alekseyevich Čerenkov who discovered the cone-shaped radiation emitted when a charged particle moves faster than the speed of light in an insulating medium. Note that there is no violation of special relativity as the charge is still slower than light *in vacuo*.

3.7 Common Optical Components in Pulsed Systems

This Section briefly introduces optical components that are common to both PCA and EO pulsed THz systems. These components are not unique to THz systems, therefore the depth of technical information covered will only be sufficient for the purposes of this Thesis. Where possible, references to technical literature are provided for further reading. Details of the specific components used to complete experiments for this Thesis are found in Appendix C.

3.7.1 Ultrafast Laser

The pulsing action of pulsed THz systems usually comes from a titanium-doped sapphire (Ti:Sapphire) femtosecond pulsed laser (also known as an *ultrafast laser*). The femtosecond laser, which is typically pumped by a green (532 nm) CW laser, emits very short laser pulses with pulsewidth of tens of femtoseconds (typically 100 fs), at a repetition rate in the range of 85–90 MHz (amplified femtosecond laser systems have kilohertz repetition rates). Each laser pulse typically contains frequencies between 690–1040 nm, with centre frequency at 780-800 nm.

Since only the lower frequency components around 720 nm are visible to the human eye, the laser pulses appear deceptively faint. The peak output power of most ultrafast lasers is actually extremely high ($>$ 450 kW), hence care is needed when working with ultrafast lasers. More details about laser safety can be found in Clarke (1971). Details on pulsed lasers (including dye lasers which preceded Ti:Sapphire lasers) can be found in Deutsch (1971), Weber (1971), Woodcock (1971), and manufacturers' websites (e.g. Coherent, Spectra-Physics, Femtolaser, Toptica Photonics).

3.7.2 Amplitude Modulation: Mechanical Chopper

As seen in both Figs. 3.1(a) and 3.1(b), the laser pulse is split into two paths—probe and pump—using a beamsplitter. The purpose of the probe path will be revealed in Section 3.8.2. The laser pulse on the pump path is amplitude modulated by a mechanical chopper as shown in Fig. 3.8. The chopper frequency chosen is usually one that is much higher than the typical noise frequency in the laboratory, and is not a harmonic of known noise frequencies. For example, fluorescent lamps, which are ubiquitous

in most laboratories, operate at either 50 or 60 Hz. A suitable chopper frequency is 2.78 kHz, because division by 50 or 60 Hz does not produce an integer result.

Laser noise is an inverse function of frequency (i.e. noise $\propto 1/\nu$), hence a high chopper frequency is desired. However, if the chopper frequency is too high, mechanical vibrations from the chopper can introduce additive noise into the measurements, thus cancelling out the chopper's benefits. Furthermore, amplitude modulators capable of very high frequencies can be substantially more expensive.

More details on the duty cycle of a mechanical chopper, and its effect on modulation can be found in Mendaš and Cvijin (1983) and Vincent (1986).

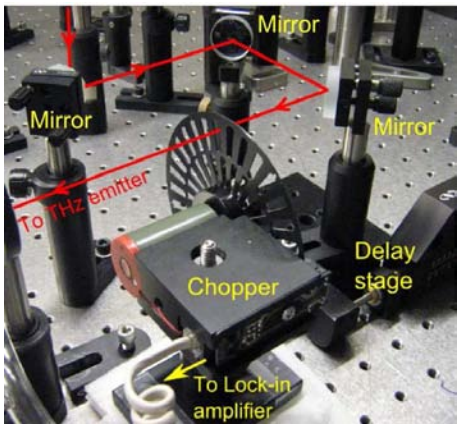

Figure 3.8: A typical chopper and delay stage in a THz system. The chopper shown is switched off to display the blades that modulate the laser pulses. The delay stage consists of a moving platform that is manoeuvred by a highly accurate motor. The mirrors mounted on the delay stage create a distinct U-shaped path for the pulsed laser beam. Equipment courtesy of X.-C. Zhang at RPI.

3.7.3 Delay Stage

The delay stage alters the propagation time of the probe path by a controlled, variable amount. The role of the delay is described in Section 3.8.2. It is sufficient to mention at this point that the delay stage is a mechanical platform as shown in Fig. 3.8 that moves in one axis in very small steps of typically 10 or 20 μm in distance. Better quality delay stages are capable of smaller step sizes, and also take less time to stabilise after each step is made.

3.7.4 Parabolic Mirrors

In Figs. 3.1(a) and 3.1(b), both the PCA and EO emitters generate divergent THz beams (illustrated in green). For the THz signal to be useful for spectroscopic investigation purposes, it needs to be either collimated or focused to a point. An off-axis parabolic

mirror is able to do this: it can either focus a parallel beam to a point, or diverge a point source to become parallel rays. Its off-axis characteristic ensures that the outgoing beam can be sent downstream to the next optical component without obstructing the parabolic mirror (Hecht 2002). If a collimated THz signal is desired, then only 2 parabolic mirrors are required: divergent to collimated, and after the sample, collimated to focused. For a focused THz signal, 4 parabolic mirrors are required as shown in Fig. 3.9: divergent to collimated, collimated to focused (e.g. on a target), and after the sample, focused to collimated, and finally collimated to focused.

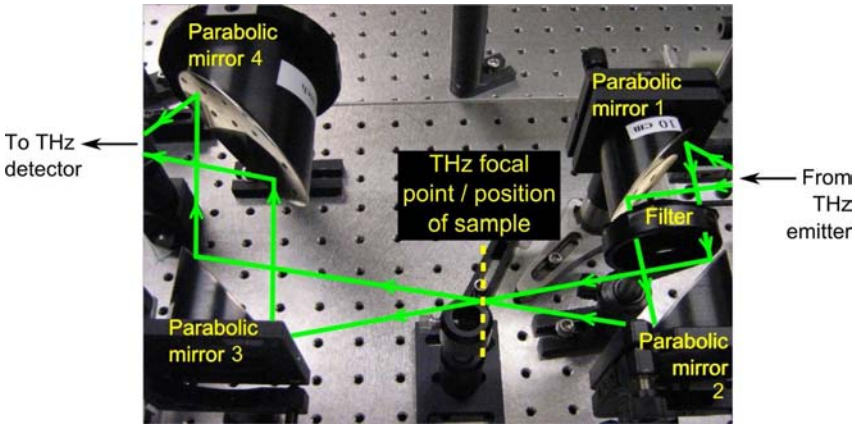

Figure 3.9: Four parabolics used to focus THz radiation to a point. The incoming radiation is from the THz emitter (either electro-optic or photoconductive). The outgoing radiation is focused either onto a beamsplitter (for electro-optic detection), or a photoconductive antenna. Equipment courtesy of X.-C. Zhang at RPI.

Two elliptical mirrors provide an alternative to the use of 4 parabolic mirrors for the focused case, but they are more expensive and more difficult to align (Khazan 2002).

3.8 Photoconductive Antenna (PCA) THz System

Photoconductive antenna technology began with the introduction of the picosecond photoconducting Hertzian dipole by Auston *et al.* in 1984. The picosecond photoconducting Hertzian dipole can be considered an improved version of the Auston switch (Section 3.5.1). The Auston switch contains a microstrip transmission line which has a geometry that supports TEM-like electromagnetic modes with low dispersion over a bandwidth of a few GHz—ideal for electrical transients of a few picoseconds. By modifying its design, other authors have succeeded in removing the need for a second pulse to turn the switch off (Platte 1976, Castagne *et al.* 1976). Fast switching times

below 10 ps have also been achieved by using new semiconductor materials, such as amorphous silicon (Auston *et al.* 1980b). Despite these improvements, electromagnetic radiation from an Auston switch is inextricably confined between the microstrip transmission lines, hence restricting its use in free-space.

A solution to overcome the free-space limitation is to couple the Auston switch to a waveguide. For example, emission of microwave pulses was demonstrated successfully this way using a X-band waveguide (Mourou *et al.* 1981a). The Hertzian dipole however does not require a waveguide hence is simpler in construction.

NOTE:
These figures are included on page 76 of the print copy of the thesis held in the University of Adelaide Library.

(a) Picosecond photoconducting Hertzian dipole

(b) Photoconducting dipole antenna

Figure 3.10: Development of the photoconducting dipole antenna. (a) The photoconducting Hertzian dipole is based on Heinrich Hertz's time-varying dipole (1893). A dipole, illustrated by the black rectangles, is located on each side of the structure. The emitter dipole is located on the left and the detector dipole on the right. Each dipole is mounted on a photoconducting film (shown in yellow in the electronic version of this Thesis). The incoming laser pulse $I(t)$ and $+V_{\text{bias}}$ provide the necessary conditions for photoconductive radiation (illustrated as blue semicircles). Details on photoconductive radiation are provided in Section 3.8.1. Although the dipoles are only spaced apart by 1.1 mm thick insulating alumina, the radiation arriving at the detector dipole is already in the far field. With the help of the second incident pulse $I(t+\tau)$, the arriving radiation is detected as a voltage signal V_s. After Auston *et al.* (1984a). (b) The photoconducting dipole antenna is a modification of the photoconducting Hertzian dipole. The antenna shown can function as either an emitter or detector. Terahertz emission and detection were successfully conducted with 2 antennas spaced 2 mm apart in free-space (stripline-sides facing each other). After Smith *et al.* (1988).

As shown in Fig. 3.10(a), the picosecond photoconducting Hertzian dipole design uses two identical photoconducting dipoles mounted symmetrically on either side of a thin slab of high resistivity alumina, therefore removing the need for transmission lines. The THz field emitted from one of the dipoles transmits through the alumina, and is detected by the other dipole. The principle behind the emission of THz from the dipole is similar to that of the Auston switch, and the detection process is similar but in reverse. The time response of this system is 1.6 ps (Auston *et al.* 1984a); when InP:Fe is used instead of alumina, the response time is 1 ps (Karin *et al.* 1986). Subpicosecond time response was subsequently achieved using a novel photoconducting dipole antenna design as shown in Fig. 3.10(b) at a detection distance of 2 mm (Smith *et al.* 1988). All the photoconducting Hertzian dipole designs mentioned thus far extend existing radio/microwave antenna techniques into the terahertz regime.

In order to increase the detection distance, the photoconducting Hertzian dipole technique was utilised differently by Fattinger and Grischkowsky whereby "optical techniques are adapted into the terahertz regime" (Fattinger and Grischkowsky 1988). The Hertzian dipole used is a point dipole source that is dimensionally smaller than any of the radiated wavelengths. This point source is located at the focal point of a spherical sapphire lens, as shown by the zoomed top view of the emitter in Fig. 3.11. Diffraction limited THz radiation generated at the point source can either be focused by the spherical lens onto the detector, or collimated by the spherical lens into free-space, therefore the detection distance is far superior to that of other Hertzian dipole designs described previously. Comparing Figs. 3.1(b) and 3.11, it is evident that many PCA systems today utilise point source THz optics. The principle behind point source THz optics will be introduced in the next Subsection.

3.8.1 Principle of Photoconductivity: THz Generation Using PCAs

The point source method relies on THz emission on coplanar transmission lines—a photoconductive semiconductor technique first demonstrated in 1986 by Ketchen *et al.* The Auston switch[33] introduced in Section 3.5.1 utilises photoconductive switching to achieve photodetection. This section describes the photoconductive process based on reports by other authors (Jepsen and Keiding 1995, Jepsen *et al.* 1996, Cheville 2008).

[33]Mathematical theory related specifically to the Auston switch can be found in Johnson and Auston (1975).

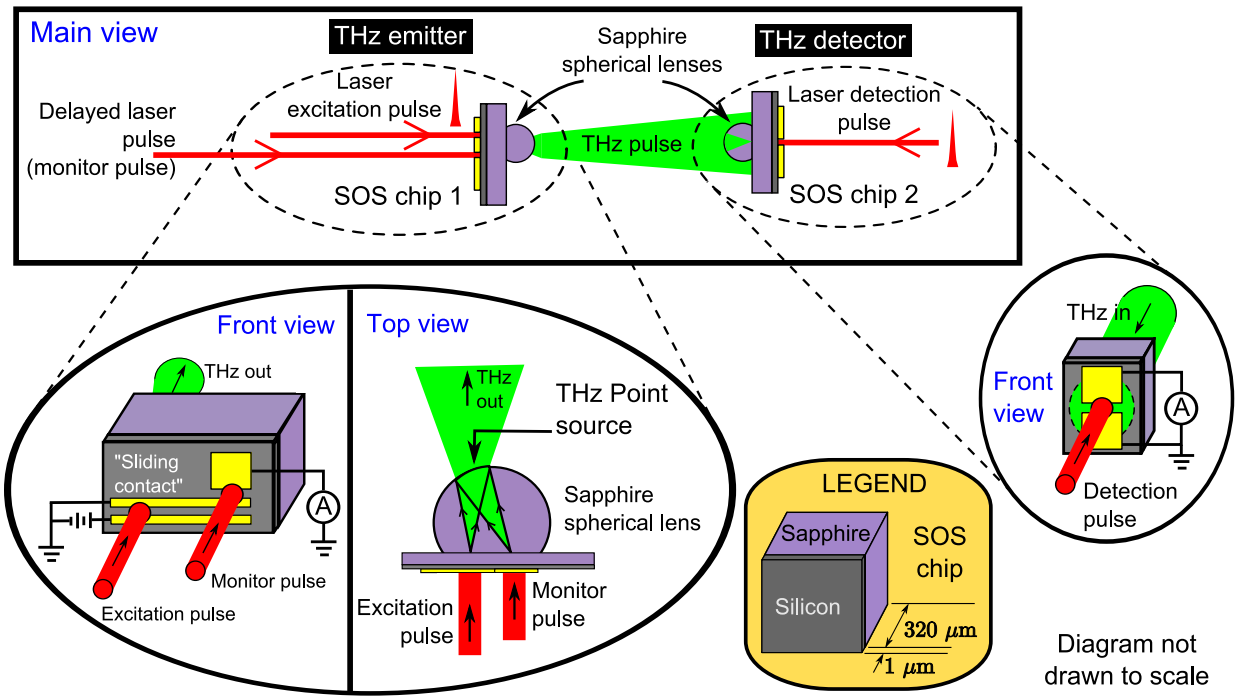

Figure 3.11: First long-range PCA system. The first PCA system capable of detecting pulsed THz radiation emitted 1 m away. This system uses point source THz optics that involve silicon-on-sapphire (SOS) chips and sapphire spherical lenses. Note that the thickness of the SOS chip is grossly exaggerated in the main diagram. The size ratio of the SOS chip and spherical lens is more accurate in the zoomed top view. The emitter consists of a pair of aluminium coplanar transmission lines mounted on undoped SOS wafer. Fast electric transients are generated at the location of the excitation pulse, resulting in THz emission on the sapphire side of the chip. The delayed laser pulse at the emitter provides a means for measuring the emitted THz signal. On the underside of the emitter, the sapphire spherical lens with diameter of 9.5 mm performs one of two actions depending on the distance between the emitter and detector: it either focuses the emitted THz radiation onto the spherical lens at the detector, or it partially collimates the emitted THz radiation into free-space (which arrives at the detector as shown by the dotted circle on zoomed front view). The detector uses the reverse point source effect to focus the THz radiation onto a simple photoconductive gap on SOS. Diagram is not to scale. After Fattinger and Grischkowsky (1988) and Fattinger and Grischkowsky (1989b).

As shown in Fig. 3.12(a), a pair of transmission lines are mounted on a semiconductor material with high photocarrier mobility, high photocarrier recombination time, and with bandgap energy less than the photon energy of an optical laser pulse. The third condition is necessary so that electron-hole pairs form easily when the laser pulse is

incident on the semiconductor; the reasons for the first and second conditions will be apparent shortly.

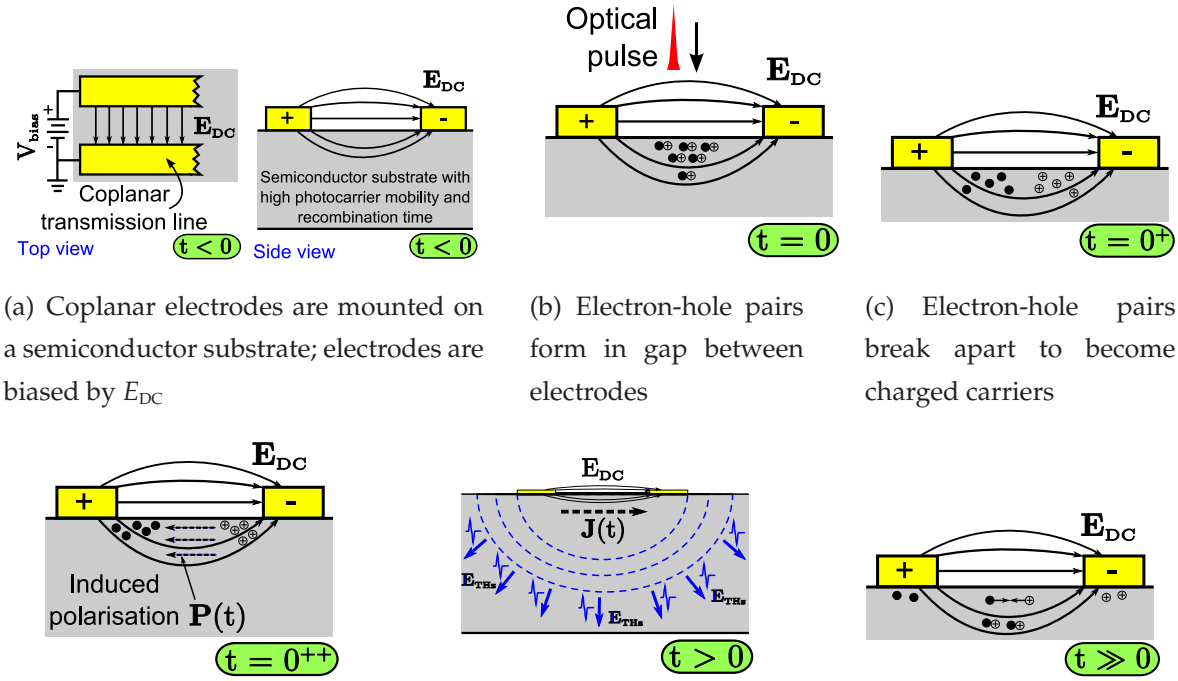

(a) Coplanar electrodes are mounted on a semiconductor substrate; electrodes are biased by E_{DC}

(b) Electron-hole pairs form in gap between electrodes

(c) Electron-hole pairs break apart to become charged carriers

(d) Gap behaves as a dipole antenna with polarisation $\mathbf{P}(t)$

(e) Short burst of $\mathbf{E}_{THz}$ is emitted from the dipole antenna

(f) Charged carriers reverse direction and recombine

Figure 3.12: Photoconductivity in PCAs. (a) Aluminium coplanar transmission lines (yellow/-lighter region) are mounted using conventional photolithographic lift-off techniques on a semiconductor substrate (grey/darker region) with high carrier mobility (e.g. silicon-on-sapphire or SOS). Each transmission line is 5 μm wide, and the gap between them is 10 μm wide. The transmission lines behave like electrodes of a capacitor when a strong electric field E_{DC} is applied across them. (b) An incident optical pulse causes the formation of electron-hole pairs at depth Δx_1 in the gap between the electrodes (solid black circle $\bullet$ = electron, open circle $\oplus$ = hole). (c) E_{DC} causes the electron-hole pairs to break apart and migrate towards the respective electrodes. The gap now becomes a very short conductive channel. (d) A transient current flows in the conductive channel, causing the channel to behave as a dipole antenna. (e) The rate of flow of the transient current gives rise to the emission of THz radiation $\mathbf{E}_{THz}$ from the dipole antenna. $\mathbf{E}_{THz}$ has a spherical wavefront and lasts several picoseconds or less. (f) Without any external excitation to sustain the charged carriers at the high energy level needed to keep them separate as positive and negative charges, they recombine as electron-hole pairs. After Ketchen *et al.* (1986) and Cheville (2008).

The coplanar transmission lines are DC biased at a very high voltage so that a strong electric field E_{DC} ($\approx 10^6$ V/m) exists across the narrow gap between the lines. Note that E_{DC} is close to the breakdown voltage threshold for air, therefore the entire structure behaves like a fully-charged capacitor of several picofarads. The coplanar transmission lines act like electrodes and will be referred to as *electrodes* henceforth.

The incident optical pulse with photon energy greater than the semiconductor's bandgap energy is purposely directed between the electrodes because:

1. As shown in Fig. 3.12(b), the semiconductor absorbs photons from the optical pulse and generates electron-hole pairs (non-instantaneously) between the electrodes at depth Δx_1, which is approximately equal to the semiconductor's absorption depth. The electron-hole pairs create an electrically neutral plasma that decreases the conductivity $\sigma(t)$ of the semiconductor at depth Δx_1. In other words, the electrically neutral plasma increases resistance of the semiconductor at depth Δx_1.

2. As shown in Fig. 3.12(c), E_{DC} causes the electron-hole pairs to break apart and become individual charged carriers (also known as photocarriers). These carriers accelerate towards the respective electrodes: negative carriers (electrons) towards the positive electrode, positive carriers (holes) towards the negative electrode. The resistance of the semiconductor at depth Δx_1 therefore decreases.

3. The movement of charged carriers between the electrodes constitutes a flow of current $i(t)$ with current density vector $\mathbf{J}(t)$. If the semiconductor has high carrier mobility, then the velocity $v(t)$ of the moving carriers is high, and results in a large $\mathbf{J}(t)$ value because $\mathbf{J}(t)$ increases proportionally to $v(t)$. This means the current flow between the electrodes is rapid, hence the current is called *transient current*. The duration of the transient current is around one picosecond. Note that although $\mathbf{J}(t)$ is large, it is as short-lived as the transient current.

4. The physical location in the semiconductor where the charged carriers separate now behaves as an electric dipole antenna (hence the name photoconductive antenna). The length of the electric dipole antenna is equal to or smaller than the gap between the electrodes (10 μm). This electric dipole antenna induces a time-varying electric polarisation $\mathbf{P}(t)$ as shown in Fig. 3.12(d). The direction of $\mathbf{P}(t)$ opposes that of the static field $\mathbf{E}_{DC}$.

The explanation of photoconductivity above is applicable to all photoconductive processes, including the Auston switch. Note that a second conductive region at depth Δx_2 is induced in the Auston switch by the second optical pulse with wavelength of 1.06 μm. The remaining explanation below pertaining to THz radiation is however not applicable to the Auston switch because it contains a ground plane (Fig. 3.6), which prevents electromagnetic radiation out of the semiconductor substrate.

The electric polarisation $\mathbf{P}(t)$ is defined as the resultant dipole moment $\mathbf{p}(t)$ per unit volume, so $\mathbf{p}(t)$ will be used instead of $\mathbf{P}(t)$ henceforth. The first derivative of $\mathbf{p}(t)$ is equal to the product of the length of the electric dipole antenna (10 μm as mentioned in item 4 above) and the time-varying transient current $i(t)$ flowing between the electrodes. The second derivative of $p(t)$ is equal to the acceleration of $i(t)$. The importance of the second derivative of $p(t)$ becomes apparent from the far-field relationship between $\mathbf{E}_{\text{THz}}$ and $p(t)$ for a Hertzian dipole:

$$\mathbf{E}_{\text{THz}}(r,t) \propto \frac{n^2}{r}\frac{dp^2(t)}{dt^2} = \frac{n^2}{r}\frac{di(t)}{dt}, \tag{3.13}$$

where r is the radial distance from the electric dipole, n is the refractive index of the semiconductor material, and the angle of $\mathbf{E}_{\text{THz}}(r,t)$ is normal to the axis of the electric dipole (Auston *et al.* 1984a, Smith *et al.* 1988). The temporal profile of $\mathbf{E}_{\text{THz}}(r,t)$ is therefore described by Equation (3.13): when the charged carriers accelerate rapidly towards the electrodes (Fig. 3.12(c)), the time domain profile of the current is a rapidly rising exponential with time constant t_{rise}. The second derivative of $p(t)$, which is the first derivative of $i(t)$ as shown in Equation (3.13), will be a positive peak with amplitude proportional to t_{rise}. When the charged carriers reverse their direction and rejoin as electron-hole pairs (Fig. 3.12(f)), the time domain profile of the current is a decaying exponential with time constant t_{fall}. The second derivative of $p(t)$ will be a negative peak with amplitude proportional to t_{fall}. The emitted THz signal therefore has a well-defined bipolar temporal pulse shape. Note that $\mathbf{E}_{\text{THz}}(r,t)$ has a spherical wavefront that radiates out from the electric dipole antenna (Jackson 1975). The cross-sectional view of the wavefronts of $\mathbf{E}_{\text{THz}}(r,t)$ is depicted by the dashed radial lines in Fig. 3.12(e).

The transient current duration (i.e. the carrier mobility (lifetime) in the semiconductor material) is related to the carrier velocity $v(t)$. The time scale involved from the moment of optical excitation (Fig. 3.12(b)) to THz generation (Fig. 3.12(e)) is of several picoseconds or less.

When the charged carriers complete their migration to the respective electrodes, they begin moving in the opposite direction to rejoin as electron-hole pairs (Fig. 3.12(f)) because there is insufficient excitation to sustain them at the bandgap energy level needed to stay as segregated positive and negative charges; the charged carriers are more stable in the electron-hole configuration. The transient current therefore decays and the resistance of the semiconductor at depth Δx_1 increases. The velocity at which the charged carriers travel towards each other depends on the semiconductor's photo-carrier recombination time; the recombination time can take several hundred picoseconds, which is significantly longer than the time taken for the carriers to separate.

In order to reduce the recombination time so that a narrower THz pulse width is achieved (and also so that faster photoconductive switching is possible in switching applications), artificial *ion traps* can be introduced into the semiconductor material to encourage electron-hole recombination. These traps are implanted via radiation damage (Section 3.8.3).

The THz generation process is complete when the re-formed electron-hole pairs achieve electrical neutrality (Fig. 3.12(a)), which can be interpreted as the electric field wavefronts closing on themselves.

The principle of photoconductivity also applies to PCA-based THz detection, which will be introduced in the next Subsection.

3.8.2 Photoconductive THz Detection

The photoconductive THz generation process described in Section 3.8.1 can easily be reversed to allow photoconductive THz detection. The autocorrelation technique that was mentioned at the end of Section 3.5.1 will be elaborated on here.

The detector PCA has a similar construction to that of the emitter PCA, such as that shown in Fig. 3.12(a). Both the emitter and detector receive the incoming optical pulses at the gap between the electrodes—the reason for this is as explained in Section 3.8.1. Referring also to Fig. 3.1(b), the optical pulses incident on the detector are time-shifted from those incident on the emitter. Note that the emitter PCA requires a continuous external DC bias source V_{DC} and that THz radiation is emitted from the underside of the antenna.

In the detection process, it is the THz signal $\mathbf{E}_{\text{THz}}(t)$ that provides the bias to the PCA. Since detection process is the reverse of emission, $\mathbf{E}_{\text{THz}}(t)$ enters the antenna from its

underside (instead of exiting for the emission case). Since $\mathbf{E}_{\text{THz}}(t)$ is not present all the time, and the detector has no *a priori* knowledge of its arrival, the detector needs to be continuously prepared for its arrival by priming the gap between the electrodes. In the absence of an external DC bias, the incoming optical pulse still creates the electrically neutral plasma in the gap as shown in Fig. 3.12(b), but electron-hole pairs do not separate due to the absence of the external static electric field E_{DC}. The formation of the plasma increases the resistance of the gap. Since the interval between the optical pulses is typically 3 orders of magnitude longer than the formation time of the plasma (nanoseconds versus picoseconds), the electron-hole pairs dissipate and the resistance of the gap returns back to its initial level.

In the absence of $\mathbf{E}_{\text{THz}}(t)$, no net external current flows in the gap during the formation and dissipation of the plasma. The maximum resistance of the gap is determined by the gap's dimensions (Cheville 2008). When $\mathbf{E}_{\text{THz}}(t)$ enters the underside of the antenna and arrives at the gap, it provides a DC voltage bias across the electrodes; this voltage is approximately equal to the magnitude of $\mathbf{E}_{\text{THz}}(t)$ multiplied by the gap distance. From Ohm's law, a current $I(t)$ now flows between the electrodes and can be detected by a microampmeter or high-sensitivity current amplifier.

The detection process described thus far does not take into account the mismatch in the pulsewidths of $\mathbf{E}_{\text{THz}}(t)$ (several hundred picoseconds) and the optical pulse (tens of femtoseconds). In fact the extremely short optical pulse appears like a unit impulse function $\delta_{\text{opt}}(t)$ when compared to $\mathbf{E}_{\text{THz}}(t)$. It is not possible to capture the whole $\mathbf{E}_{\text{THz}}(t)$ signal using the simple detection described in the previous paragraph unless $\mathbf{E}_{\text{THz}}(t)$ is *sifted* by time-shifting $\delta_{\text{opt}}(t)$. In other words, $\mathbf{E}_{\text{THz}}(t)$ needs to be convolved with $\delta_{\text{opt}}(t)$:

$$I(t) \propto \int_{-\infty}^{+\infty} E_{\text{THz}}(\tau)\,\delta_{\text{opt}}(\tau + t)\,d\tau, \tag{3.14}$$

$$\propto \int_{-\infty}^{+\infty} E_{\text{THz}}(\tau + t)\,\delta_{\text{opt}}(\tau)\,d\tau. \tag{3.15}$$

The implications of Equations (3.14) and (3.15) are (i) that either $\mathbf{E}_{\text{THz}}(t)$ or the optical pulses $\delta_{\text{opt}}(t)$ can be delayed by the delay stage (Fig. 3.1(b)), hence the delay stage can be included in the probe path instead of the pump path; (ii) the sifting process effectively samples the whole $\mathbf{E}_{\text{THz}}(t)$, therefore the PCA detector acts as a sampling gate (Auston *et al.* 1980a, Smith *et al.* 1981) and is sometimes referred to as PCA sampling (analogous to EO sampling introduced in Section 3.5.2).

The introduction to photoconductive THz generation and detection concludes here, however two more topics salient to PCA THz systems will be briefly described in the following Subsection.

3.8.3 New Dipole Antenna Materials and Designs

The basic coplanar transmission line design presented in Figs. 3.11 and 3.12(a) is still used today—its longevity probably owing to its simple design. Nonetheless, research into new THz PCA designs has been active, with the main goal of increasing the emitted THz bandwidth as well as improving PCA-based THz detection. Techniques for improving PCA design involve either new semiconductor materials with shorter carrier lifetimes (higher carrier mobility), or new electrode designs, or both. Novel designs that add functionality to the antenna have also been explored (e.g. biochip for liquid analysis).

Early improvement to PCAs focused on improving the photoconductive switching time by finding alternatives to materials already in use, namely silicon and radiation damaged silicon-on-sapphire (SOS).

Radiation damage of a semiconductor film involves the use of a Van der Graff accelerator to implant ions (also known as ion traps) into the film. For silicon-on-sapphire (SOS), varying doses (3×10^{11} to 3×10^{15} ions per cm^{-2}) of 0.4 MeV $_{16}O^{+}$ ions are implanted at room temperature. The ion beam is incident at 60° to the surface normal of the film, and the ions are implanted up to 0.5 μm under the surface. A wide range of defect densities is achieved by varying the dose of implantation (Smith *et al.* 1981).

Radiation damaged semiconductors have been reported to be unstable at room temperature, and the advantageous effects of the damage anneals away within days or weeks (Smith *et al.* 1989). However, this claim has not been supported by subsequent publications.

Gallium arsenide (GaAs) was one of the first alternatives to silicon and radiation damaged SOS (Lee *et al.* 1977, Lee 1977, Kolner and Bloom 1986, Smith *et al.* 1989), followed by indium phosphide (InP) (Foyt *et al.* 1982, Downey and Schwartz 1984, Wiesenfeld *et al.* 1987). Superconductive materials such as niobium (Nb) (Gallagher *et al.* 1987), indium (In) transmission lines (Hsiang *et al.* 1987), and $YBa_2Cu_3O_{7-\delta}$ (YBCO) (Hangyo *et al.* 1996) were also explored. Undamaged SOS significantly reduced the full width at

half maximum (FWHM) transient current lifetime from several picoseconds to a few hundred femtoseconds (Krökel *et al.* 1989).

The photoconductive switching process is ultimately limited by the charged carriers' lifetime in the material; however, optimising the dipole antenna design can result in improvements to photoconductivity. The H-structure as shown in Fig. 3.13(a), which reduces the gap between the electrodes in the antenna, was the first improvement to the coplanar transmission line structure. Since current density is inversely proportional to the area of the gap, the reduced gap in the H-structure results in more radiated power and therefore increased bandwidth (van Exter *et al.* 1989a, van Exter and Grischkowsky 1990). By using a coplanar emitter and a H-structure detector, the benefits of both structures are combined to yield a much wider bandwidth beyond 3 THz (Katzenellenbogen and Grischkowsky 1991). An improvement to the H-structure is the bow-tie structure as shown in Fig. 3.13(b), which further reduces the gap distance to achieve enhanced bandwidth (Tonouchi *et al.* 1997, Seliuta *et al.* 2006, Ishihara *et al.* 2006).

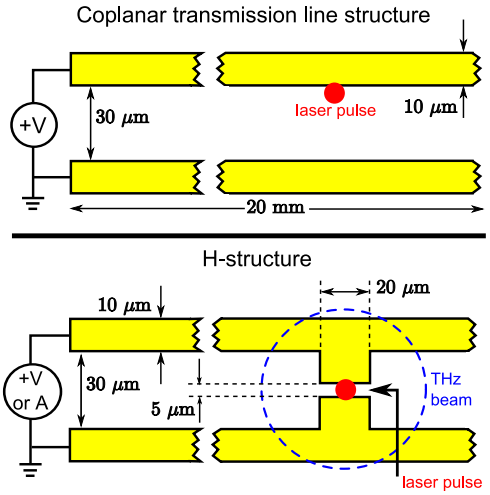

(a) (Top) coplanar transmission line PCA; (Bottom) PCA with H-structure

(b) PCA with bow-tie structure

Figure 3.13: Improvements to PCA designs. (a) The H-structure reduces the gap between the electrodes to 5 μm, resulting in more radiated power and improved detected bandwidth. After van Exter *et al.* (1989a). (b) The bow-tie structure can further reduce the gap to 2 μm. After T-Ray Science (2008a) and after Kašalynas *et al.* (2009).

Other antenna designs that have been explored include large aperture dipole antenna for steerability (Hu *et al.* 1990a), large aperture diodes (Xu *et al.* 1991), log spiral

and log periodic (Dykaar *et al.* 1991), all electronic systems using monolithic nonlinear transmission lines (NLTL) (Bostak *et al.* 1994), bow-tie NLTL structures (van der Weide 1994), amplified systems (Greene *et al.* 1991), and probes on the semiconductor structure (Pfeifer *et al.* 1994). 'Hand-built' devices such as that shown in Fig. 3.14 may look crude and have a wide gap distance, but can still operate successfully especially as a THz emitter.

(a) Underside of a 'hand-built' bow-tie PCA

(b) Front side of the same PCA

Figure 3.14: Novel PCA construction. (a) This bow-tie PCA is made by applying silver paint on a thin film of GaAs that is attached onto the back of a silicon lens. Since the paint is manually applied, the gap size is large compared to PCAs made by photolithographic processes, but this PCA still functions well as a THz emitter. (b) The front view of the same PCA shows the silicon lens connected to electrodes for DC biasing at over 400 V. Equipment courtesy of R. E. Miles at the University of Leeds.

The different antenna structures and materials described above emit different THz radiation patterns in the far-field, and result in different system signal-to-noise ratios being reported (Lutz and DeFonzo 1989, Darrow *et al.* 1990, Zhang *et al.* 1990a, Jepsen and Keiding 1995, Jepsen *et al.* 1996).

3.9 Electro-optic (EO) THz Generation

The success of EO Čerenkov sampling presented in Section 3.6 triggered renewed interest in the 1960s and 1970s work on the generation of FIR radiation in crystals (Section 3.5). This interest, coupled with the lessons learnt from EO Čerenkov sampling, helped Zhang *et al.* (1990b) to demonstrate pulsed THz radiation in free-space using semiconductor surfaces illuminated by femtosecond laser pulses. This technique differed from EO Čerenkov sampling in that only one beam of laser pulse was required,

and this beam did not need to be tightly focused. By 1992, Xu *et al.* (1992) were able to demonstrate THz generation from bulk EO materials (Xu *et al.* 1992). Pulsed THz radiation emitted from a bulk semiconductor material is commonly referred to as EO free-space THz generation, or simply EO THz generation.

The physics behind EO THz generation has many similarities with that of PCA THz generation (Section 3.8.1). Referring to Fig. 3.12(b), a bare (without electrodes) noncentrosymmetrical nonlinear crystal that is illuminated by a femtosecond laser pulse will also form electron-hole pairs. As highlighted in Section 3.4.2, although the external static field $\mathbf{E}_{DC}$ is absent, the ultrafast laser pulses incident on the noncentrosymmetrical crystal create high voltage electrical transients analogous to $\mathbf{E}_{DC}$ in amplitude. The crystal[34] now behaves like a Hertzian dipole.

As with the PCA case shown in Fig. 3.12(c), the electrical transients cause the electron-hole pairs to break apart and accelerate—the electrons move towards the surface of the crystal (the surface illuminated by the laser pulse), while the holes move away from the surface and head deeper into the crystal. Recalling that for the PCA case as shown in Fig. 3.12(d), the movement of charged carriers between the electrodes results in the flow of transient current, and that the gap between the electrodes becomes a dipole antenna with length equal to the gap length. For the EO case, current flows across the depletion depth l_1; this depth acts as the dipole antenna with an electric polarisation, which results in the emission of THz radiation which either exits the crystal from its underside (Figs. 3.12(e) and 3.15(a)), or exits from the front side of the crystal, i.e. same side as the incident laser pulse (Fig. 3.15(b)). Note that as shown in Fig. 3.15(a), some amount of laser light also exits the crystal and travels with the THz radiation. The intensity of this laser light is less than the incident laser pulse, but can be sufficient to damage sensitive samples under investigation and can also interfere with the EO THz detector. A filter[35] is sometimes placed after the crystal to block the residual laser light.

One significant benefit of EO THz generation is that it provides a platform for studying optical rectification (Section 3.3.1) in semiconductor and non-semiconductor EO materials using coherent measurements (Zhang *et al.* 1992a), for the purpose of discovering new submillimeter and THz radiation sources. For example, the nonlinear organic crystal dimethyl amino 4-N-methylstilbazolium tosylate (DAST) has shown to be a

[34] The physical orientation of the nonlinear crystal is an important consideration in both EO THz generation and detection. A brief introduction to nonlinear crystal geometry with respect to THz generation is given in Appendix B.

[35] A simple filter can be made from black polyethylene, such as that used in garbage bags.

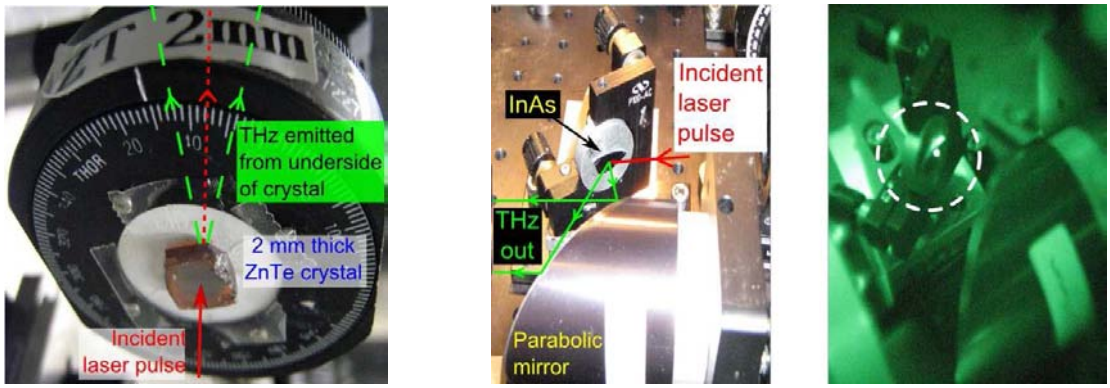

(a) ZnTe crystal as an EO THz generator (b) InAs as an EO THz generator

Figure 3.15: Examples of crystals used in EO THz generation. (a) Zinc telluride (ZnTe) is a commonly used crystal for EO THz generation and detection. The thickness of the ZnTe generator is typically between 1 to 2 mm, whereas the ZnTe detector is less than 1 mm. Terahertz radiation is emitted from the underside of the crystal. Crystal courtesy of X.-C. Zhang at RPI. (b) (Left) Terahertz radiation can also be emitted from the same side as the incident laser pulse. Crystals used in such a scenario are usually opaque to either THz or optical light, except for the thin conduction layer on the surface of the crystal. Indium arsenide (InAs) is used in this example. (Right) View from an infrared camera of the InAs crystal. The bright spot inside the dotted circle corresponds to the laser pulse incident at an angle. Crystal courtesy of I. Wilke at RPI.

good source of submillimeter waves (Zhang *et al.* 1992b). Another notable benefit of EO THz generation is that THz systems can be purely EO-based (Wu and Zhang 1995), thus providing a complete alternative to PCA THz systems. Electro-optic detection will be presented in the next Section.

In conclusion, like the Auston switch (Section 3.5.1) and EO sampling (Section 3.5.2), EO THz generation is another milestone in THz history.

3.10 Electro-optic (EO) THz Detection

Comparing the detection and post-detection end of Fig. 3.1(a) with the components used in Fig. 3.7, it is obvious that EO THz detection is heavily based on EO sampling, which was presented in Section 3.5.2. Electro-optic sampling has thus far been described simply as a technique that utilises a Pockels cell to detect the lifetime of electrical transients. The detection process alters the birefringence of the Pockels cell, which

results in asymmetry in the polarisation of the outgoing optical signal. Balanced photodiodes interpret the asymmetry as a differential current. The delay stage utilised in EO sampling serves the same sifting purpose as in the PCA case, where the pump and probe signals are convolved as described in Equations (3.14) and (3.15) because of the grossly different pulsewidths of the two signals.

In PCA detection, the strength of the THz electric field is translated as a current that flows in the electrodes. In EO THz detection where there are no electrodes on the detector, the EO detection process relies on the Pockels effect (Section 3.4) in the nonlinear crystal to detect the incident THz electric field. The resulting birefringence is captured by polarised *pulses* of light travelling through the crystal—these light pulses are provided by the probe beam.

The EO crystal used as a detector is usually selected to be thinner than the EO emitter because there is generally a group velocity mismatch (GVM) between the THz radiation and the laser pulses in the probe beam (Wu and Zhang 1996a). The mismatch has been measured as being 0.4 ps/mm in ZnTe, at least 15 ps/mm in GaAs, and at least 14 ps/mm in $LiNbO_3$ (Wu *et al.* 1996, Wu and Zhang 1996b). The effect of this mismatch is reduced in a thin detector crystal, resulting in an increase in the measurement bandwidth. Systems utilising EO detectors have reported bandwidths exceeding 7 THz (Wu and Zhang 1997, Han and Zhang 1998).

As an aside, noncentrosymmetrical nonlinear crystals that are commonly used as the EO detector are zinc telluride (ZnTe) and lithium niobate ($LiNbO_3$). The reason for this choice of crystal is explained in Appendix B.

The following Subsections will only elucidate the purpose of the hardware used before and after the EO detector.

3.10.1 Aligning THz and Laser Pulses

Unlike PCA detection, the incident THz and probe signals can be aligned to enter the EO detector from the same side (the signals typically enter from opposite sides in PCA detection). The alignment of the two signals in EO detection is achieved using a beamsplitter as shown in Fig. 3.16(a). The beamsplitter is transparent to both the THz radiation, and the laser light in the probe beam. Examples of a suitable beamsplitter for this purpose are a pellicle beamsplitter, or indium tin oxide (ITO) as shown in Fig. 3.16(b).

The beamsplitter is chosen to have minimal dispersion and aberration so as not to introduce extraneous polarisation artifacts that may incorrectly be interpreted as THz radiation.

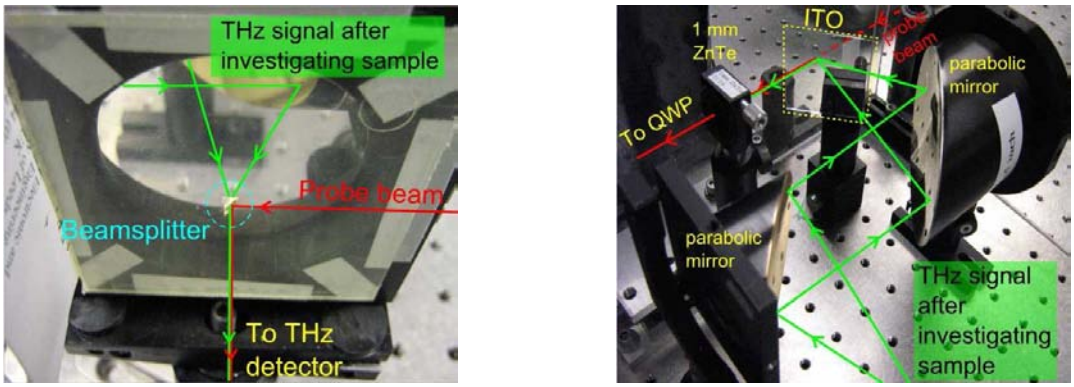

(a) Beamsplitter used to align the THz and probe beams (b) ITO used as a beamsplitter

Figure 3.16: Alignment of THz and laser pulses for EO THz detection. (a) The beamsplitter aligns the incident THz and optical probe beam prior to their arrival at the EO THz detector. Equipment courtesy of R. E. Miles at the University of Leeds. (b) An alternative to a beamsplitter is a sheet of ITO or any material with similar optical properties. Equipment courtesy of X.-C. Zhang at RPI.

3.10.2 Terahertz-Induced Polarisation Change

The optical signal emitted from the EO detector has an electric field with phase shift dependent on the presence of the THz field: zero phase shift in the absence of THz results in linear polarisation; non-zero phase shift in the presence of THz gives slight elliptical polarisation.

The presence of two differing types of polarisation—linear and elliptical—complicates detection due to the need for a polarimetric-type detector. However, if the linear polarisation can be converted into circular polarisation, then the original elliptical signal and the newly circularly polarised signal can be compared based on their common polarising components, i.e. their orthogonal vectors, which can be detected by simpler non-polarimetric techniques that will be elaborated on in Sections 3.10.4 and 3.10.5.

3.10.3 Circular Polarisation of a Signal

A quarter wave-plate (QWP) is a type of retardation polariser that is used to circularly polarise only a linearly polarised optical signal emitted by the THz detector; the polarisation of an elliptically polarised optical signal is unaffected by the QWP.

The signal exiting the QWP now has one of two possible polarisations: elliptical or circular. These two types of polarisations share a common characteristic, *viz* that either polarisation can be decomposed into its two orthogonal polarisation components. Using the same notation as in Section 3.4, and assuming that the z axis is the direction of propagation, the polarisation components are: p (or x), and s (or y). The descriptions p and s will be continued henceforth because they are more commonly used than x and y.

The amplitude of the p and s components will be proportional to the presence as well as the strength of the THz signal. For example, the p and s amplitudes are equal in the absence of a THz signal because only the circularly polarised signal will be present. When a THz signal is present, only the elliptically polarised signal will be present, producing differing p and s amplitudes. This difference between the amplitudes now provides a means of measuring the strength of the THz signal. However the p and s components must first be extracted. This is achieved in the Wollaston prism.

3.10.4 Wollaston Prism (WP)

As illustrated in Figs. 3.17(a) and 3.17(b), a Wollaston prism (WP) is a type of polarising beam splitter that is made from a material (usually calcite) that is birefringent, i.e. the material has two orientation-dependent refractive indices. As described in Section 3.4, the orthogonal p and s components from an incident single wavefront travel at different velocities inside the WP due to the orientation-dependent refractive indices, resulting in the p and s components exiting the Wollaston prism at different velocities and angles (typically between 15-45° for laser light at a centre frequency of 780-800 nm). Two wavefronts, the o and e-rays, now exist whereby each wavefront can be manipulated independently.

When either the elliptical or the circularly polarised wavefront from the QWP is incident on a Wollaston prism, the o and e linearly polarised wavefronts exit the Wollaston prism as two separate optical wavefronts (beams), diverging in a V-shape. The

NOTE:
These figures are included on page 92 of the print copy of the thesis held in the University of Adelaide Library.

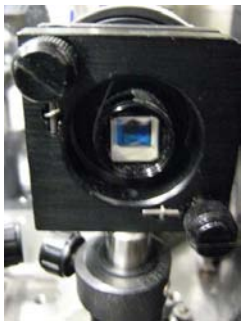

(a) (Top) Incident wavefront split by a WP; (Bottom) commercial Wollaston prisms

(b) Birefringence in a crystal

(c) WP mounted on a stand

Figure 3.17: Wollaston prism (WP). (a) (Top) This picture illustrates the splitting of the single incident wavefront inside the WP into two orthogonal wavefronts: *o* and *e*. After Wikipedia (2008b); (Bottom) Examples of commercially available Wollaston prisms encased in cylindrical aluminium housing. After Melles Griot (2007a). (b) This picture shows a Glan-Taylor prism (which is similar to a WP except that the emitted *o* and *e* beams are always orthogonal); also shown are (i) a graph of the two orientation-dependent refractive indices inside a birefringent medium, which results in (ii) the emission of two wavefronts that are evident by the double-image of the printed text under the prism. After Melles Griot (2007b). (c) A WP (with its aluminium housing) mounted on a stand for use in a THz system. WP courtesy of X.-C. Zhang at RPI.

strength of the THz signal is determined by the difference in amplitude (intensity) between these two beams; the intensity of each beam can be measured individually by any detector sensitive to linearly polarised radiation, such as photodetectors.

In the absence of any THz signal, the difference in intensities between the *o* and *e* beams is ideally zero because the *p* and *s* components of the circularly polarised signal are equal. Conversely, the presence of a THz signal results in a significant difference in intensity between the *o* and *e* beams due to the unequal *p* and *s* components of the elliptically polarised signal.

3.10.5 Balanced Photodetectors and Lock-In Amplifier (LIA)

Balanced photodetectors are ideal for detecting the intensities of the *o* and *e* beams because their circuit generates a zero current signal when the *o* and *e* beam intensities are equal. The photodetectors are thus balanced in the absence of any THz signal to give a zero differential current.

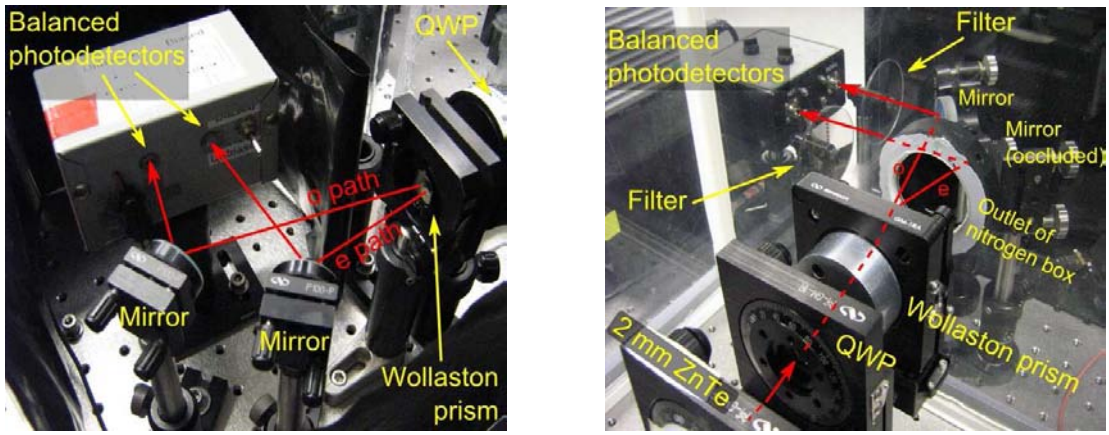

(a) Last stage of the THz detection setup

(b) Last stage of the THz detection setup used at the University of Leeds

Figure 3.18: Photodetectors. (a) The illustration on this photograph shows the *o* and *e* beams emitted from the Wollaston prism and directed via mirrors to the balanced photodetectors. Equipment courtesy of X.-C. Zhang at RPI. (b) Similar THz detection setup but with additional optical filters before the balanced photodetectors for attenuating the incoming *o* and *e* beams' power. Equipment courtesy of R. E. Miles at the University of Leeds.

The differential current is very small, typically in the microamp range. Furthermore, the differential current has been modulated by the chopper as described in Section 3.7.2, hence can be demodulated back to the baseband frequency using a lock-in amplifier (LIA). This form of demodulation is called *phase sensitive detection*.

The differential current from the balanced photodetectors is fed into the differential input of the LIA, while the chopper frequency provides the reference input. The LIA can be thought of as a multiplier circuit: it contains an amplifier to amplify the incoming differential current, and then a multiplier to multiply the reference signal with the amplified differential signal. The resulting signal is then low pass filtered so that any noise is averaged or smoothed. More details on LIAs can be found from manufacturer datasheets, such as Bentham Instruments Ltd. (2008).

3.11 Variants of Pulsed THz-TDS Systems

As a final note, two variants of pulsed THz-TDS systems are mentioned briefly. Waveguided THz systems operate using the same principles as microwave waveguides,

channelling THz radiation either inside the confines or on the surface of 3D structures, such as ribbons, plates or fibres (Mendis and Grischkowsky 2000, Mendis and Grischkowsky 2001, Mendis *et al.* 2005b, Mendis 2006a, Mendis 2006b, Mendis 2007). The generation and detection of THz radiation is no different from that described in EO/PCA THz systems, however it is necessary to focus the THz beam in and out of the waveguide.

High power systems that utilise ancillary optical devices, such as prisms, together with standard THz emitters are able to generate THz radiation that are one order or more stronger than without the ancillary optical devices (Carr *et al.* 2002, Johnston *et al.* 2002, Mendis *et al.* 2005a).

These variants of pulsed THz-TDS systems create new exciting possibilities for THz spectroscopy. The confined space of THz waveguides make them attractive for examining small quantities of sample, such as biological fluid. An example of a microfluidic device for THz spectroscopy will be discussed in Section 4.5.2.

3.12 Chapter Summary

The generation and detection of THz radiation in pulsed THz-TDS systems have been introduced in this Chapter. The underlying principles of optical rectification of crystals with second order nonlinearity, and transient photoconductivity have also been discussed in detail. The THz generation and detection techniques discussed in this Chapter underpins all the THz experiments presented from Chapter 5 onwards in this Thesis.

Prior to discussing the novel THz experiments and work included in this Thesis, one final review Chapter is necessary. Given the multidisciplinary nature of this Thesis, the next Chapter reviews medical spectroscopy and imaging research in the IR, microwave and THz frequency regimes. This Chapter is included because medically-inspired THz research is still in its infancy when compared to the medically-inspired IR and microwave research. There is much to be gained from reviewing past and present IR and microwave work because IR and microwave measurement techniques, as well as data, can often be adapted or expanded for use in the THz range. Parallel work in THz and IR/microwave fields will be highlighted in the next Chapter.

Chapter 4

Review of Medical Spectroscopy and Imaging

MEDICAL spectroscopic and imaging studies in both the non-terahertz and terahertz regimes are reviewed in this Chapter. Many frequencies in the electromagnetic spectrum have unique properties that are exploited accordingly through the plethora of diagnostic modalities and analytical tools available today. Information about chemicals and living organisms can be studied using frequencies across the electromagnetic spectrum, hence it is not uncommon to use several diagnostic modalities to access information at multiple frequencies. The infrared (IR) and microwave frequency regions, adjacent to THz frequencies on the electromagnetic spectrum, have been used in medical research to investigate many types of biological materials of interest to THz researchers. Measurement techniques and data accumulated in the IR and microwave frequency regions can often be adapted or expanded for use in the THz range, therefore it is useful to study work already carried out in these areas. This Chapter describes salient IR and microwave medically related research, and highlights parallel work in the THz field including the original contributions of this Thesis.

4.1 Medical Diagnostic Technologies

The use of radiation to profile or image biological matter is a common practice in medical diagnosis today. Medically useful electromagnetic frequencies span an incredible 16 orders of magnitude: from gamma rays (10^{19} Hz) to radio frequencies (several hundred kilohertz). This wide spectrum has allowed the development of a diverse range of imaging modalities: computed tomography (CT) utilises ionising X-rays ($\approx 10^{18}$ Hz); magnetic resonance imaging (MRI) relies on non-ionising electromagnetic fields in the radio frequency range ($\approx 10^{6}$ Hz); and positron emission tomography (PET) detects gamma rays emitted by a short-lived radioactive tracer (radiotracer) that is injected into a patient's blood stream. The advantage of this diversity in imaging modalities is that they can often be used in parallel to allow superimposition of images—a process called *image fusion*, or *co-registration* in medical terminology.

The infrared (IR) and microwave regions that sandwich the terahertz (THz) range have both been actively researched for medical purposes; however, the IR range is far more developed in terms of practical medical usage on live subjects because microwave tissue heating issues limit the extent of safe microwave exposure (Dimbylow 2002).

The techniques and results used in the IR and microwave regions are extremely useful for the THz range, particularly in the study of biotissue where THz data is scarce compared to well-documented IR and microwave tables of biotissue and water properties, which have been compiled over several decades.

This Chapter commences with a general discussion of spectral fingerprints. Medically related spectroscopic studies of biological matter performed in the IR and microwave regions is then introduced. Both IR and microwave spectroscopies are often used in conjunction as a means of understanding the overall interatomic behaviour of a molecule although experimental techniques in the two types of spectroscopies differ greatly. Fourier Transform Infrared (FTIR) is a common modality for IR spectroscopy, whereas a plethora of microwave techniques exist. Many of these techniques are suited, or can be suited to the THz range with some modifications. The Chapter concludes with biologically inspired THz spectroscopic studies, with emphasis on protein, water and biotissue.

4.2 What Causes Spectral Fingerprints?

In Sections 1.3 and 1.4, historical reviews of the discovery of infrared and microwave radiation and their evolution into modern day spectrometers were presented. The concept of the spectral fingerprints of chemical elements was introduced in Section 1.3.1, and it was shown that these spectral features form the basis of molecular and astronomical spectroscopy.

Both the IR and microwave frequency ranges are used in medical and biologically related spectroscopy. The basis of IR spectroscopy is the vibration and rotation of molecules, whereas microwave spectroscopy is usually only concerned with the rotation of polar molecules. Vibration refers to interatomic interactions that cause bonds between atoms to either stretch or bend in different directions from each other. Rotation refers to interatomic interactions that cause the bonds to rotate. In 1901, Max Planck proposed that the cause of the vibration and/or rotation of molecular bonds is the excitation of molecules from their ground (unexcited) state E_1, to a higher energy level E_2. The source of excitation is an applied electric field with frequency ν equal to

$$E_1 - E_2 = \Delta E = h\nu = \frac{hc}{\lambda}, \tag{4.1}$$

where E has units of electron volt (eV, or kcal/mol in S.I. units, 1 eV = 8065 cm^{-1}), h is the Planck's constant (3.99×10^{-13} kJ·s·mol^{-1}), c is the speed of light *in vacuo*, and $1/\lambda$ is the wavenumber (Banwell 1966). Equation (4.1) is known as Planck's Law.

For rotation to occur, only a small ΔE is needed: approximately a thousandth of an electron volt as shown in Fig. 1.1. Using Equation (4.1), this quantity of energy converts to a wavenumber of 1 cm^{-1}, which is in the same order as wavenumbers in the microwave frequency range (Ingram 1967). This means that a molecule absorbs specific microwave frequencies called *resonant frequencies* when it rotates, hence producing an absorption spectrum with specific reduced intensities in the microwave frequency range. This is the concept of chemical fingerprints.

Similarly, specific IR wavelengths are absorbed when an atom vibrates but a larger ΔE (approximately a tenth of an electron volt or 806.5 cm^{-1}) is required. Rotational activity is also present at this energy level but its influence on the molecule is effectively quenched by the stronger atomic vibrations (Ingram 1967).

Genuine vibrational and rotational activities can only occur in polar molecules[36]. A polar molecule contains atoms bound together by covalent bonds, however there is unequal sharing of electrons between atoms. For a pair of atoms, this results in one end of the molecule being more positive and the other more negative (Brown 2000). The overall molecule therefore acts like a dipole and possesses a dipole moment. When excited to energy level E_2, the molecule will experience a torque in its atomic bonds, and will either vibrate, rotate or do both according to the extent that E_2 deviates from the ground state E_1.

It should be noted here that the field of spectroscopy is not limited to the study of vibrations and rotations in molecules in the IR and microwave frequency ranges. As listed in Ingram (1967), examples of other molecular characteristics studied are:

- photon scattering from molecules (Raman effect using optical frequencies);
- transitions between nuclear spin energy levels (Nuclear Magnetic Resonance or NMR using radio frequencies);
- paramagnetic resonance absorption due to ions in crystalline lattices (using microwaves);
- ferromagnetic resonance of free radicals and F-centres (using microwaves); and
- electron resonance in metals and semiconductors (using microwaves).

In the next Section, IR spectroscopy will be introduced, with a brief discussion on the complementary use of Raman spectroscopy and NMR alongside IR measurements.

4.3 Infrared Medical Spectroscopy

The term 'fingerprints' is often used loosely in the terahertz research community as being unique molecular absorption peaks in the frequency domain for a specific type of material, which is measured using transmission mode THz spectroscopy. In the IR regime however, the absorption peaks (more commonly referred to as 'bands' in IR

[36] Non-polar molecules can also generate rotational and vibrational spectra as the electron distribution in the molecule is momentarily disturbed by an applied electric field (Townes and Schawlow 1955). An example is CO_2.

literature) are classified as either *group frequencies*, or *fingerprint frequencies* (Harwood *et al.* 1999).

Group frequencies typically exist above 45 THz (1500 cm^{-1}, where cm^{-1} is the unit for wavenumbers[37]), but can also exist below 45 THz. Group frequencies are characteristics of a *group* of vibrating atoms called functional groups. The vibration is localised within the functional group, i.e. the vibration does not involve other functional groups in a molecule. For example, if two functional groups in a molecule vibrate independent of each other, then their resonances are group frequencies. Group frequencies can therefore help identify common functional groups such as -OH, $-CH_3$, -COOH, $-NO_2$. Table 4.1 lists some functional groups and their IR absorption frequencies.

Fingerprint frequencies typically exist below 45 THz. They mainly capture the vibrational characteristics of a molecule as a whole, i.e. the vibration is not localised to a specific functional groups. Fingerprint frequencies therefore help identify specific whole molecules. As discussed in the previous paragraph, group frequencies do exist below 45 THz. Examples of functional groups with group frequencies below 45 THz are C-C and C-O.

At above 45 THz, a peak can be classified with confidence as a group frequency. By cross-referencing a correlation table, such as that shown in Table 4.1, the functional groups responsible for strong peaks can be identified. Smaller peaks are usually overtones (frequency harmonics of the functional groups). Below 45 THz, a peak may be either a group frequency or a fingerprint frequency. In the THz frequency range (0.1–10 THz), a peak is very likely to be a fingerprint frequency. The absence of peaks, particularly strong peaks, is an equally important indicator as the presence of peaks (Harwood *et al.* 1999).

An example of how IR spectra are used to differentiate between chemicals is shown in Fig. 4.1. The IR spectra of styrene and polystyrene appear similar to the untrained eye, but they become quite distinct when interpreted against a correlation table. For example, in the region straddling 90 THz, polystyrene has many broad and strong peaks; styrene however lacks the peaks just under 90 THz. According to Table 4.1, peaks in this region indicate the presence of aliphatic[38], straight-chained C-H bonds,

[37] Infrared (IR) spectroscopy literature specifies radiation in terms of wavenumbers with units of cm^{-1}, rather than frequency. For consistency in this Thesis, frequency is given in units of Hertz, namely MHz, GHz, and THz. Therefore, IR frequencies in this Thesis are quoted in units of THz.

[38] Aliphatic bonds form straight chains. Not to be confused with aliphatic compounds, which do not contain benzene rings.

Frequency (THz)	Wavenumber (cm^{-1})	Functional group	Comment (functional group(s); type of peak)
108	3600	O-H	Free, non-bonded; sharp
105–90	3500–3000	O-H	H-bonded; broad
		N-H	Amine or amide; often broad
99	3300	≡C-H	Sharp
93–81	3100–2700	C-H	Variable intensity peak
105–75	3500–2500	COO-H	Carboxylic acids; broad
75	2500	S-H	Weak
70.5	2350	CO_2	Carbon dioxide from path-length imbalance
66	2200	C≡C, C≡N	Often weak
66-57	2200–1900	X=Y=Z	Allene, isocyanate, azide, diazo groups, etc.; strong
55.5–49.5	1850–1650	C=O	Strong
49.5–45	1650–1500	C=C , C=N	Variable intensity
48	1600	C=C (aromatic)	Often weak
46.5	1550	$-NO_2$	Strong
40.5	1350	$-NO_2$	Strong
		$-SO_2-$	Strong
39–37.5	1300–1250	≡P=O	Strong
39–30	1300–1000	C-O	Alcohol, ether, ester; strong
34.5	1150	$-SO_2-$	Strong
25.5–21	850–700	aromatic C-H	Ortho-, meta-, para-disubstituted benzenes
24–21	800–700	C-Cl	Usually strong

Table 4.1: An extract of the IR correlation table of functional groups. There are no strict demarcations between the different frequency ranges listed here. Overlapping of regions often occur. For example, the ≡P=O functional group has been reported as far down as 1080 cm^{-1}. After Harwood *et al.* (1999).

which are present as [-CH-CH_2]$_n$ in polystyrene but absent in styrene. On the other hand, styrene has several sharp peaks above 45 THz. Referring to Table 4.1 again, strong peaks in this region indicate non-aromatic[39] C=C bonds, which are present in the -CH=CH_2[40] structure of styrene.

The types of vibration—stretch, scissor, wag—of the various functional groups can also be interpreted from the IR spectra. The broad peak just below 45 THz for polystyrene is caused by the "scissoring" vibration of the [-CH-CH_2]$_n$ bond. A review of vibrational modes is outside the scope of this Thesis but more information can be found in Colthup *et al.* (1964), and Banwell (1966).

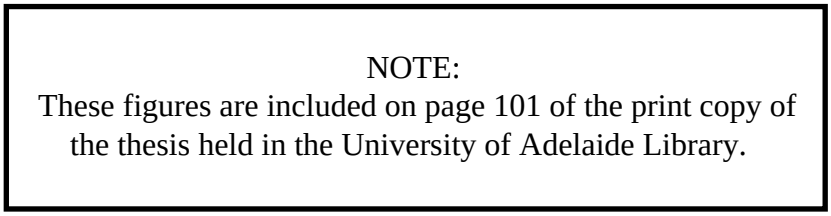

(a) IR spectrum of styrene (b) Chemical structure of styrene

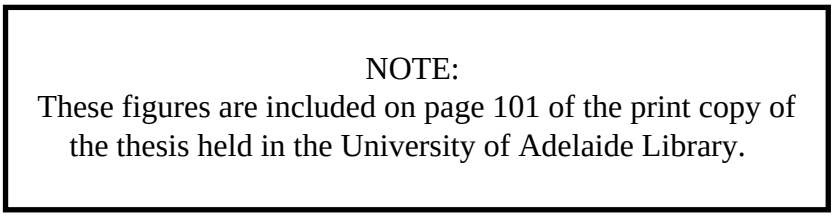

(c) IR spectrum of polystyrene (d) Chemical structure of polystyrene

Figure 4.1: A comparison of the IR spectra of styrene and polystyrene. The hexagons shown in the chemical structure schematics represent benzene (C_6H_6). After the National Institute of Advanced Industrial Science and Technology (2009).

[39] Aromatic bonds have alternating double and single links. Not to be confused with aromatic compounds which contain benzene rings.

[40] The -CH=CH_2 structure is called the vinyl group of olefins. Olefins contain at least one C=C bond.

Infrared spectroscopy is often used in conjunction with Raman spectroscopy[41]. Like most THz spectroscopic measurements, IR spectroscopy measures the residual signal that passes through a sample. Raman spectroscopy however measures the signal that is scattered at the incident surface of the sample. Raman and IR spectroscopies therefore complement each other because a weak IR spectrum usually results in a strong Raman spectrum, and *vice versa*. This is shown in Figs. 4.2(a) and 4.2(b).

NOTE:
These figures are included on page 102 of the print copy of the thesis held in the University of Adelaide Library.

(a) IR spectrum of styrene

(c) CNMR spectrum of styrene using ^{13}C isotopes

NOTE:
These figures are included on page 102 of the print copy of the thesis held in the University of Adelaide Library.

(b) Raman spectrum of styrene

(d) HNMR or proton NMR spectrum of styrene using ^{1}H isotopes

Figure 4.2: Infrared, Raman, and NMR spectra of styrene. (a and b) IR and Raman spectroscopies are often used together as they complement each other. For example, the strong dip at 1615 cm^{-1} for IR hints at the presence of C=C stretching. The strong peak at the same location for Raman confirms this guess; (c and d) NMR spectrographs of styrene. The symbol δ denotes the chemical shift: the fraction of frequency change from the reference frequency. After the National Institute of Advanced Industrial Science and Technology (2009).

[41] Raman spectroscopy is based on the Raman effect, which is named after its discoverer Sir Chandrashekhara Venkata Raman.

Raman spectroscopy provides more information about a sample than IR spectroscopy because it also quantifies the difference between a test sample and a reference sample. This useful analogy is attributed to Albert Einstein:

> "IR is analogous to putting a dime (10 cents) in a Coke machine and getting a Coke. Raman is analogous to putting $1.00 in a Coke machine and getting a Coke and 90 cents change."

One disadvantage of Raman spectroscopy is that it utilises a high power laser beam to illuminate a test sample. This heats the sample up and may cause a phase change, or even damage it. Alternatives to Raman spectroscopy are Raman hybrids, such as Fourier Transform Raman (FT/Raman) and Spatially Offset Raman Spectroscopy (SORS) (Matousek *et al.* 2005a, Matousek *et al.* 2005b, Matousek *et al.* 2006), and Nuclear Magnetic Resonance (NMR) spectroscopy[42].

Although NMR operates in the radiofrequency range (60–600 MHz), it is introduced in this Section because of its frequent use in conjunction with IR spectroscopy. Nuclear Magnetic Resonance utilises a magnetic field to study the magnetic and angular moments of a known magnetically susceptible nucleus that is added to a test sample, with the aim of identifying the structure of atoms in the test sample. In the examples shown in Figs. 4.2(c) and 4.2(d), ^{13}C and ^{1}H isotopes[43] are the magnetically susceptible nuclei that are added separately to styrene. The moments of these isotopes depend on the alignment of either the carbon (if ^{13}C used) or hydrogen (if ^{1}H used) atoms in styrene; the moments manifest as unique resonant frequencies ν_{test} akin to those in THz and IR spectroscopy, however ν_{test} lies in the radiofrequency range. Furthermore, NMR results are reported in scientific units which are not directly comparable to THz and IR measurements. As seen in Figs. 4.2(c) and 4.2(d), the units are given as the chemical shift (frequency shift) relative to a known reference frequency ν_{ref}. In the examples presented here, the resonant frequency of the methyl group (CH_3) in tetramethylsilane (TMS, $Si(CH_3)_4$) provides the reference frequency. The chemical shift δ of a test sample is therefore defined as

$$\delta = \frac{\nu_{\text{test}} - \nu_{\text{ref}}}{\nu_{\text{ref}}} \times 10^6 . \tag{4.2}$$

[42] Proposed by Isidor Isaac Rabi in 1938, and refined by Felix Bloch and Edward Mills Purcell in 1946.

[43] A chemical element can have two or more species of atoms called nuclides that have the same atomic number and nearly identical chemical behaviour, but have differing atomic mass or mass number, and differing physical properties. For example, ^{1}H and ^{3}H are isotopes of hydrogen. They both have hydrogen nuclei but have different atomic masses. Furthermore, ^{3}H is radioactive whereas ^{1}H is not.

The δ spectrum, like the IR spectrum (Table 4.1), can be divided into regions where particular atomic bonds are most active. For example, the peaks at $\approx$ 130 ppm in Fig. 4.2(c) correspond to C=C bonds, whereas the peaks at $\approx$ 7.25 ppm in Fig. 4.2(d) correspond to C=C-H bonds. Tables of chemical shifts and details on NMR can be found in Hore (1995), and Brown (2000).

The next Subsection introduces the modalities and analytical methods used in IR spectroscopy.

4.3.1 Common Modalities and Analytical Tools for IR Spectroscopy

As introduced in Sections 1.3 and 1.4, the Fourier Transform Infrared (FTIR) spectrometer is one of the most ubiquitous IR modalities today. Newer FTIR systems have the capability to perform both spectroscopic and imaging measurements through the use of detector arrays (e.g. focal plane arrays and linear array detectors). Other IR systems capable of both spectroscopy and imaging are univariate and Attenuated Total Reflectance (ATR) imaging systems. While most IR systems are sufficiently small to fit on the top of a laboratory bench, large synchrotrons (Section 2.7.1) are also sources of IR radiation (Gazi *et al.* 2005).

Regardless of the IR spectroscopic modality used, the measured data can always be presented as shown in Fig. 4.2(a) where transmittance (or absorbance) is plotted against frequency. The information to be interpreted from this type of plot is fairly limited in that it only identifies and quantifies the absence or presence of functional groups. A wider and more powerful set of techniques called *chemometrics* allows for the extraction of information that is otherwise not immediately obvious.

Chemometrics is the science of applying mathematical, statistical, graphical and/or symbolic methods to data for the purpose of extracting maximal information. In the realm of engineering, chemometrics is equivalent to applying linear algebra and signal processing algorithms that firstly smooth data, and then extract and cluster features, such as eigenvectors, for the purpose of *classification* or *calibration* (finding the link between blocks of variables).

Two frequently encountered examples of chemometric techniques are:

- multivariate data analysis, namely Principal Component Analysis[44], for classification such as in pattern recognition and clustering; and
- univariate and multivariate regression for calibration.

The mathematics behind Principal Component Analysis[45] for pattern recognition, and univariate and multivariate regression can be found in Brereton (2003). An example of the application of Principal Component Analysis will be presented later in Fig. 4.3(b).

Other areas of science that have benefited from chemometrics are hyperspectral imaging, multivariate process modelling, Quantitative Structure-Activity Relationships (QSAR), as well as pattern recognition of THz data (Ferguson *et al.* 2002a, Te *et al.* 2002).

4.3.2 Applications of Infrared Spectroscopy

As described in Section 4.3, IR spectroscopy is used extensively in the study of the atomic structure and vibrational behaviour of chemicals. The latter, called IR vibrational spectroscopy, is also used in many medically oriented IR spectroscopic applications introduced in this Section. These applications are closely related to THz studies of similar materials, hence useful information can be gained from examining the results from these IR studies.

Infrared Spectroscopy of Cells

As shown in Fig. 1.1, the wavelength of the IR range (10^{-6} m up to 10^{-4} m) is at the same order as the size of cells and some of their contents, hence the IR range is ideal for studying morphological and chemical changes in cells.

The study of human cervical tissue has been one area of active IR research since 1991 (Wong *et al.* 1991). With the advent of FTIR microspectroscopy, examination of exfoliated cervical cancer cells has become possible (Wood *et al.* 1996, Wood *et al.* 1998, Romeo *et al.* 2003, Wood *et al.* 2004, El-Tawil *et al.* 2008). The aim of most examinations is to study the types and contents of exfoliated cells that are obtained from women who have had abnormal or inconclusive Papanicolaou smear tests (Pap

[44] Invented by Karl Pearson in 1901. Also known as the discrete Karhunen-Loève transform, Hotelling transform or Proper Orthogonal Decomposition (POD).

[45] The acronym for Principal Component Analysis is PCA, but it is not used in this Thesis because it conflicts with the acronym for photoconductive antennas.

smears). A complex mixture of cells is inevitably obtained from smears: endocervical (from the endocervix), squamous ectocervical (scale-like cells from the ectocervix), erythrocytes (red blood cells), leukocytes (white blood cells), and thrombocytes (platelets). In addition, other contaminants such as bacteria, yeast, and remnants of the cervical sampling instruments are often present (Wood *et al.* 1998). The removal of unwanted cells using buffers and filtration is tedious but has since been eased using commercial processing techniques such as ThinPrep (Hologic Inc. 2008).

Fig. 4.3(a) shows a comparison of the IR spectra of normal endocervical and normal ectocervical cells with the HeLa cervical cancer cell line[46]. The dips and peaks can be attributed to the known chemical composition of cervical cells. For example, the 1650 cm^{-1} band is described in Table 4.1 as being caused by the C=O functional group. For all three cell types, this observation is consistent with presence of amide (N-C=O) in tissue protein (Wong *et al.* 1991, Wood *et al.* 1998). The strong band at 1246 cm^{-1} for the HeLa cells is unseen in the normal cells, hence could be a biomarker for cervical cancer.

The development of FTIR imaging has enhanced the way data is analysed and presented (Bambery *et al.* 2004, Heraud *et al.* 2007). Figure 4.3(b) shows a comparison of high resolution optical images A and B with a univariate (single frequency) FTIR image C taken at 1024 cm^{-1} wavenumbers. Glycogen (links of CH_2OH) in the glandular epithelium absorbs strongly at this frequency, hence should be visible in a pseudo-coloured FTIR image. The brighter regions (cyan, yellow, red) do indeed co-register with the optical image. Image D in Fig. 4.3(b) shows the result of applying chemometrics for multivariate (multifrequency) clustering of regions with similar spectral features. Spanning from 1800 cm^{-1} to 800 cm^{-1} wavenumbers, this 7-cluster map reveals regions that co-register remarkably well with optical image A.

Other types of cancer cells, such as prostate, pancreatic and lung, have also been probed successfully with FTIR spectroscopy. This means that FTIR spectroscopy could be employed as an additional diagnostic tool for reducing false negative detections that arise from existing cell cytological[47] analysis.

[46] The HeLa cervical cancer cell line is derived from the cervical cancer cells that were taken from Henrietta Lacks, who died from cervical cancer in 1951. Lacks and her family had no knowledge that her cells were being propagated and commercialised; her family eventually learnt about the HeLa cervical cancer cell line in the 1970s (Masters 2002).

[47] The branch of biology that studies the structure, multiplication, and life of cells.

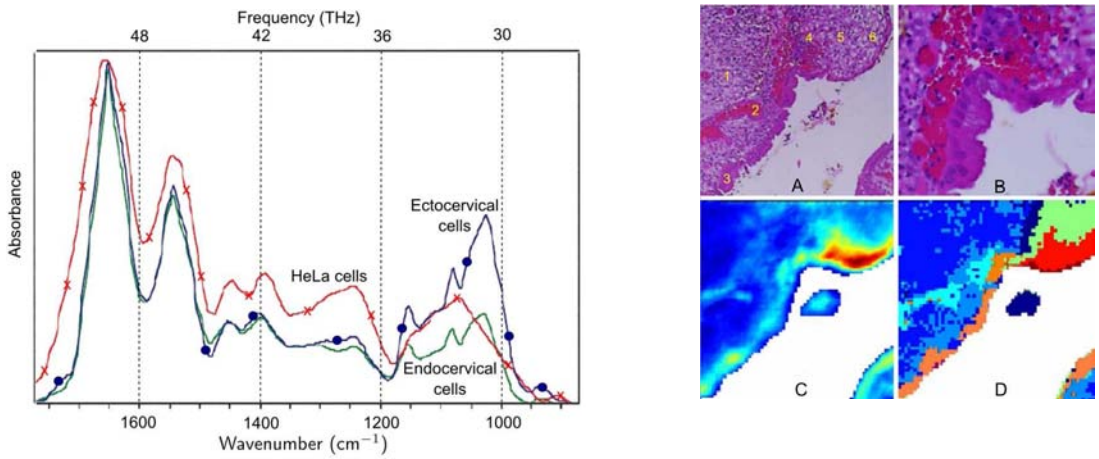

(a) IR spectra of HeLa cervical cancer cells and two normal types of cervical cells

(b) FTIR images of a cell taken from the cervix

Figure 4.3: Infrared spectroscopy of cervical cancer cells. (a) FTIR microspectroscopy allows probing of small structures such as cells. The composition of an individual cell can be analysed and compared against a standard, such as the HeLa cervical cancer cell line. After Wood *et al.* (1998). (b) Data obtained from FTIR imaging can be classified using pattern recognition algorithms, and then pseudocoloured to facilitate comparison against optical images. Regions with abnormal spectral responses are therefore easily identifiable. After Wood *et al.* (2004).

Infrared Spectroscopy of Skin

Infrared spectroscopy has been applied to the study of the structure of human skin through the observation of IR scattering effects from the top layers of skin. This is an ideal endeavour because the wavelengths of IR radiation are in the same order as the thicknesses of the outer skin layers (tens to hundreds of microns). However, there is a limitation on the penetration depth of IR radiation into skin as many frequencies in the broad IR spectrum are strongly attenuated by water (in this case, water in biotissue). There is a window in the spectrum where IR is unaffected by water—this "therapeutic window" lies between 0.6 and 1.3 μm (Anderson and Parrish 1981, Parrish 1981), which is the near-IR region of the spectrum. An example of how IR is used in deep tissue analysis is presented in the next Subsection.

In skin studies, IR spectroscopy has been used to profile the depth of skin (Viator *et al.* 2003) and the hydration of skin (Attas *et al.* 2002b, Attas *et al.* 2002a). These studies are important for the medical management of burns and skin diseases. Thermal IR observation of temperature changes in burns and diseased skin is an alternative to IR

spectroscopy (Jones 1998). Figure 4.4 shows some results from these skin studies. Most skin-related IR studies are performed in reflection mode due to the aforementioned attenuation by water in biotissue. Attenuated total reflection (ATR) is one means of performing reflective IR spectroscopy.

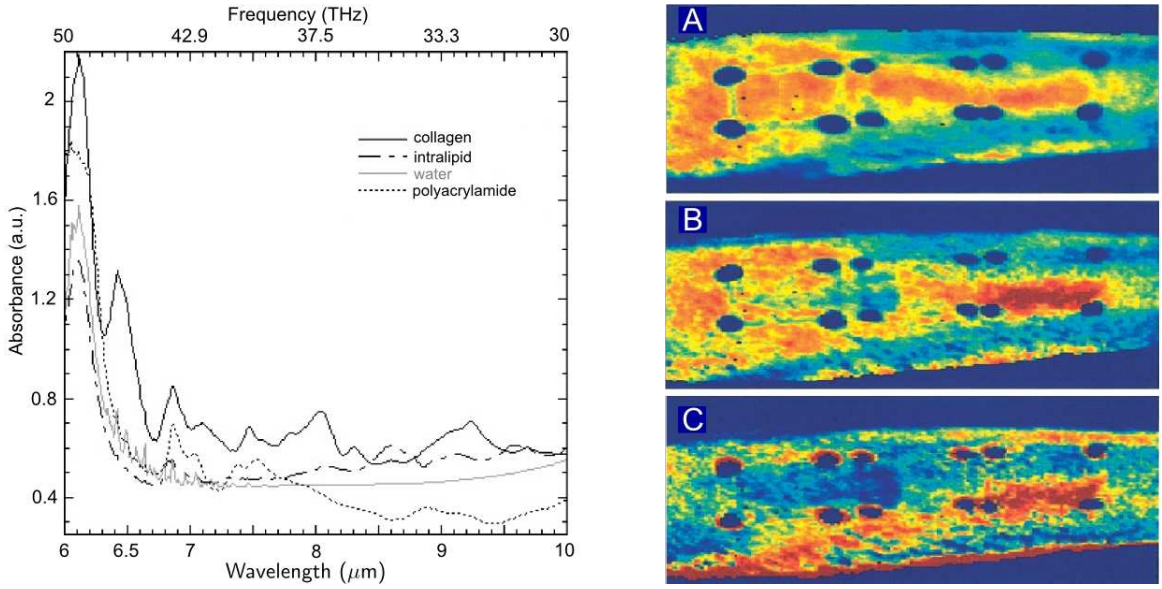

(a) IR spectrum of synthetic skin

(b) Hydration analysis of skin on the forearm

Figure 4.4: Infrared spectroscopy of synthetic skin. (a) IR spectroscopy reveals the different chemical layers in synthetic skin. The collagen layer is identified by three peaks: 6.1 μm, 6.45 μm, and 8.1 μm correspond respectively to hydrated C=O group stretching, hydrated O-H group stretching, and C-N stretch. The peaks at 6.8 μm and 7.4 μm are due to C-H bending in both collagen and polyacrylamide. The $(CH_3)CH$ stretch in intralipid causes the 8.6 μm peak. After Viator *et al.* (2003). (b) In these images, the volunteer's wrist is located on the right side. (A) Three rectangular regions were demarcated using four blue circles per region. Moisturiser was applied to the rightmost region, and acetone to the leftmost region; (B) The arm was imaged 30 minutes later with IR radiation at 206.9 THz; (C) The difference between images A and B reveals the varying hydration levels in the three regions. After Attas *et al.* (2002b).

The structure of skin is highly stratified and suffers from multiple occlusions due to objects such as hair follicles, sweat glands and blood vessels. Skin is therefore considered a turbid media in the IR frequency range. In order to understand and/or predict the propagation of IR radiation in skin, mathematical models utilising stochastic techniques, such as the Monte Carlo algorithm, have been created (Wilson and

Adam 1983, Prahl *et al.* 1989, Song *et al.* 1999). For example, the extent of light scattered from skin has been quantified using mathematical models that are verified with experimental data (Matcher *et al.* 1995).

Synthetic substitutes for real skin—skin phantoms—are also used as models for studying the propagation of IR (Lu *et al.* 2000, Viator *et al.* 2003). Examples of skin and tissue phantoms are shown in Fig. 4.5.

NOTE:
These figures are included on page 109 of the print copy of the thesis held in the University of Adelaide Library.

(a) Various phantom types (b) Arm phantoms (c) Cone phantoms

Figure 4.5: Phantoms for IR spectroscopy. (a) Various types of phantoms, including neonatal head phantoms. (b) Arm phantoms with embedded rods to mimic bones. (c) General purpose cone phantoms. The phantoms are made from epoxy. After University College London (2005).

The creation of such phantoms require a good understanding of the behaviour of skin in the IR frequency range. Optical properties in the IR frequency range have been reported in literature, but no central database is known to exist to date. Nonetheless, these scattered pieces of information are useful starting points for various unknown THz optical properties.

Infrared Spectroscopy and Imaging of Deep Biotissue

The "therapeutic window" lying between 0.6 and 1.3 μm (Anderson and Parrish 1981, Parrish 1981) has allowed IR spectroscopy to probe biological targets that lie a few centimeters inside the human body. This is extremely beneficial for the detection of breast cancer tumours. Near-IR spectroscopy, imaging and tomography have been investigated as alternatives to ionising X-ray mammograms (Colak *et al.* 1999, Hawrysz and Sevick-Muraca 2000, Wang *et al.* 2005, Wang *et al.* 2006).

An example of a X-ray mammographic image is shown in Fig. 4.6(a). This image is fuzzy, which can result in false negatives. In addition, patients often experience discomfort when undergoing mammograms due to the awkward positioning of the breast

NOTE:
These figures are included on page 110 of the print copy of the thesis held in the University of Adelaide Library.

(a) X-ray mammographic image (b) Near-IR image (c) The SoftScan near-IR system

Figure 4.6: Infrared spectroscopy of biotissue. The high number of false negatives from mammograms has led to the development of IR spectroscopy as a complementary scanning technique for breast cancer screening. The awkward way a patient's breast is scanned during a mammogram has led to an overhaul of the scanner design, resulting in one where the patient lies in a prone (face down) position so that the breast hangs downwards without the need for painful and obstructive clamps. The scan is therefore more comfortable for the patient, and may increase the volume of biotissue inspected by each scan. After Advanced Research Technologies Inc. (2008).

on the X-ray scanner. A more patient-friendly commercial near-IR breast scanner is shown in Fig. 4.6(c). This system, developed by Advanced Research Technologies in Canada, is presently in use in Canada and Europe, but is awaiting approval from the American Food and Drug Administration (FDA) (Advanced Research Technologies Inc. 2008). Figure 4.6(b) shows the near-IR image of the same breast shown in Fig. 4.6(a). The red region clearly shows the presence of a tumour.

Infrared Spectroscopy and Imaging of Infant Brains

Another medical application that takes advantage of the IR "therapeutic window" is IR spectroscopy of infant brains. The left diagram in Fig. 4.7(a) shows the non-invasive spectroscopic technique that was developed in 1977 by Jöbsis. This early technique was capable of detecting changes in the volume and oxygenation of blood inside brain tissue of very premature babies with the aim of monitoring infant development (Jöbsis 1977, Kurth *et al.* 1995, Meek 2002).

Improvements have since been made to Jöbsis' design to allow near-IR imaging of the brain. The right diagram in Fig. 4.7(a) shows a multi-electrode technique that enables *in vivo* functional brain imaging (Hebden *et al.* 2002, Hebden 2003, Aslin and

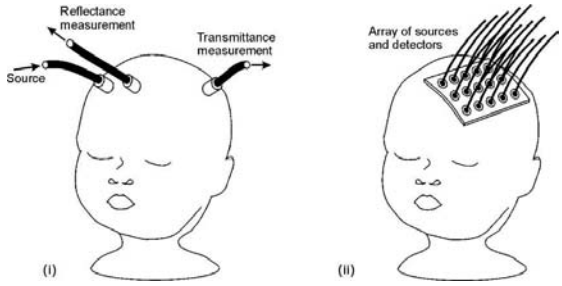

(a) IR spectroscopes for infant brains

(b) IR functional brain imager on a 5-week old infant born 2 months premature

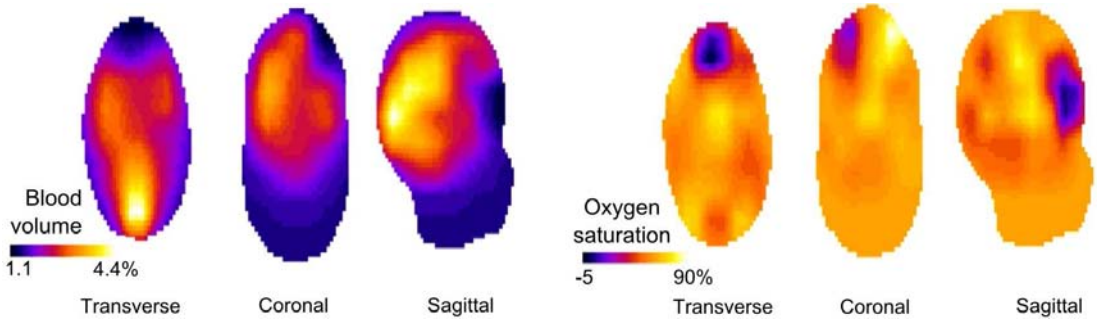

(c) Functional brain imaging results

Figure 4.7: Infrared spectroscopy of human infant brains. (a) (Left) Early design of a non-invasive IR spectroscope for monitoring blood volume and oxygenation in an infant's brain; (Right) A multi-electrode design which allows functional brain imaging to be performed. (b) Integrating the multi-electrode system into a helmet that fits comfortably on the infant's head for several hours. (c) Functional brain imaging of an infant with suspected perinatal hemorrhage. In the coronal view of blood volume, the asymmetry indicates hemorrhaging. After Hebden *et al.* (2002) and Hebden (2003).

Mehler 2005). The electrodes are housed inside a fibre helmet, as shown in Fig. 4.7(b), which is worn on the premature infant's head. Results from functional brain imaging of a premature infant with perinatal hypoxic-ischaemic brain injury[48] are presented in Fig. 4.7(c).

Infrared Spectroscopy of Blood and Blood Vessels

Liquid spectroscopy is another area where IR has been used. *In vivo* whole blood measurements have been conducted in the near-IR range to determine the concentration of oxygenated and deoxygenated hemoglobin (Kim *et al.* 2005). The purpose of such a study is to monitor blood oxygenation dynamics in tumours. Glucose concentration in

[48] Damage to brain cells due to inadequate oxygen prior to or during birth.

whole blood has also been studied with FTIR spectroscopy (Shen *et al.* 2003). The mid-IR has specifically been used to study *ex vivo* whole blood in order to determine if the cellular constituents of blood significantly scatter IR (Guo *et al.* 2004). The mid-IR response of whole blood is comparable to that of water, thus making it possible to apply *in vivo* diffuse reflectance spectroscopic imaging in the mid-IR range on subcutaneous blood vessels. Figure 4.8 shows the result of using multi-wavelength spectral imaging on chicken skin. The blood vessels are clearly revealed in the mid-IR range.

NOTE:
These figures are included on page 112 of the print copy of the thesis held in the University of Adelaide Library.

Figure 4.8: Infrared spectroscopy of blood vessels. (a) Optical image of the surface of chicken skin reveals no detail about the underlying blood vessels. (b) Focusing 88.2 THz (3.4 μm wavelength) IR radiation at the surface still reveals little detail. (c) Diffuse reflectance spectroscopic imaging at 65.2 THz (4.6 μm wavelength) requires the radiation to be focused at a depth of 4.6 μm in order for details of the blood vessels to be seen. (d) Similarly for the 88.2 THz radiation, the radiation is focused 3.4 μm under the skin. (e) Juxtaposing and pseudocolouring of images c and d results in a clear revelation of the structure of blood vessels in the subcutaneous layer of chicken skin. After Guo *et al.* (2004).

4.4 Microwave Medical Spectroscopy

In Section 1.3.1, microwave spectroscopy of gas was introduced as a successor of molecular spectroscopy dating back to the 19th century; the development of the magnetron in 1933 allowed the use of microwave frequencies above 3.33 GHz. With the advent of radar technology during the Second World War, high frequency microwave generators such as the travelling-wave tube became more accessible for microwave spectroscopy. Propagation of microwaves in waveguides had been studied extensively in the development of radar, hence waveguides emerged as one of the new post-war techniques for microwave spectroscopy.

Unlike in IR spectroscopy where the spectral fingerprints of most chemicals can be generalised as being attributed to specific functional groups (Table 4.1) and to the type(s) of vibration, microwave spectral fingerprints are unique to each pure chemical measured.

Microwave spectroscopic results provide an insight into the structure of the molecule and the chemical nature of its bonds. For example, bond lengths and their angles can be deciphered with a high degree of accuracy. The high sensitivity of microwave spectrometers also results in microwave spectra with hyperfine details that yield information about the nuclei of individual atoms (Ingram 1967). Microwave spectroscopic information is therefore tabulated to suit each individual chemical. Examples of submillimeter , millimeter, and microwave spectral line catalogues covering an extensive number of chemicals are found in (Poynter and Pickett 1985, Pickett *et al.* 1998).

Microwave spectral features of pure chemicals are prone to broadening and shape deformation due to variation in pressure, temperature, saturation, collisions between molecules and Doppler shifts (Townes and Schawlow 1955). While these effects may initially appear to be disadvantageous for microwave spectroscopy, they actually aid in determining the types of interatomic van der Waals forces (e.g. dipole-dipole, quadrupole-dipole). Microwave spectroscopy is therefore a powerful tool in the study of pure chemicals.

Section 4.4.1 highlights several types of microwave spectrometers and the types of samples measured. Many microwave spectrometers have been introduced previously in Chapter 2, hence will not be elaborated on again here. The emphasis of Section 4.4.2 is on biotissue measurements that yield optical properties which can be extrapolated into the lower THz frequency range.

4.4.1 Common Modalities of Microwave Spectroscopy

An assortment of well-established measurement apparatus is available for measuring biotissue with microwave radiation. Klystrons, magnetrons, spark discharge, triode electronic tubes, travelling wave tubes and backward wave tubes are the most common sources of microwave radiation (Townes and Schawlow 1955). Most of these have been in existence since before the Second World War; techniques for channelling the radiation onto a test sample are, however, more recent developments. An early technique used to probe biological materials was based on standing waves in waveguides and coaxial lines (Roberts and von Hippel 1946). Ultrahigh frequency (UHF, 0.2–1 GHz)

diathermy[49] was developed shortly afterwards for measuring the impedance of various biotissue (Schwan and Carstensen 1953). Both techniques were used extensively before newer measurement techniques were developed in the late 1970s. For example, time domain spectrometers utilising coaxial lines (Dawkins *et al.* 1979), waveguide cells (Steel *et al.* 1987), waveguides (Richards and Sheppard 1991), resonant cavities operating between 1.5 and 6 GHz (Land and Campbell 1992), and microwave network analysers. An example of a modern microwave spectrometer is shown in Fig. 4.9.

NOTE:
These figures are included on page 114 of the print copy of the thesis held in the University of Adelaide Library.

(a) An industrial microwave spectrometer

(b) Sample passing through waveguide is scanned with microwaves

Figure 4.9: Example of a microwave spectrometer. The Guided Microwave Spectrometer from Thermo Scientific provides a non-contact method for monitoring a sample passing through the waveguide. The system operates from 0.2–3.2 GHz, and can monitor moisture, pH, viscosity, fat, sodium, alcohol, and solvent levels in the sample. Example sample types are liquids, grains, slurries and pastes (e.g. ground meat). After Thermo Fisher Scientific Inc. (2009).

4.4.2 Applications of Microwave Spectroscopy

Biotissue is far more complex in composition and structure than pure chemicals, and fine spectral detail in the microwave frequency range is generally suppressed by the collective response of the biotissue. Microwave spectroscopy has been used on biotissue because of initial concerns pertaining to the exposure of humans to microwaves from radar (Schwan and Li 1956), hence heating of biotissue by microwaves was the focus of most early studies (Schwan and Carstensen 1953, Schwan and Li 1953).

Safety is still a concern today, particularly with the proliferation of relay antennas for cellular telephones. There is an ongoing development of mathematical models for

[49] Diathermy is the use of electric currents to generate heat in biotissue for medical or surgical purposes.

analysing the specific absorption rate (SAR) of microwaves in various parts of the human body (Stuchly 1994, Dimbylow 1997, Stuchly and Dawson 2000, Dimbylow 2002, Gjonaj *et al.* 2002, Ohishi *et al.* 2002, Fukunaga *et al.* 2004). Numerical methods such as the Finite Difference Time Domain (FDTD) method and Finite Element Method (FEM) are frequently used for computational modelling of microwave propagation in biotissue (Wang and Fujiwara 1999, Bulyshev *et al.* 2001, Gajšek *et al.* 2001, Mazzurana *et al.* 2003, Kosmas *et al.* 2004).

In order to develop models of the body, optical properties of various excised biotissue from animals and humans have been studied, including:

1. excised dog brains, 0.01–10 GHz using diathermy (Foster *et al.* 1979);
2. muscle of barnacles, 0.01–17 GHz using a transmission line (Foster *et al.* 1980);
3. dog cancer tumours, 0.01–17 GHz using an impedance meter and a microwave network analyser (Schepps and Foster 1980);
4. brain cortex, spleen and liver of cats and rats, 0.1–10 GHz using a coaxial line (Stuchly *et al.* 1982);
5. rabbit ocular tissue measured at 37°C, 0.01–10 GHz using a time domain spectrometer-coaxial line (Gabriel *et al.* 1983);
6. lens cortex of rabbit, 2–18 GHz using a coaxial line (Steel *et al.* 1984);
7. rabbit ocular tissue in supercooled and frozen states, 0.01–10 GHz using a time domain spectrometer-coaxial line (Gabriel and Grant 1985);
8. excised rabbit brain, 1–18 GHz using standing-wave profile (Steel and Sheppard 1985);
9. rabbit blood, water, ethanol and methanol, 35 GHz using a waveguide cell (Steel *et al.* 1987);
10. rabbit tissue, water and various liquids, 35 GHz using a waveguide (Steel and Sheppard 1988);
11. liquids, up to 20 GHz using a coaxial probe (Wei and Sridhar 1989);
12. common solvents and water, 0.95–89 GHz using a travelling wave tube (Barthel *et al.* 1990);

13. high loss liquids (water and formamide), 57–82 GHz using a waveguide (Alison and Sheppard 1990, Alison and Sheppard 1991);
14. *in vitro* human breast tissue, 3.2 GHz using resonant cavity perturbation (Campbell and Land 1992);
15. human blood, 29–90 GHz using a waveguide (Alison and Sheppard 1993);
16. rat liver, using NMR (Moser *et al.* 1996);
17. various biological and organic liquids, up to 110 GHz using a two-port waveguide (Duhamel *et al.* 1997);
18. rat brain, using a two-port microstrip (Tofighi and Daryoush 2002a, Tofighi and Daryoush 2002b);
19. *ex vivo* human brain slices, 0.5–18 GHz using a vector network analyser in transmission and reflection (Axer *et al.* 2002); and
20. human breast tumours, using an ultrawide-band (UWB) synthetic planar array (Fear and Stuchly 2000, Li and Hagness 2001, Fear *et al.* 2002, Li *et al.* 2004) (see Fig. 4.10).

Excellent literature surveys of microwave biotissue studies conducted up till 1996 can be found in Gabriel *et al.* (1996a, 1996b, 1996c), and Gabriel and Gabriel (1997a). These references contain compilations of the optical properties of various human and animal biotissue, which will be referred to in Chapter 9 of this Thesis.

4.5 Terahertz Medical Spectroscopy

In Sections 1.4.1 and 1.4, THz sensing of proteins and biotissue were briefly introduced. Terahertz's susceptibility to absorption by water was also mentioned. The influence of water, either in samples or in the surrounding atmosphere, poses many challenges for all THz researchers.

4.5.1 Water Absorption in the THz Frequency Range

It has been known for several decades by submillimeter and far-infrared (FIR) research groups that frequencies in the THz region are strongly absorbed by water vapour

NOTE:
These figures are included on page 117 of the print copy of the thesis held in the University of Adelaide Library.

(a) Before application of a skin subtraction algorithm

(b) After application of a skin subtraction algorithm

Figure 4.10: Microwave imaging of a breast phantom. Ultrawide-band microwave imaging of a breast phantom containing an embedded phantom tumour that has a diameter of 6 mm, and is located at position x = 40 mm, y = 40 mm. The view shown here corresponds to a slice along the coronal plane. A circular array of antennas surrounds the breast phantom. The black lines mark the location of the inner skin surface enveloping the breast tissue. (a) Reflections from skin dominate the detected signal but the effect of skin can be removed by applying a skin subtraction algorithm. (b) Reflections from the embedded tumour are revealed as seen by the dark red region. After Fear and Stuchly (2000).

and liquid water. Since the 1970s, researchers have used interferometric techniques to quantify the influence of water on signal strength in the submillimeter and FIR frequency ranges. Analytical models based on Debye and Cole-Cole theories have been used to predict and explain the molecular behaviour of water over a range of frequencies in the following publications:

1. water vapour, up to 0.752 THz using microwave spectroscopy (de Lucia *et al.* 1972);

2. water and ice, critical survey of measurements and analytical models from 3 Hz to 30 THz (Ray 1972);

3. various liquids (water, chloroform, bromoform, chlorobenzene), 4.5–7.5 THz using Fourier Transform Spectroscopy (Afsar *et al.* 1976);

4. water and heavy water (D_2O), 0.18–13.5 THz using Fourier Transform Spectroscopy (Afsar and Hasted 1977);

5. water vapour, up to 21.45 THz using both microwave and FIR instruments (Messer *et al.* 1983);

6. liquid water, up to 0.12 THz using Fourier Transform Spectroscopy (specifically a polarising interferometer) (Hasted *et al.* 1985);

7. temperature variation of water from 282–313 K (10-40°C), 0.18–0.42 THz using Fourier Transform Spectroscopy (Hasted *et al.* 1987); and

8. molecular dynamics of water, 0.66–4.26 THz using laser spectroscopy and broad band interferometric spectroscopy (Evans *et al.* 1987).

By the late 1990s, many of the measurements listed above were repeated using THz-time domain spectroscopy (THz-TDS). The accuracy of the measurements made in the lower THz range were improved with THz-TDS, allowing for more realistic fit of measured data with analytical models (van Exter *et al.* 1989b, Thrane *et al.* 1995, Kindt and Schmuttenmaer 1996, Kindt and Schmuttenmaer 1997, Viant *et al.* 1997, Rønne *et al.* 1997, Rønne *et al.* 1999, Kindt and Schmuttenmaer 1999, Rønne and Keiding 2002). To highlight the benefit of using THz-TDS for measurements in the THz frequency range, a chronological comparison of the spectral features of water vapour is given in Table 4.2.

As a final note, water has also been investigated using high power THz sources such as the free electron laser (Xu *et al.* 2006a), which is introduced in Section 2.7.2. A p-germanium high power, tunable laser spectrometer has also been employed to perform THz spectroscopy of water (Bergner *et al.* 2005).

The Effect of Water Vapour in the THz Frequency Range

Water vapour, being in a gaseous state, has vibrational and rotational modes similar to those described in Sections 4.3 and 4.4. These modes absorb specific THz frequencies, which are called *water absorption lines* or simply *water lines*. The rightmost column in Table 4.2 lists the nine water lines that are usually referred to in THz literature. Figure 4.11 illustrates the effect of water vapour on a measured THz signal as compared to a nitrogen-purged environment that contains less water vapour.

In the experimental work performed in this Thesis, although nitrogen purging of the test environment is used to reduce the effect of water vapour, some artifacts from residual water vapour are still present.

Using microwave, submillimeter and FIR techniques in 1972 (unit: THz)	Using microwave and FIR techniques in 1983 (unit: THz)	Using THz-TDS in 1989 (unit: THz)
Not found	0.022	Not found
Not found	0.183	Not found
0.321	Not found	Not found
Not found	0.325	Not found
Not found	0.381	Not found
0.437	0.437	Not found
0.439	0.439	Not found
0.443	0.443	Not found
Not found	0.448	Not found
0.470	0.47	Not found
0.474	0.475	Not found
0.488	Not found	Not found
Not found	0.504	Not found
Not found	0.557	0.558
0.62	0.62	Not found
0.752	0.752	0.753
Not found	0.916	Not found
Not found	0.970	Not found
Outside measurement range	0.988	0.989
Outside measurement range	Not found	1.099
Outside measurement range	Not found	1.115
Outside measurement range	Not found	1.165
Outside measurement range	Not found	1.209
Outside measurement range	Not found	1.230
Outside measurement range	Not found	1.412

Table 4.2: Discovery of water vapour lines. A comparison of the frequencies of known water vapour lines in the THz frequency range over 17 years shows an improvement in measurement accuracy particularly in the lower THz range. The nine water vapour lines discovered using THz-TDS are the standard ones referred to in most THz literature, including this Thesis. After de Lucia *et al.* (1972), Messer *et al.* (1983), and van Exter *et al.* (1989b).

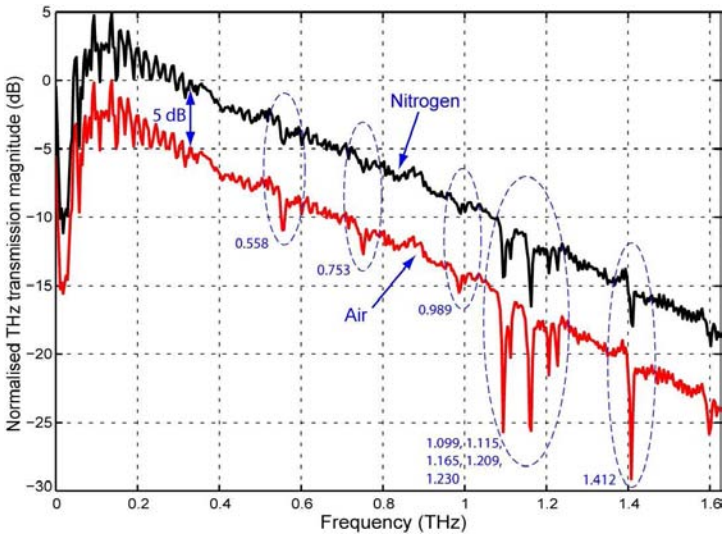

Figure 4.11: Water vapour lines in the THz frequency range. A comparison of the effect of two transmission media—air (lower red plot) and nitrogen (upper black plot)—on two THz signals. Because the plots originally overlap, the upper plot has been offset upwards by 5 dB for clarity. Air contains water vapour that attenuates the THz signal at the water lines. This is evident by the dips in this plot. Nitrogen is used to purge water vapour in the THz test environment, hence attenuation from water vapour is significantly reduced.

The Effect of Liquid Water in the THz Frequency Range

Liquid water, unlike water vapour, behaves like biotissue in that only the collective absorption response of all water molecules is observed. The collective absorption response of water is one that severely reduces the measured signal strength. Figure 4.12(a) illustrates the reduction in the strength of a THz signal after it propagates through 1 mm of water. The reduction is quantified using the absorption coefficient α as shown in Fig. 4.13(a). The absorption coefficient, which is formally introduced in the next Chapter, can be interpreted as the extent of reduction in the THz signal's intensity as it passes through one centimeter of the test material. Comparing the α values of water and (much thicker) bulk polyethylene (Fig. 4.13(b)), it is evident that liquid water strongly absorbs THz.

In Section 4.5.4, a discussion on the percentage of water in the human body will show that fresh biotissue contains a high proportion of water, hence fresh biotissue has similar α values as liquid water, making it opaque to THz radiation.

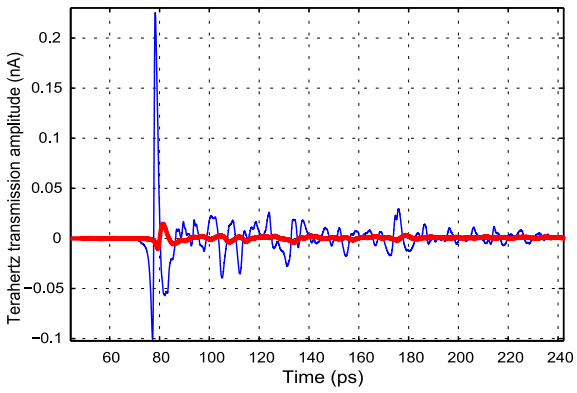

(a) THz transmitted signal through 1 mm of water

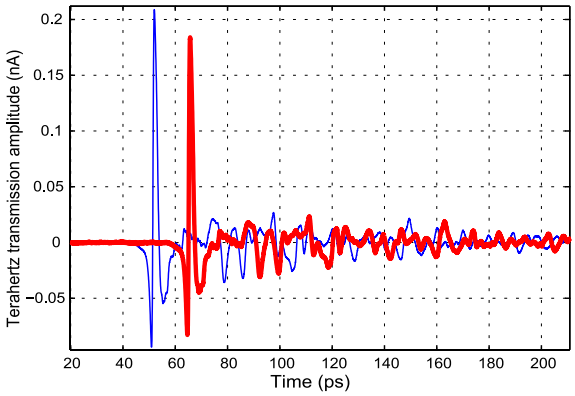

(b) THz transmitted signal through 8 mm of bulk polyethylene

Figure 4.12: Terahertz absorption by liquid water. (a) Time domain plots of measured THz signals with (red thick plot) and without (blue thin plot) transmission through 1 mm of water. The amplitude of the signal after propagating through water has been severely reduced. (b) Instead of water, 8 mm of bulk polyethylene was used as the sample (red thick plot). Although the polyethylene is much thicker than the water sample, the transmitted THz signal is significantly delayed but only slightly reduced in amplitude when compared to the signal propagating in free-space (blue thin plot).

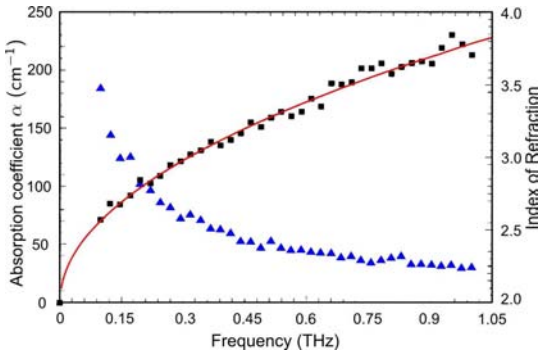

(a) Absorption coefficient α of liquid water

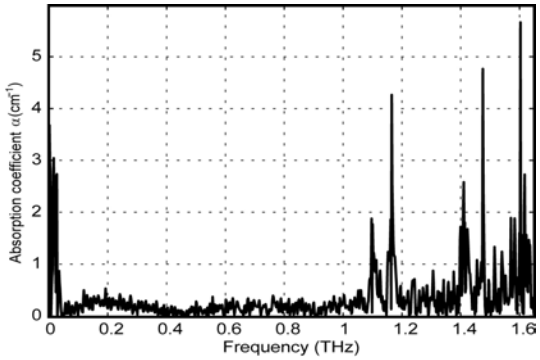

(b) Absorption coefficient α of bulk polyethylene

Figure 4.13: Comparison of α of opaque and transparent materials in the THz frequency range. (a) Values of α for water (■) are typically >100 cm^{-1} at higher THz frequencies, hence water is considered opaque to THz. The index of refraction (▲) is not relevant in this discussion. After Thrane *et al.* (1995). (b) Conversely, bulk polyethylene is considered transparent to THz because of its low α values over most THz frequencies. The spikes on the right of this figure correspond to water lines. The spikes on the left are outside the THz system's usable bandwidth, commencing just above 0.1 THz.

4.5.2 Terahertz Studies of Biomolecules

Strong THz absorption by water has limited the bulk of medically-related THz investigations to dry synthetic samples, such as commercially available powdered proteins. Small quantities of powdered material can be mixed with polyethylene to create enough bulk to make pellets. The range of samples investigated in their powdered/crystalline form has been extensive, although biomolecules have been the major point of interest.

A biomolecule is any type of molecule that is produced by living organisms. This means biomolecules are organic molecules that contain carbon atoms. Other atoms that may be present are hydrogen, nitrogen, and oxygen. Recalling that structures containing these atoms have rich molecular vibrations in the infrared frequency range (Table 4.1), it is expected that similar responses would be present in the THz range. This expectation spurred early investigations using FIR instruments, where it was found that biomolecules (specifically L-amino acids, benzoic acid, dinitrobenzoic acid, urea, hydroquinone, saccharides and polysaccharides) do indeed have many spectral fingerprints from 3–18 THz (Husain *et al.* 1984a, Husain *et al.* 1984b).

More recent investigations using THz-TDS have covered all four major classes of biomolecules: nucleic acids, carbohydrates, lipids and proteins. A summary of work carried out by other authors is as follows (THz-TDS used unless otherwise stated):

Lipids

- safety studies using liposomes; FEL THz source (Doria *et al.* 2004);

Carbohydrates

- polycrystalline and amorphous saccharides (Walther *et al.* 2003);
- vibration of glucose, fructose, sucrose (Nishizawa *et al.* 2003);
- saccharides using CW THz semiconductor laser (Nishizawa *et al.* 2005);

Nucleic acids

- vibrational modes of calf thymus deoxyribonucleic acids (DNA) (Markelz *et al.* 2000);
- label-free probing of DNA binding state (Brucherseifer *et al.* 2000);

- vibrational modes of DNA components: nucleobases and nucleosides (Fischer *et al.* 2002);
- marker free DNA (Nagel *et al.* 2003);
- DNA and polynucleotide (Globus *et al.* 2003);
- differentiating between types of artificial ribonucleic acids (RNA) using spectroscopy and imaging (Fischer *et al.* 2005b);
- dielectric properties of herring and salmon DNA (Parthasarathy *et al.* 2005);
- cytosine, DNA and RNA using CW THz semiconductor laser (Nishizawa *et al.* 2005);

Proteins (repeated groups of amino acids)

- retinal (Walther *et al.* 2000);
- bovine serum albumin (BSA) and collagen (Markelz *et al.* 2000);
- low-frequency protein motions (Mourant *et al.* 2001);
- label free bioaffinity of avidin (protein) and biotin (vitamin B_7 or vitamin H) (Mickan *et al.* 2002d, Menikh *et al.* 2004);
- conformational modes of D96N bacteriorhodopsin (Markelz *et al.* 2002);
- vibrational modes of wild-type and D96N bacteriorhodopsin (Whitmire *et al.* 2003);
- L-glutamic acid (Taday *et al.* 2003a);
- torsional vibrational modes of tryptophan (Yu *et al.* 2004);
- oxidation of cytochrome c (Chen *et al.* 2005);
- crystalline trialanine (Siegrist *et al.* 2006);
- low-frequency dynamics (Yamaguchi *et al.* 2007);
- denaturation of guanidine hydrochloride (Chen *et al.* 2007a);
- dynamical transition (Markelz *et al.* 2007);
- new technique for protein detection: thin metallic mesh (Yoshida *et al.* 2007);
- various amino acids using CW THz semiconductor laser (Nishizawa *et al.* 2008);
- structure and function (Markelz 2008); and
- conformal changes in photoactive yellow protein (Castro-Camus and Johnston 2008).

As evident in this summary, most THz investigations have involved nucleic acids and proteins, which may be due to importance of these two classes of biomolecules in biological function in cells.

Proteins are essentially made up of small structural units that usually contain combinations of the 20 common L-amino acids. These structural units are repeated linearly to form either short chains or large 3D structures (Brown 2000). Regardless of size, the overall structure of a protein molecule—the *tertiary structure*—is unique to that type of protein, and is expected to generate unique THz spectral fingerprints called conformational modes. Figure 4.14 shows examples of simple and complex protein tertiary structures.

NOTE:
These figures are included on page 124 of the print copy of the thesis held in the University of Adelaide Library.

(a) Ball and stick diagram of the amyloid-β protein

(c) Ball and stick diagram of the bacteriorhodopsin protein

NOTE:
These figures are included on page 124 of the print copy of the thesis held in the University of Adelaide Library.

(b) Ribbon diagram of the amyloid-β protein

(d) Ribbon diagram of the bacteriorhodopsin protein

Figure 4.14: Structural differences in biomolecules. Ball and stick, and ribbon diagrams of proteins. Diagrams obtained from the Protein Data Bank, and rendered using Jmol. Colour convention: grey=carbon, white=hydrogen, blue=nitrogen, red=oxygen, yellow=sulphur. (a and b) The amyloid-β protein is considered a small to mid-sized protein based on its molecular weight. It has a simple tertiary structure. After Kohno *et al.* (1996). (c and d) The bacteriorhodopsin protein is a macromolecule with a complex tertiary structure. After Subramaniam and Henderson (2000).

Inside each structural unit of protein, the groups of amino acids are held together by peptide bonds. Hydrogen bonds hold the larger structural units together. These bonds

make most proteins quite flexible, with the propensity to generate unique vibrational modes depending on the size and contents of each structural unit. These vibrational modes give information about the way the structural units are arranged—the *secondary structure* of a protein molecule. Secondary structure is therefore also of interest in THz studies. Additionally, these vibrational modes change when a protein molecule reacts to chemical or environmental changes (e.g. heat), thus THz spectroscopy can be used to study the dynamics of a protein molecule.

The contents and arrangement of structural units in proteins is controlled by a repository of genetic information inside cells; this repository is called deoxyribonucleic acid (DNA) (Avery *et al.* 1944). Enzymes extract information in DNA by copying (*transcribing*) the information into one of three variants of ribonucleic acid (RNA) (Crick 1970). The DNA double helix and the RNA single helix consist of repeated, long and unbranched combinations of five types of nucleic acids: uracil, cytosine, thymine, adenine and guanine. These nucleic acids are linked via alternating units of phosphate and deoxyribose. The double and single helices are the secondary structure of DNA and RNA respectively (Brown 2000). Like proteins, the vibrational modes from the secondary structure of DNA and RNA can be studied using THz spectroscopy. Furthermore, the three variants of RNA—messenger RNA, ribosomal RNA and transfer RNA—with subtly different structures and chemical compositions have been successfully identified using THz spectroscopy and imaging as listed in the summary above.

As a final note, THz spectroscopy has also been successfully applied in distinguishing between the different biomolecule sizes (Chan *et al.* 2004).

Biomolecules in Solution

One point of contention with measuring biomolecules in their dry/crystalline form is that naturally occurring biomolecules exist in solutions, such as in blood. If THz is to mature as a medical diagnostic tool, then the test environment should more closely resemble the natural one.

The interaction of biomolecules in solution is expected to produce THz spectral fingerprints that differ from those obtained in dry environments. Studying protein in solution poses challenges as discussed in Section 4.5.1, where water severely attenuates the transmitted THz signal. If the transmitted THz signal only passes through a thin film of solution, then it is possible to make meaningful measurements with acceptable dynamic range (Jepsen and Fischer 2005).

Several authors have investigated solutions other than water that may be suitable for hydrating proteins. Examples are: an acetonitrile-water mixture Venables and Schmuttenmaer (1998); solvents (Beard *et al.* 2002); electrolyte solutions (Asaki *et al.* 2002); water-dioxane mixture (Mickan *et al.* 2004); and aqueous buffers (Xu *et al.* 2006a). Custom-made sample holders, such as compressed polyethylene bags (Venables and Schmuttenmaer 1998) and cuvettes (Matei and Dressel 2003), have been designed to reduce the sample thickness in the THz path. Commercial liquid sample holders (more commonly known as *liquid cells*) can also be purchased with spacers of assorted thicknesses. Figure 4.15 shows examples of both custom-made and commercially bought liquid cells.

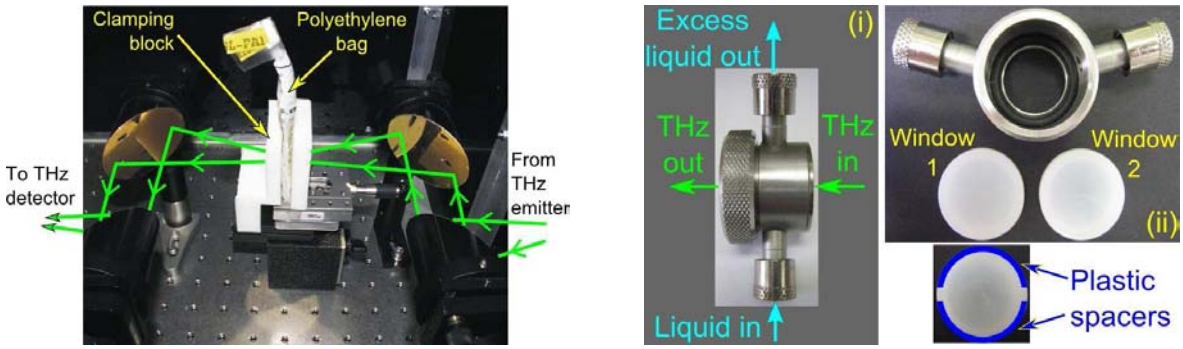

(a) Custom made liquid cell

(b) Commercial liquid cell

Figure 4.15: Examples of liquid cells. (a) Custom made liquid cell based on the design of Venables and Schmuttenmaer (1998). A polyethylene bag is clamped between two polyethylene blocks with a variable gap width. After Mickan *et al.* (2002b). (b) The A140 liquid cell from Bruker Optics. Image (i) shows the side view of the cell including the oversized screw-top lid on the left, which secures two polyethylene windows. Liquid is injected into the lower nozzle (shown capped) with a syringe, and the liquid accumulates between the two windows. Excess liquid flows out from the upper nozzle (also shown capped). THz radiation is directed through the windows as shown by the green arrows. The cell is dismantled in image (ii). Each polyethylene window is 1 mm thick. To create a space of x mm between the windows, plastic spacers (shown in blue) with thickness of x mm are sandwiched between the windows.

Measurements of hydrated DNA (Globus *et al.* 2006) and lysozyme protein (Knab *et al.* 2006, Xu *et al.* 2006b, Xu *et al.* 2006c, Knab *et al.* 2007, Chen *et al.* 2007b) have indeed shown that there is a marked difference between the THz spectra of dry and hydrated biomolecules. In the hydrated environment, some water molecules *adsorb*[50] to the

[50] Adsorbance means adherence. Adsorb differs from absorb.

biomolecules, becoming "bound water." Mathematical models, verified with THz-TDS experiments, have revealed that bound water interacts strongly with biomolecules, hence biomolecules and water molecules cannot be treated as two separate entities. These findings confirm that biomolecules need to be measured in their liquid state if the aim of the experiment is to resemble naturally occurring biomolecules.

More details on the dynamics of water adsorption in the THz frequency range can be found in Grant *et al.* (1978), Mickan *et al.* (2002b), and Zhang and Grischkowsky (2004).

Terahertz Spectroscopy of Unprocessed Whole Blood

The refinement of THz spectroscopic techniques for measuring small quantities of liquids has been advantageous for THz spectroscopy of biological liquid samples, such as blood, which tend to be available in small quantities. Very small quantities of whole blood (Giovenale *et al.* 2003, Scarfí *et al.* 2003, Matei and Dressel 2003) and plasma (Plusquellic *et al.* 2003) have been investigated with THz-TDS. These studies have so far focused on test methodologies, and have compared the THz spectra of blood and water. Identification of biomolecules in whole or centrifuged blood is still not possible because of the extremely small concentrations of biomolecules present (tens of micrograms per millilitre). Most THz experiments utilise several milligrams of biomolecules, hence vast improvements in the sensitivity (i.e. dynamic range) of THz liquid spectroscopy will be needed before micrograms of biomolecules in solution can be successfully probed.

Techniques for Improving SNR of THz Liquid Spectroscopy

One possible technique for improving THz sensitivity is to use thin films (Jiang *et al.* 2000) incorporating modulation that improves the signal-to-noise ratio (SNR) of the measured signal (Mickan *et al.* 2002c, Mickan *et al.* 2002a, Mickan *et al.* 2004, Balakrishnan *et al.* 2009). Sample and reference measurements are made in quick succession in order to minimise the influence of noise from the THz system, hence maximising the weak signal from the liquid sample.

Another technique for improving the SNR is to measure liquid in reflection mode instead of transmission mode. Attenuated total reflection is unaffected by problems pertaining to sample thickness because measurements are made on the surface of the sample (Nagai *et al.* 2006). Alternatively, microfluidic devices comprising very narrow channels (several microns in width) contain minute quantities of flowing liquid. These

channels also act like waveguides in which THz radiation can pass, hence allowing a means of measuring the liquid sample (George *et al.* 2008). Larger waveguide structures have also been employed in the study of biomolecules (Laman *et al.* 2008).

Finally, near-field THz spectroscopy may allow THz to be directed at very close range to biomolecules. This differs from existing THz-TDS that requires samples to be measured in the far-field. Near-field THz spectroscopy has the potential for nano-scale accuracy and resolution, giving THz spectroscopy unprecedented access to capture the nano- and atomic characteristics of biomolecules (Hunsche *et al.* 1998, Mair *et al.* 2002, van der Valk and Planken 2004, Walsh *et al.* 2004, Yuan *et al.* 2005).

In Chapter 7, novel THz-TDS work involving hydrated biomolecules in a frozen state is presented. In Chapter 6, a discussion on the THz response of ice shows that it is transparent to lower THz frequencies (below 10 THz), therefore freezing provides a means for eliminating the adverse absorptive effect of liquid water and improves the SNR of the measured THz signal.

4.5.3 Pharmaceutical Quality Control using THz

Terahertz spectroscopy and imaging has found another niche in the area of pharmaceutical quality control. Terahertz has been applied in the inspection of tablet coatings, particularly enteric coatings which are necessary for the administration of certain drugs into the body (Zeitler *et al.* 2007). Terahertz spectroscopy has also played a part in other important quality control considerations in the synthesis of drugs, such as identifying polymorphism and crystallinity (Taday *et al.* 2003b, Strachan *et al.* 2005), as well as confirming if a chiral drug has been corrupted into a racemic mixture (Franz *et al.* 2006).

Mixtures of drugs can also be mapped with THz imaging and pattern recognition techniques (Fischer *et al.* 2005a, Shen *et al.* 2005b, Shen *et al.* 2005c, Fischer *et al.* 2007). Terahertz spectroscopy can also differentiate between chemicals that are derived from similar sources, such as benzoic acid (a food preservative), salicylic acid (2-hydrobenzoic acid, a plant hormone), 3- and 4-hydrobenzoic acid (derivatives of benzoic acid), and aspirin (Walther *et al.* 2002). An excellent review of pharmaceutical applications of THz is found in (Taday 2004).

The success of THz pharmaceutical applications has led to its application in the detection of illicit drugs (Kawase *et al.* 2003, Woolard *et al.* 2005), microorganisms such as

Bacillus subtilis (Brown *et al.* 2004), and illicit food additives such as triazine, of which melamine is a derivative (Huang *et al.* 2004), sodium bicarbonate and calcium sulphate (Chan *et al.* 2004).

4.5.4 Terahertz Biotissue Studies

Section 1.4 describes numerous examples of where THz-TDS is used in sensing biotissue. Two examples are similar to those covered in IR and microwave spectroscopies, namely skin and tumours. Two other medically related THz applications which have similar applications in IR and microwave are: cortical bone (Stringer *et al.* 2004, Stringer *et al.* 2005), and cells (Ferguson *et al.* 2004, Liu *et al.* 2007). Continuous wave THz techniques have also been employed in the measurement of biotissue (Marx 2002, Nishizawa *et al.* 2008).

Reviews of THz biotissue applications can be found in Kincade (2000), Smye *et al.* (2001), Pepper (2003), and Mallozzi (2003).

Increasingly, THz research is aiming to develop *in vivo* scanning tools for the human body, hence safety considerations pertaining to THz exposure have been investigated and found to be within acceptable limits[51] (Berry *et al.* 2003b).

Problems Involving Excised Biotissue

One issue highlighted in Section 1.4 is the use of excised biotissue in THz studies. As the human body contains around 60% water (Mullins 2001), it is not possible to perform *in vivo* THz spectroscopy or imaging of biotissue located deep inside the body with the current THz power levels and TDS equipment; surgery would be needed to expose the biotissue to the THz radiation, although endoscopic devices that channel THz radiation into the body are starting to emerge as possible solutions to this problem (Lu *et al.* 2008). Another device, based on the THz wand shown in Fig. 1.8, aims to detect residual tumour tissue around the surgical site where a tumour is removed (Ashworth *et al.* 2007). While these instruments are still being developed, *ex vivo* measurements of excised biotissue are still the most common way of analysing samples in the THz research field.

[51] Average beam power for THz scanning imaging systems <1 μW; average beam power with amplification <1 mW. Upper limit in guidelines <3 mW (Berry *et al.* 2003b)

When compared to more established research involving biomolecules, THz biotissue spectroscopy is still a developing research area, hence there are no formalised standards for handling and preserving excised biotissue. Different preservation methods have been reported in existing THz literature: from standard pathological formalin fixing to frozen samples. Every preservation method alters a sample in one way or another, thus it is important to choose an appropriate method for a specific study. For example, cross linking agents such as formalin aim to preserve biotissue by destroying the natural protein enzyme action and digestion process that occurs in decomposition. Formalin cross-links proteins to halt this process and water is removed from the biotissue to further encourage protein denaturation. Consequently, formalin fixed samples are not suitable for studies where the presence of water is important, such as THz protein sensing studies. However, since formalin preserves the histomorphology of biotissue, formalin fixed samples can still provide relevant results when inspected with THz as seen in the example given in Fig. 1.6 (Knobloch *et al.* 2001, Knobloch *et al.* 2002).

Biotissue samples frozen in domestic freezers (slow freezing) no longer retain their protein structures because the process of slow freezing forms ice crystals between cells, resulting in irreversible destruction of subcellular structure. Slow frozen biotissue however may be suited for THz analysis of biotissue density and distinguishing bone-tissue boundaries via THz imaging (Ferguson *et al.* 2002a).

Fresh biotissue most closely resembles *in vivo* conditions as there is minimal structural destruction so, in theory, collective structural responses can be captured in the THz frequency domain to determine the health of the biotissue. Fresh biotissue has been used in a handful of studies to distinguish between organ types based on the different optical properties (Fitzgerald *et al.* 2003, Berry *et al.* 2003a, He *et al.* 2006), for example as shown in Fig. 4.16.

The distinction between optical properties of different types of fresh biotissue means that THz spectroscopy has the potential to identify diseased and healthy biotissue, e.g. previous results based on formalin-fixed biotissue indicate that diseased biotissue has different optical properties from healthy biotissue.

Unfortunately, one particularly important aspect of fresh biotissue lacks discussion in existing literature: biotissue hydration. As discussed previously, water severely reduces the THz signal; water in biotissue will have a similar effect, however its influence depends on how much the biotissue is hydrated during measurements. The level of biotissue hydration may distort THz spectroscopy measurements, resulting in false

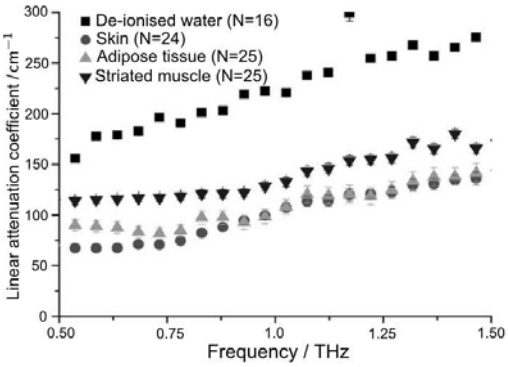

Figure 4.16: Differentiating biotissue in the THz frequency range. Different types of biotissue samples can be distinguished based on their THz optical properties. These properties are distinct from that of liquid water, indicating that the optical properties are due to the biotissue properties rather than water content. After Fitzgerald *et al.* (2003).

interpretation of results, such as optical properties. This is an important consideration because nitrogen that is used to purge the test environment for the purpose of removing water vapour, will inevitably dry biotissue over time.

Two other issues lacking discussion in existing literature are handling and storage conditions of fresh biotissue.

In Chapter 5, novel work involving fresh rat tissue will focus on how biotissue dehydration over an extended time interval affects extracted optical properties. Experimental protocols will be emphasised, including information on how biotissue can be kept fresh from the moment of excision to measurement. The Chapter also proposes a viable solution for overcoming hydration and freshness problems.

In Chapter 6, the transparency of ice in the lower THz frequency range will be discussed. Novel measurements involving snap-frozen human brain biotissue will then be presented as part of the discussion pertaining to the use of THz as a tool for understanding protein plaques that accumulate in the brain in diseases such as Alzheimer's disease.

4.6 Chapter Summary

A thorough review of medical spectroscopy and imaging research in the THz, IR, and microwave frequency regimes have been introduced in this Chapter. It is evident that the breath of medically-inspired IR and microwave research is far wider than those in

the THz regime. The work presented in this Thesis is inspired by existing medical research from all three frequency regimes, hence knowledge will be drawn from the three sources where possible. However, the primary focus on the work presented in Chapters 5–9 is to contribute towards the pool of medical THz knowledge. This endeavour begins in the next Chapter, where the influence of hydration on THz spectroscopy of freshly excised biotissue is investigated.

The use of freshly excised biotissue is a paradigm shift from early THz experiments involving formalin-fixed biotissue or raw/cooked meat (Mittleman *et al.* 1999, Knobloch *et al.* 2001, Knobloch *et al.* 2002). Freshly excised skin tissue, as described in Section 1.4, was first presented in 2002 (Woodward *et al.* 2002). Considered most similar to *in vivo* conditions, fresh biotissue continues to attract and challenge THz researchers who aim to develop an *in vivo* THz diagnostic tool (Ashworth *et al.* 2009). In the next Chapter, these challenges will be discussed and an alternative to freshly excised biotissue is presented.

Chapter 5

Impact of Fresh Biotissue Hydration on Terahertz Spectroscopy

FRESH excised biotissue (as opposed to preserved biotissue) most closely mimics *in vivo* conditions, but high water content in biotissue, coupled with extreme structural pliantness, creates many challenges for handling and measurement. Storage of fresh biotissue is also an important consideration in order to ward off decay before measurements are conducted. During measurements, biotissue dehydration becomes a concern in the nitrogen-purged test environment. The decreasing levels of biotissue hydration result in THz measurements that can be erroneously interpreted as having spectral features unique to specific biotissue types. In this Chapter, novel investigations to monitor the effect of biotissue hydration and freshness on measurements are described. Fresh and necrotic biotissue samples are compared to identify spectral differences. Lyophilisation (freeze drying) is then introduced as a viable solution for overcoming hydration, thickness, freshness, structural-preservation, and handling problems.

5.1 Introduction

"Problems worthy of attack prove their worth by fighting back."

Piet Hein (1905–1996)

Variability of fresh biotissue measurements is one of the biggest challenges facing researchers in this area. As highlighted in Section 4.4.2, an assortment of microwave instruments has been developed to probe biotissue; there is an ongoing quest to find the ideal instrument and technique for measuring biotissue with confidence and ease.

Transmission mode THz-TDS systems are most commonly used in THz research, but their experimental layout is often best suited for samples that are dry and firm, such as pellets. Special holders are needed for samples that may be moist or supple. These holders may interfere with the THz beam and can introduce artefacts, such as etalons, which can only be partially removed using post-measurement data processing techniques.

Another challenge with THz-TDS is high THz absorption by water in a sample. It is noted that this challenge can actually be an advantage in studies that track hydration changes, such as in leaves (Hu and Nuss 1995, Hadjiloucas *et al.* 1999). As discussed in Section 4.5.4, THz measurements have been successfully performed on fresh biotissue samples. These samples need to be sufficiently thin, typically less than 1 mm due to the high absorption coefficient α of liquid water as shown in Fig. 4.13(a). Additionally it is paramount that the hydration in these thin samples is monitored when using a nitrogen-purged THz test environment because sample dehydration is accelerated. This can vastly alter measurements, resulting in incorrect interpretation of results.

The objective of experiments presented in this Chapter is twofold: first to highlight that the establishment of handling and experimental protocols for THz biotissue measurements is paramount because of the fragile nature of the samples; second to propose a solution to hydration issues in the form of lyophilisation.

5.1.1 Motivation

Diagnosing the health of fresh biotissue using THz spectroscopy is a potential application that may complement existing medical diagnostic modalities. However, as discussed in Section 4.5.4, THz spectroscopy of biotissue is still a burgeoning research area with no formalised standard for handling and preserving samples. When compared to

other types of biological materials, such as powders and solutions, biotissue samples are inherently more difficult to handle and prepare due to their supple nature and fast rate of deterioration. This makes it difficult to perform repeatable measurements on biotissue unless some form of preservation is applied to enhance mechanical support within the sample. For example, formalin fixed biotissue as highlighted in Section 4.5.4 gains mechanical robustness, but at the expense of protein content. There is therefore a need to refine fresh biotissue handling techniques, or alternatively find new techniques for preserving biotissue without the need for additives such as formalin.

Availability of biotissue for measurements is another hurdle that researchers need to overcome. Ethics clearance, which is often needed for experiments involving donated human biotissue or sacrificing animals for scientific research, sets constraints on the size of the sample set. In several early bodies of THz research, raw/cooked meat for domestic consumption was used as proof of concept (Mittleman *et al.* 1999). The relatively low cost of meat plus its ease of acquisition and storage make it a convenient sample, but the storage of meat in domestic refrigerators or freezers causes subcellular destruction as highlighted in Section 4.5.4. With only a small pool of available biotissue samples, the establishment of well-defined experimental protocols is paramount so that samples are measured in a consistent manner with the highest possible accuracy.

5.1.2 Objective Summary

This Chapter presents a THz study on fresh rat biotissue. Details of experimental protocols are provided. There is a focus on how biotissue dehydration over an extended time interval affects the frequency responses of samples in the THz frequency range. The changes in the samples are gauged based on their THz *optical properties*, namely their refractive indices and absorption coefficients. A discussion on how biotissue samples can be kept fresh from the moment of excision to measurement is then presented, and a proposal for a viable solution for overcoming hydration and freshness problems is given.

Since THz measurements and data analysis are involved in this Chapter, it is necessary to first formalise the mathematics applied to the measured data for extracting optical properties. With the formalisation complete, the THz study on fresh rat biotissue is then presented from Section 5.3 onwards.

5.1.3 Location of Experimental Work

The experiments described in this Chapter were performed at the Center for Terahertz Research at Rensselaer Polytechnic Institute (RPI) in Troy, New York, USA, during a collaborative visit.

5.2 Terahertz Data Acquisition and Analysis

In this Section, details of how THz signals are measured and analysed are presented. The general THz experimental layout and the mathematics presented in this Section are applicable to the entire Thesis. Details of THz equipment, such as laser model and crystal thicknesses, are specific to this Chapter only.

5.2.1 Terahertz Equipment

An electro-optic, transmission-mode THz-TDS system with a layout similar to that shown in Fig. 3.1(a) is used in this study. Details of the operation of such a system are given in Sections 3.9 and 3.10. For this study, an ultrafast Ti:Sapphire laser from Coherent Inc. (model: Mira 900) emits 100 fs wide pulses at 800 nm wavelength. Terahertz pulses are generated in a 2-mm thick zinc telluride (ZnTe) crystal, and detected by a 1-mm thick ZnTe crystal.

Nitrogen Purging

In order to reduce the negative effects of water vapour in the test environment as described in Section 4.5.1, water vapour needs to be reduced in the environment surrounding all optical components involved in THz generation and detection. This is done by building a well-sealed test chamber that encloses all components before and after the THz emitter and detector, and purging the chamber with dry nitrogen gas. This is shown in Fig. 5.1(a). The nitrogen gas not only keeps the humidity in the THz test chamber below about 3%($\pm$3%), it also ensures the temperature inside the chamber is kept constant (22–23°C) throughout this study. Temperature and humidity levels are monitored using the hygrometer shown in Fig. 5.1(b).

Fig. 5.1(a) shows the THz focal point between the parabolic mirrors where the sample is to be measured. The diameter of the THz focal point varies across THz systems,

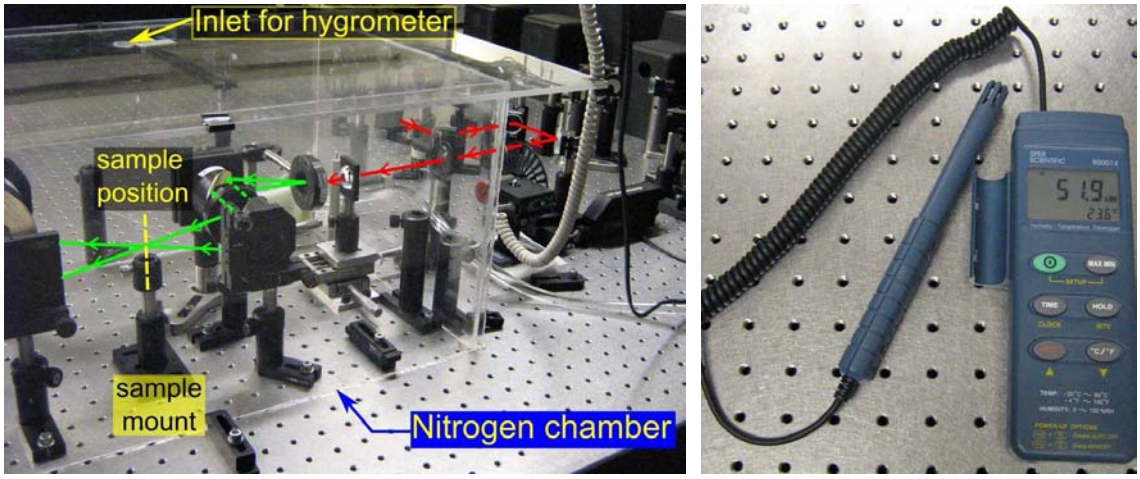

(a) Test chamber for nitrogen purging (b) Hygrometer

Figure 5.1: Nitrogen-purged test chamber. (a) Test chamber encasing optical components involved in the emission and detection of THz radiation. Dry nitrogen gas is piped into the chamber to purge water vapour. Laser pulses enter and exit the chamber through specially made holes in the chamber walls. (b) A hygrometer is used to monitor temperature and humidity levels in the proximity of the sample. An inlet on the lid of the chamber enables the hygrometer probe to be placed close to the sample. Equipment courtesy of X.-C. Zhang at RPI.

ranging from a few millimeters to over 10 mm. The THz focal point in this study is 3 mm. The sample mount that supports the sample is aligned and height-adjusted so that the sample is at the focal point, and the sample's surface is perpendicular to the incident beam.

Types of Measured Signals

Terahertz measurements are recorded from the lock-in amplifier (LIA) via a graphical user interface created with LabView software. Measurements are made in the time domain.

For THz data analysis, both the sample and its reference signal need to be measured. The reference signal is that of the test environment in which the sample is contained. For example, if a sample is suspended in free-space, then the reference is that of free-space. If however the sample is encased in a holder, then the reference is that of the empty holder.

In this study, the reference THz signal $E_{\text{ref}}(t)$ is for the free-space path inside the nitrogen-purged test chamber; the reference signal is therefore also referred to as "nitrogen" in this Chapter. Ten scans of the reference signal are averaged to produce one $E_{\text{ref}}(t)$ measurement, shown by the thick red plot in Fig. 5.2(a). By applying the Fourier transform on $E_{\text{ref}}(t)$, the reference frequency spectrum $E_{\text{ref}}(\omega)$ is obtained, shown by the thick red plot in Fig. 5.2(b). Normalised logarithmic plots are used throughout this Thesis to display the magnitude of the Fourier transformed THz data. Linear plots are used elsewhere unless otherwise stated. The MATLAB software is used to process all time domain data for the purpose of data analysis and graphical visualisation.

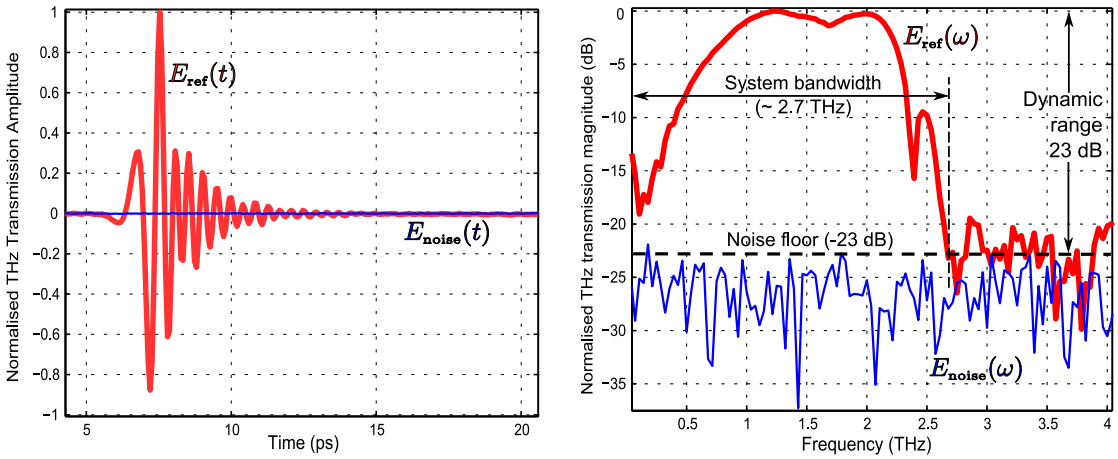

(a) THz signals in the time domain

(b) THz signals in the frequency domain

Figure 5.2: Time and frequency domain representations of THz data. (a) A comparison of the time domain THz signals of nitrogen in free-space (thick red plot) and system noise (thin blue plot) shows that the noise signal stays flat over the course of the measurement, which indicates that the THz system is stable. (b) In the frequency domain, the two signals yield more information about the performance of the THz system. The most important piece of information is the system noise floor because it determines where the measured signal is considered reliable. In this case, measurements that fall below the noise floor at -23 dB are not analysed. This limit is applied to analysis of biotissue sample measurements.

Regardless of the type of reference medium, a sample is immersed in its reference medium such that the THz measurement inherently includes both the sample and reference, hence is denoted as $E_{\text{sample+ref}}(t)$. Like the reference signal, each $E_{\text{sample+ref}}(t)$ measurement is averaged over 10 scans in this study. To extract information about the sample without the influence of the reference medium, data processing of $E_{\text{sample+ref}}(t)$ is needed. The mathematical theory behind the extraction is given in Section 5.2.3.

5.2.2 System Bandwidth and Dynamic Range

It is evident in Fig. 5.2(b) that the signal $E_{\text{ref}}(\omega)$ begins to roll off after 2 THz and eventually stabilises at 3 THz and beyond. Since the signal is decreasing inside this 1 THz frequency range, it is necessary to determine if the signal is reliable for analysis. This is carried out by comparing the THz signal with the system noise $E_{\text{noise}}(t)$ and its frequency equivalent $E_{\text{noise}}(\omega)$.

In this Thesis, system noise is deemed to be the noise that is produced in the probe beam in the absence of any THz signal. As shown in Fig. 5.3, an object opaque to THz radiation (e.g. a copper plate) is placed at a slight angle in the sample position. This ensures that the THz radiation which is reflected off the surface of the copper sheet is directed away from the incident path, hence no THz radiation is reflected back to the THz emitter and probe beam. The signal $E_{\text{noise}}(t)$ is then measured and averaged in the same manner as $E_{\text{ref}}(t)$.

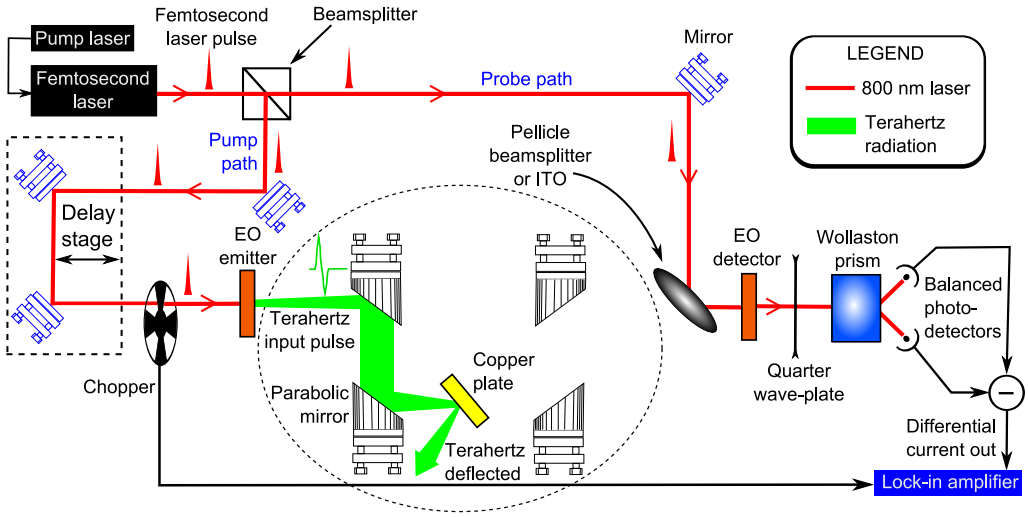

Figure 5.3: System layout for noise measurement. The EO system used in this study has a similar layout to that shown in Fig. 3.1(a). Only the region marked by the dotted boundary is affected when measuring the noise floor. The copper plate deflects the THz beam into free-space away from the EO detector.

The amplitude of $E_{\text{noise}}(t)$ as shown in Fig. 5.2(a) is significantly smaller than $E_{\text{ref}}(t)$. In the frequency domain (Fig. 5.2(b)), $E_{\text{noise}}(\omega)$ manifests as a signal that lies mostly below -25 dB. As a conservative estimate, the noise floor is set at -23 dB, which implies that the system's dynamic range is 23 dB and its usable bandwidth above the measured noise floor is 2.7 THz.

5.2.3 Terahertz Data Analysis

After measuring $E_{\text{ref}}(t)$ and $E_{\text{sample+ref}}(t)$, the signals are processed using the MATLAB software, versions 7.5.0 (release R2007b) and 7.6.0 (release R2008a) by the MathWorks Inc. (MathWorks, Inc. 2010). Details of the data processing steps implemented in MATLAB are provided in Appendix H. Mathematical details of the data processing steps are provided below.

The measured signals $E_{\text{ref}}(t)$ and $E_{\text{sample+ref}}(t)$ are Fourier transformed to give $E_{\text{ref}}(\omega)$ and $E_{\text{sample+ref}}(\omega)$ respectively:

$$E_{\text{ref}}(\omega) = \mathcal{F}\{E_{\text{ref}}(t)\} = |E_{\text{ref}}(\omega)|\, e^{-i[\omega t + \phi_{\text{ref}}(\omega)]} \tag{5.1}$$

$$E_{\text{sample+ref}}(\omega) = \mathcal{F}\{E_{\text{sample+ref}}(t)\} = |E_{\text{sample+ref}}(\omega)|\, e^{-i\left[\omega t + \phi_{\text{sample+ref}}(\omega)\right]}, \tag{5.2}$$

where $\mathcal{F}$ denotes the Fourier transform, $|E_x(\omega)|$ is the magnitude of $E_x(\omega)$, and $\phi_x(\omega)$ is the phase of $E_x(\omega)$.

The THz frequency response of a sample $E_{\text{sample}}(\omega)$ in the absence of the reference medium is extracted from $E_{\text{sample+ref}}(\omega)$ and $E_{\text{ref}}(\omega)$ as follows:

$$E_{\text{sample}}(\omega) = |E_{\text{sample}}(\omega)|\, e^{-i\left[\omega t + \phi_{\text{sample}}(\omega)\right]} \tag{5.3}$$

$$|E_{\text{sample}}(\omega)| = \left|\frac{E_{\text{sample+ref}}(\omega)}{E_{\text{ref}}(\omega)}\right| \tag{5.4}$$

$$\phi_{\text{sample}}(\omega) = \phi_{\text{sample+ref}}(\omega) - \phi_{\text{ref}}(\omega)\,. \tag{5.5}$$

With the knowledge of $E_{\text{sample}}(\omega)$, it is now possible to extract more information about the characteristics of the sample. For example, the sample's frequency dependent optical properties are often of interest. Optical properties usually refer to the sample's refractive index $n(\omega)$ (unitless) and absorption (or attenuation) coefficient $\alpha(\omega)$ (units: cm^{-1}). Each of these two properties can be interpreted individually, however they are often used in unison to determine the presence of spectral fingerprints, which are discussed in Section 4.2.

If a broadband electric field with irradiance $I(\omega)$ is incident on a material that does not absorb any amount of the radiation, then the speed of propagation v of the field through the material as compared to that *in vacuo* is determined by:

$$n(\omega) = \frac{c}{v} = \sqrt{\frac{\epsilon'(\omega)\mu}{\epsilon_0 \mu_0}}\,, \tag{5.6}$$

where $n(\omega) \in \mathbb{R}$, and is also known as the absolute refractive index; c is the speed of light *in vacuo*, $\epsilon'(\omega)$ and μ are the permittivity and permeability of the material respectively, and ϵ_0 and μ_0 are respectively the permittivity and permeability of vacuum.

If the material absorbs some amount of the incident electric field (e.g. polar molecules in Section 4.2 which have resonant frequencies), then the irradiance $I(\omega)$ of the transmitted electric field through the material will decrease according to the Beer-Lambert law:

$$I(\omega) = I_0(\omega)e^{-2\omega\kappa(\omega)d/c} = I_0(\omega)e^{-\alpha(\omega)d}, \tag{5.7}$$

where d is the thickness of the material. Equation (5.7) can be expressed in terms of $E(\omega)$ as follows:

$$\begin{aligned} \text{irradiance } I(\omega) &= E(\omega)E^*(\omega) = |E(\omega)|^2 \\ \text{therefore Equation (5.7) becomes } |E(\omega)|^2 &= |E_0(\omega)|^2 e^{-\alpha(\omega)d} \\ |E(\omega)| &= |E_0(\omega)| e^{-\alpha(\omega)d/2}, \end{aligned} \tag{5.8}$$

where the * symbol denotes the complex conjugate.

Equation (5.8) does not take into account reflections that occur at the interface between the material and the incident medium. In order to account for losses due to these reflections, the Fresnel coefficient $T(\omega)$ is included in Equation (5.8):

$$|E(\omega)| = T(\omega)\ |E_0(\omega)|\, e^{-\alpha(\omega)d/2}. \tag{5.9}$$

For a sample suspended in air,

$$T(\omega) = \frac{4n_{\text{sample}}(\omega)}{[1 + n_{\text{sample}}(\omega)]^2}. \tag{5.10}$$

To incorporate the effect of absorption into the refractive index, the extinction coefficient $\kappa(\omega) \in \mathbb{R}$ is included as an imaginary term. This results in the complex refractive index:

$$\hat{n}(\omega) = n(\omega) - i\kappa(\omega) \tag{5.11}$$

$$= n(\omega) - i\frac{c\alpha(\omega)}{2\omega}, \tag{5.12}$$

$$\text{and } \hat{n}^2(\omega) = \epsilon(\omega) = \epsilon'(\omega) - i\epsilon''(\omega) \tag{5.13}$$

$$\text{where } \epsilon'(\omega) = n^2(\omega) - \kappa^2(\omega), \tag{5.14}$$

$$\text{and } \epsilon''(\omega) = 2n(\omega)\kappa(\omega). \tag{5.15}$$

The derivation of Equation (5.11) in the context of polar molecules is given in Appendix D, where is it shown that Equation (5.13) is equal to:

$$\hat{n}^2(\omega) \;=\; \hat{\epsilon}(\omega) \;=\; \epsilon'(\omega) - i\epsilon''(\omega) \;=\; 1 + \frac{N q_e^2}{\epsilon_0 m_e} \sum_k \frac{f_k}{\omega_{0k}^2 - \omega^2 + i\gamma_k \omega} \,. \tag{5.16}$$

The variables N, q_e, m_e, f_k and γ_k are explained in Appendix D. Where only one resonant frequency ω_0 exists, then Equation (5.16) simplifies to

$$\hat{n}^2(\omega) \;=\; \epsilon(\omega) \;=\; \epsilon'(\omega) - i\epsilon''(\omega) \;=\; 1 + \frac{\text{constant}}{\omega_0^2 - \omega^2 - i\gamma\omega} \,. \tag{5.17}$$

The significance of Equations (5.16) and (5.17) is twofold. First, $\epsilon'(\omega)$ and $\epsilon''(\omega)$ are interdependent on each other, hence cannot be solved separately. This means that $n(\omega)$ and $\kappa(\omega)$ are also related and cannot be solved separately. Second, Equation (5.17) can be represented by the causal susceptibility kernel $G(\tau)$ (Jackson 1975)

$$\begin{aligned} \epsilon(\omega) \;&=\; \epsilon'(\omega) - i\epsilon''(\omega) \;=\; 1 + \int_0^\infty G(\tau)\, e^{i\omega\tau}\, d\tau \\ \text{where}\;\; G(\tau) \;&=\; (\text{constant})^2\, e^{-\gamma\tau/2}\, \frac{\sin(\nu_0 \tau)}{\nu_0}\, \theta(\tau) \,. \end{aligned} \tag{5.18}$$

Since Equation (5.18) is now analytic[52], Cauchy's integral theorem can be applied to relate $\epsilon'(\omega)$ and $\epsilon''(\omega)$. By choosing an appropriate integral contour[53] in Cauchy's integral theorem, the outcome is the formation of the Kramers-Kronig[54] relations (or KK equations) as shown below for $n(\omega)$ and $\kappa(\omega)$:

$$n(\omega) \;=\; 1 + \frac{1}{\pi} \int_{-\infty}^{\infty} \frac{\kappa(\omega')}{\omega' - \omega}\, d\omega' \,, \tag{5.19}$$

$$\kappa(\omega) \;=\; -\frac{1}{\pi} \int_{-\infty}^{\infty} \frac{n(\omega') - 1}{\omega' - \omega}\, d\omega' \,. \tag{5.20}$$

Due to the interdependency of $n(\omega)$ and $\kappa(\omega)$, the KK equations are usually solved using iterative algorithms. One distinct advantage of time domain spectroscopy (TDS), such as THz-TDS, is that $n(\omega)$ and $\kappa(\omega)$ can be calculated without using the KK equations. This is because both the magnitude $|E_x(\omega)|$ and phase $\phi_x(\omega)$ information can be obtained directly by Fourier transforming a THz-TDS measurement $E_x(t)$ as seen in Equation (5.1).

[52] Equation (5.18) is analytic in the upper half ω plane only.
[53] See p. 310 in Jackson (1975) for details.
[54] Named after Hendrik (Hans) Kramers and Ralph Kronig (Kronig 1926, Kramers 1927).

The absorption coefficient $\alpha(\omega)$ can therefore be found by substituting the amplitude $|E_{\text{sample}}(\omega)|$ into Equation (5.9), and utilising Equations (5.3) and (5.10) to give

$$\begin{aligned} |E_{\text{sample+ref}}(\omega)| &= T(\omega)\ |E_{\text{ref}}(\omega)|\, e^{-\alpha(\omega)d/2} \\ \alpha_{\text{sample}}(\omega) &= -\frac{2}{d}\ln\left(\frac{|E_{\text{sample}}(\omega)|\,[1+n_{\text{sample}}(\omega)]^2}{4n_{\text{sample}}(\omega)}\right). \end{aligned} \tag{5.21}$$

The refractive index $n(\omega)$ is found from the phase information $\phi(\omega)$:

$$n_{\text{sample}}(\omega) = \frac{c\,[\phi_{\text{sample+ref}}(\omega)-\phi_{\text{ref}}(\omega)]}{\omega\, d} + 1 = \frac{c\,\phi_{\text{sample}}(\omega)}{\omega\, d} + 1\,. \tag{5.22}$$

The derivation of Equation (5.22) is based on the substitution of the Fresnel equations into the one dimensional wave function $E(z,t)$ propagating along the z-axis. The definition of the Fresnel equations are given in Section D.2.1 and a formal derivation of Equation (5.22) is given in Appendix D.

Dependence of Optical Properties on Thickness

The correct calculations of Equations (5.21) and (5.22) are dependent on the accurate measurement of the sample thickness d. Section 5.4.1 emphasises that sample thickness of fresh biotissue does not remain constant over time due to sample dehydration. Sample thickness is therefore measured in this study either immediately before or after each THz measurement. Referring to Equation (5.21), inaccurate values of d result in plots of $\alpha(\omega)$ having incorrect gradients. This is an important consideration because the gradient of $\alpha(\omega)$ is often the only unique and distinctive spectral property of complex biological systems, such as biotissue, in the THz regime.

5.3 Sample Preparation Techniques

The sample preparation protocols used in this study are presented in this Section. Problems encountered will be highlighted so as to shed light on why the final protocol is adopted.

5.3.1 Fresh Biotissue Excision, Slicing and Storage

Fresh rat biotissue samples used in this study were obtained from routine autopsies unrelated to this study. Since necrosis sets in fairly quickly after excision, it was important to consider how biotissue is stored from the onset of this study. Immediately

after excision, biotissue samples used in this study are submerged in Hank's buffer—a glucose-enriched buffer[55] that can sustain biotissue for a limited period. The buffer is kept cold in a dish seated in a trough of ice. This is shown in Fig. 5.4.

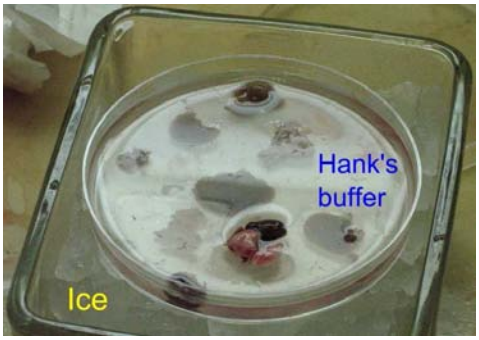

Figure 5.4: Storage of fresh biotissue after excision. Biotissue samples are placed in Hank's buffer immediately after excision. The buffer sits in a trough of ice to ensure optimal freshness of the samples is maintained.

Types of biotissue obtained for this study are diaphragm, kidney (cortex), liver, colon, and stomach. Three other biotissue types—ventral skin, dorsal skin and ventral muscle—are also available, but are excluded from this study because of the poor quality of the samples at various stages of preparation. For example, despite shaving the skin samples, many residual hair follicles still exist. Hair follicles may cause scattering of THz radiation. This issue has resulted in a separate study of scattering by hair-like strands in Chapter 8.

Ideally, all biotissue samples should be cut into slices with uniform thickness. However this is not realistically possible due to handling issues. Diaphragm, colon and stomach samples are used "as is" because they cannot be sliced any thinner in their fresh, supple state. Kidney and liver samples tend to be thicker so several thinner slices are possible.

Slicing Tools

Several earlier trials to slice fresh biotissue with uniform thickness included a vibratome (FHC Inc.), a microtome (IEC), a commercial rodent brain slicer (Braintree Scientific Inc.), and custom made slicers. A microtome holds a blade that is used to slice biotissue with a cutting action analogous to cutting thin slices of meat on a cutting board. A vibratome holds a blade that vibrates to achieve the cutting action. Figure 5.5 shows three of the slicers used.

One millimeter thick slices are preferred as samples can be handled most easily at this thickness. The vibratome works best, but the process of cutting one sample takes several hours and is deemed unsuitable. A custom-built slicer, as shown in Fig. 5.6,

[55] See Appendix C for more details on Hank's buffer.

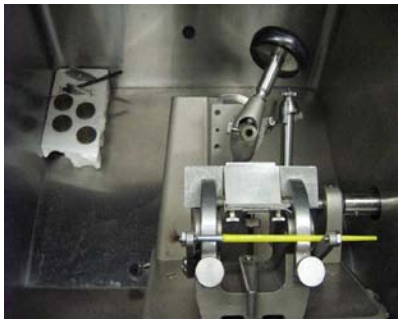

(a) Cryo-microtome

(b) Vibratome

NOTE:
This figure is included on page 145 of the print copy of the thesis held in the University of Adelaide Library.

(c) Rodent brain slicer

Figure 5.5: Examples of commercial biotissue slicing apparatus. (a) Microtome from IEC, shown without blade, is housed inside a cryostat. (b) Vibratome from FHC Inc. shown without actual blade (blade drawn in blue). (c) A commercial rodent brain slicer shown without blades. After Braintree Scientific Inc. (2000).

comprising of two razor blades spaced by a 1 mm washer works surprisingly well and with some practice, slices with relatively uniform thickness are achievable within seconds. The biotissue slices are then re-submerged in cold Hank's buffer and refrigerated with the buffer until the time of THz measurement.

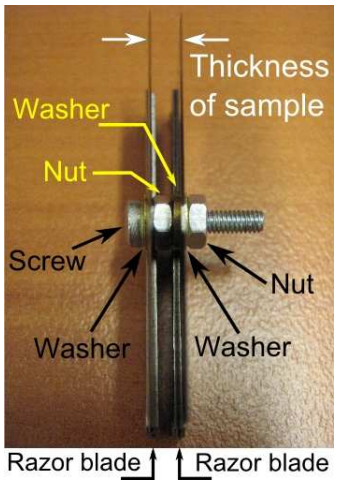

(a) Top view of the slicer

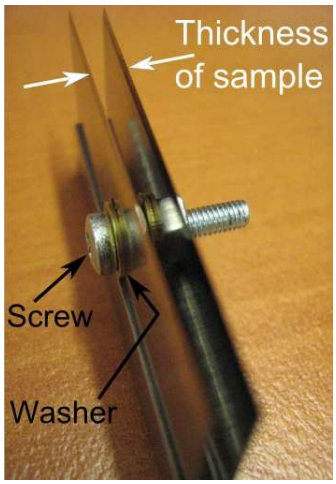

(b) Side view of slicer

Figure 5.6: Custom-built biotissue slicer. A nut is included between the razor blades for illustrative purpose only so that the gap between the two razor blades can be seen clearly. In the study, only a 1 mm washer separates the two blades. External washers and a nut are needed to hold the two blades securely.

5.3.2 Sample Transportation and Priming Prior to Measurements

Fresh biotissue samples are obtained from the Wadsworth Center (New York State Department of Health) in Albany, New York, USA. Sliced samples in buffer are packed in a styrofoam box together with ice packs and transported for 20 minutes to the THz laboratory. Upon arrival, the samples remain in the styrofoam box until the commencement of THz measurement. Ice packs are replaced as necessary.

Each fresh sample is removed from the buffer just prior to measurement and excess buffer is allowed to drip off the sample by tilting the polyethylene plate. The sample is then measured with THz radiation and labelled $E_{\text{sample+ref}}(t)$ as described in Section 5.2.1. To capture any changes in the sample hydration, measurements are repeated for each sample at intervals of between 15 to 20 minutes. This results in a family of $E_{\text{sample+ref}}(t)$ plots over time for each sample. These measurements are presented in the frequency domain in Section 5.4.1.

5.3.3 Mounting Fresh Biotissue for Measurement

A standard THz-TDS system in transmission mode is used in this study. System specification is provided in Section 5.3. The direction of the THz beam is parallel to the optical table, thus samples have to be mounted vertically. It is necessary to design a method of keeping the biotissue slices upright. Commercially purchased petri dishes were used in earlier investigations whereby fresh biotissue slices were mounted by applying minimal amounts of commercial superglue at the edges. Petri dishes were found to be unsuitable because the slices pull away from the surfaces of the dish during measurement, creating air pockets between the slices and dishes. These pockets result in etalon artefacts in the measured THz signal.

Since a biotissue slice is only secured at the edges to the dish, the problem of the slice pulling away from the dish cannot be overcome. This is particularly acute in the middle region of the slice. One alternative is to sandwich the slice between two plates, but without squeezing it out of shape. It was discovered that air pockets still formed between the biotissue and the plate, so this technique was not used.

The ideal scenario would be to measure biotissue samples in air, with only air as the reference. A novel way of achieving this is to make a small hole on each mounting plate, and then sandwich the biotissue slices between the two plates. The middle of

a slice is aligned with the two holes so that the middle of the slice is effectively suspended in air. By ensuring the holes are wider than the THz beam, the beam can pass through the biotissue directly without interference from the plates.

Mounting Plates

Plates are made from 1 mm thick polyethylene sheets (Goodfellow Corporation, high density sheet polyethylene, 0.95 g/cm^3). Each plate is 60 mm by 20 mm in size with a 5 mm diameter hole punched in the middle of each plate. This diameter is larger than the THz beam waist of 3 mm. Polyethylene is chosen because it is stiff enough to keep a biotissue slice in shape, yet pliable enough to be cut easily with scissors and holes can be punched out with a regular office hole puncher. Polystyrene is also trialled but being stiffer than polyethylene, it is very brittle and cracked during cutting and drilling.

The sandwiching technique is initially employed in this study. Elastic bands are used at both ends of the plates to secure the biotissue between the two plates. It is found that the process of sandwiching causes the biotissue to bulge at one of the holes. This is seen in Fig. 5.7. The uneven thickness of the bulge potentially affects calculations of biotissue optical properties, hence this sandwiching method is unsuitable.

An improved technique is to mount the biotissue using minimal drops of commercial superglue at the edges so that only one plate is required. This is the technique employed in this study. Prior to THz measurement, fresh biotissue slices are placed gently on the plates without any visible stretching of the sample, and positioned so that the hole is completely covered by the slice as shown in Fig. 5.8. Minimal drops of superglue are then applied at the edges. It is found that none of the biotissue slices droop into the hole during the course of the experiment, hence all biotissue surfaces are assumed in this study to be reasonably perpendicular to the incoming THz beam.

5.4 Results and Discussion

This Section presents the results of the first part of this study pertaining to changes in biotissue hydration.

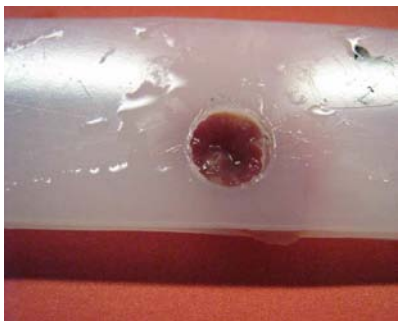

(a) No visible bulge on one side

(b) Bulge on the reverse side

Figure 5.7: Double plate sample holder. Rat kidney sample sandwiched between two 1 mm polyethylene plates with (a) no bulging on one side. (b) severe bulging on the reverse side.

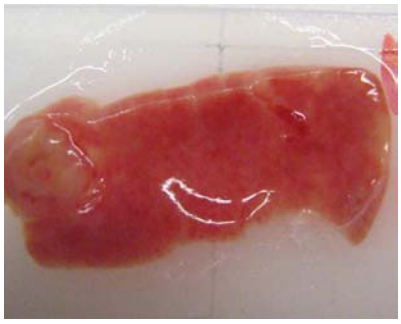

(a) No visible bulge on one side

(b) No visible bulge on the reverse side

Figure 5.8: Single plate sample holder. (a) Rat liver sample covering the transmission hole completely, affixed using superglue. (b) The reverse side, demonstrating the sample remains flat without bulging.

5.4.1 Changes Over Time

Since fresh biotissue samples are stored in buffer prior to THz measurement, they contain very high quantities of water. It is therefore not surprising that the first run of measurements had extremely poor signal-to-noise ratios, resembling that of noise. As highlighted in Section 5.2.2, the noise floor of the THz system is -23 dB; as seen in Fig. 5.9, the magnitude of measured THz transmission signal for the first 20 minutes is buried in this noise floor. The importance of this observation becomes apparent when the absorption coefficient α is calculated.

Fig. 5.10 shows α calculated based on 1 mm thickness. To prevent deterioration of the samples, they were handled minimally so thickness measurements are only taken at intervals when there is a visible changes in a sample's texture, appearance or measured

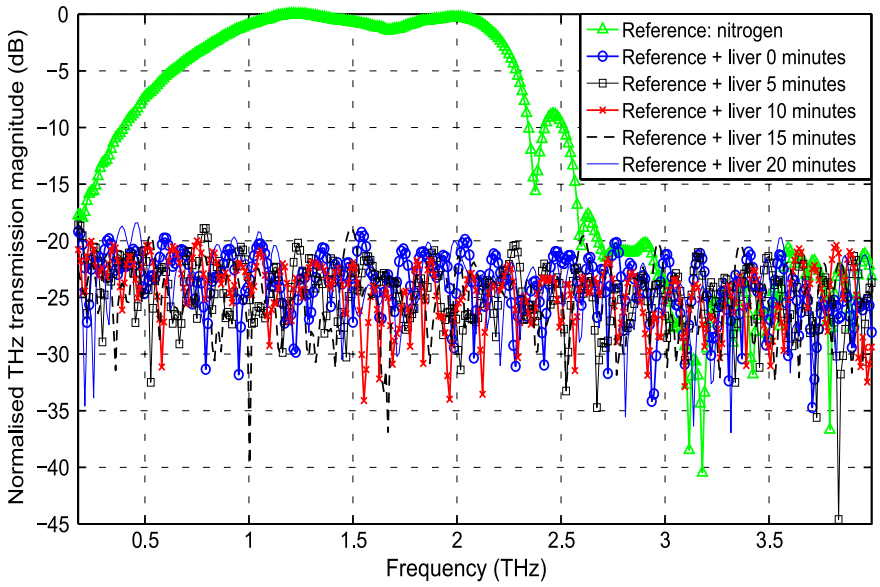

Figure 5.9: Noise floor. Initial THz transmission signal of fresh liver is lost in the noise floor.

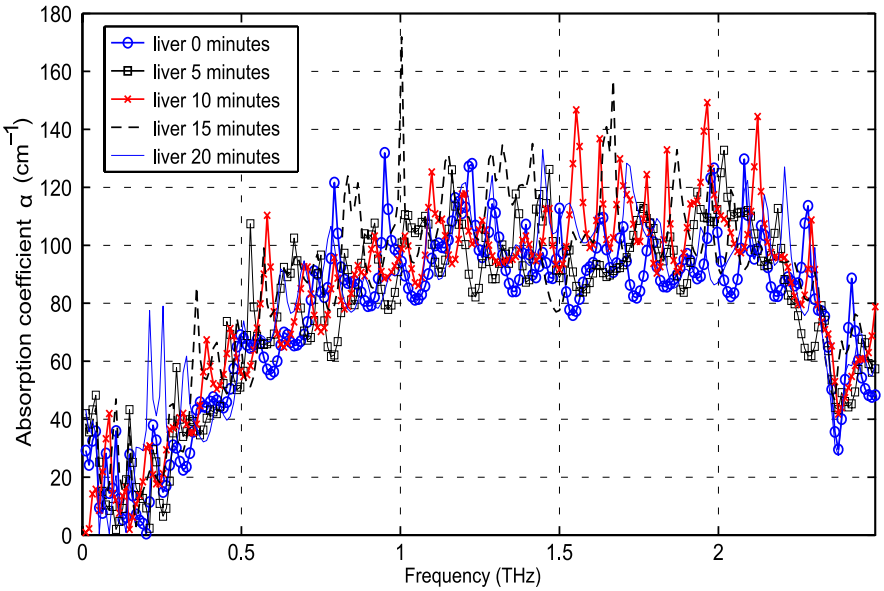

Figure 5.10: Irrelevant α. With the THz transmission signal in the noise floor, the calculated absorption coefficient α is irrelevant.

THz signal. No changes are observed over the first 20 minutes, hence it is assumed that sample thickness remained consistent at 1 mm.

At first glance, these plots of α in Fig. 5.10 do not appear abnormal considering water has similar absorption properties in the THz range (Fig. 4.13(a)). However questions arise when the dynamic range of the measurement is considered. In this study, the dynamic range of the measurement refers to the height of the THz signal above the

noise floor in the frequency domain. This is consistent with that used by Jepsen and Fischer (2005). For the measurement shown in Fig. 5.10, the THz signals are buried under the noise floor at -23 dB, hence the dynamic range is inadequate. This means that α has little meaning in this context (Jepsen and Fischer 2005). Optical properties of fresh biotissue should therefore not be extracted unless the measured THz signal is above the noise floor.

Dehydration of Biotissue in Nitrogen-Purged Atmosphere

Continued exposure of the biotissue sample to the nitrogen-purged atmosphere causes the sample to dehydrate. With less water, the strength of the transmitted THz signal increases, widening the usable THz bandwidth and dynamic range as a result. A comparison of Fig. 5.9 and Fig. 5.11 show a significant improvement in the usable bandwidth and dynamic range after 152 minutes.

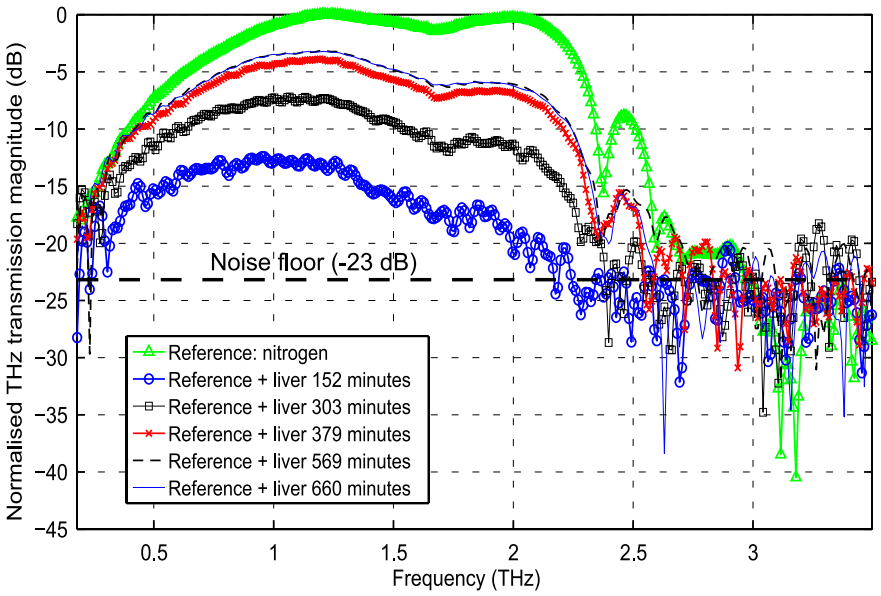

Figure 5.11: Improvement to bandwidth and system dynamic range. Prolonged exposure to nitrogen causes biotissue to dehydrate thus improving the usable bandwidth and system dynamic range. The measurements stabilise after 569 minutes (9.5 hours).

In this study, all moist biotissue samples were intentionally exposed to nitrogen for a prolonged period of time in order to monitor changes in the THz transmitted signal due to the level of biotissue hydration. The rate of dehydration was found to vary according to biotissue type, with denser types such as kidney, colon and diaphragm drying very slowly. This is apparent from Fig. 5.11 and Fig. 5.12 where the measured THz signal of kidney between 0.5–1 THz only rises above the noise floor after 5.5 hours

whereas liver between 0.3–2 THz takes under 2.5 hours to do so. In summary, biotissue samples of similar thickness (when fresh) dehydrate at different rates and their usable THz bandwidths are incomparable.

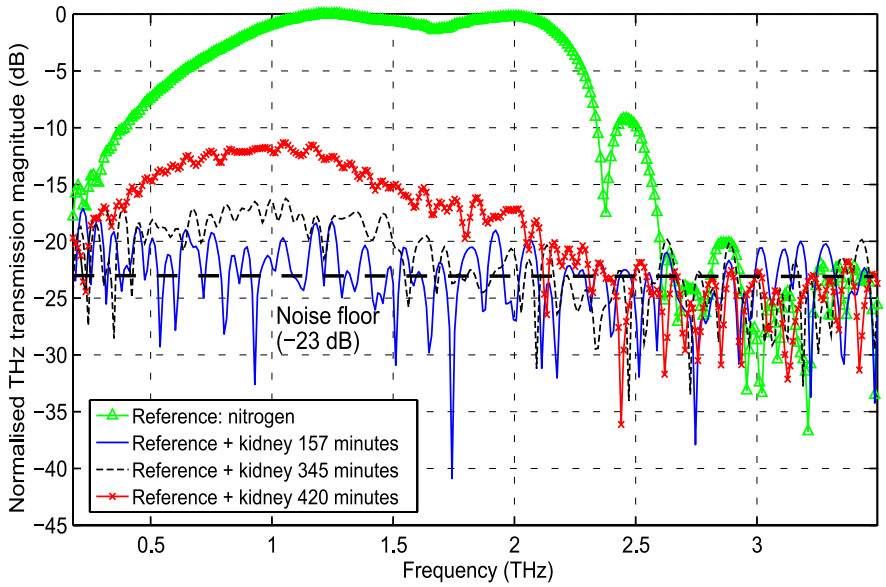

Figure 5.12: Dehydration rates in biotissue. Dense biotissue such as kidney dehydrates slowly. When compared to liver, kidney of the same thickness (when fresh) takes over twice as long to dehydrate.

The extended exposure of biotissue to nitrogen raises questions pertaining to the structural and biological integrity of the samples: do the samples disintegrate as water evaporates? Optical images of one of the liver samples are presented in Fig. 5.13(a) and Fig. 5.13(b). The colour, shape and texture of the sample are possible indicators of biological integrity. It is apparent that the sample retains its shape after 45 minutes, but there is visible shrinkage. With continued shrinkage, the sample develops tears as it pulls away from the edges that were secured to the polyethylene plates with superglue. It is interesting to note that after 10.5 hours, there are still water droplets on the surface of the sample—obvious evidence of the high quantity of water in biotissue. Referring to Fig. 5.11, the improvement in the dynamic range of the measured THz signal converges after 569 minutes (9.5 hours); the rate of dehydration appears to plateau, indicating that removal of the remaining water in the biotissue becomes increasingly difficult over time. Terahertz measurements of biotissue exposed to prolonged air or nitrogen drying will therefore still include the influence of water. This

is another impetus to explore other biotissue preparation methods, such as lyophilisation, that can reduce or remove water from biotissue. Lyophilisation will be introduced in Section 5.5.2.

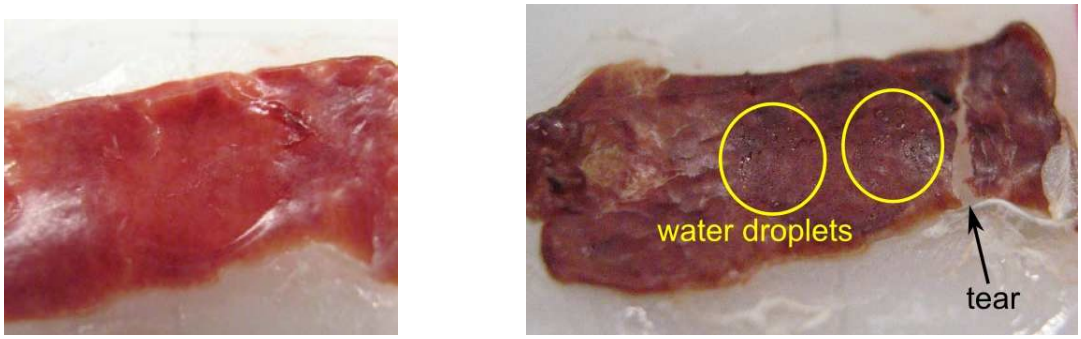

(a) 45 minutes after the first measurement (b) 10.5 hours after the first measurement

Figure 5.13: Visual observation of biotissue dehydration over time. (a) Dehydrated liver sample after exposure in the nitrogen-purged chamber. (b) The sample becomes thin, brittle, and prone to tears. Note that after 10.5 hours, water droplets are still present on the surface of the sample.

5.4.2 Errors in Optical Properties Due to Thickness Variations

In Section 5.4.1, sample shrinkage is highlighted. Shrinkage affects the thickness of samples, which in turn influences the calculated optical properties as shown in Equation (5.9). Sample thickness therefore needs to be monitored. In a study of fresh skin biotissue, sample thickness was maintained through the use of metal spacers (Wallace *et al.* 2006). This technique is tenable if the THz system is fast enough (30 scans per second as reported in their paper). It however does not generalise to longer scanning times, which is necessary for higher signal-to-noise ratio. Wallace *et al.* report a signal-to-noise ratio of 4000:1. Most conventional THz-TDS systems are capable of very high signal-to-noise ratios over 100,000:1 (Zhang 2002) but have scan times of a few minutes, as was the case for this experiment. As borne out from these experiments, spacers may still not resolve our sample thickness issue because spacers are no guarantee against biotissue shrinkage.

Fig. 5.14 illustrates the impact of using an incorrect value for sample thickness on a fresh liver sample that started off with 1 mm thickness. When the frequency response of the sample rises above the noise floor at 152 minutes, the sample's thickness is measured again and found to be 0.3 mm—a significant reduction in thickness. If 1 mm is

used, the incorrect extracted optical properties are considerably lower than the actual values.

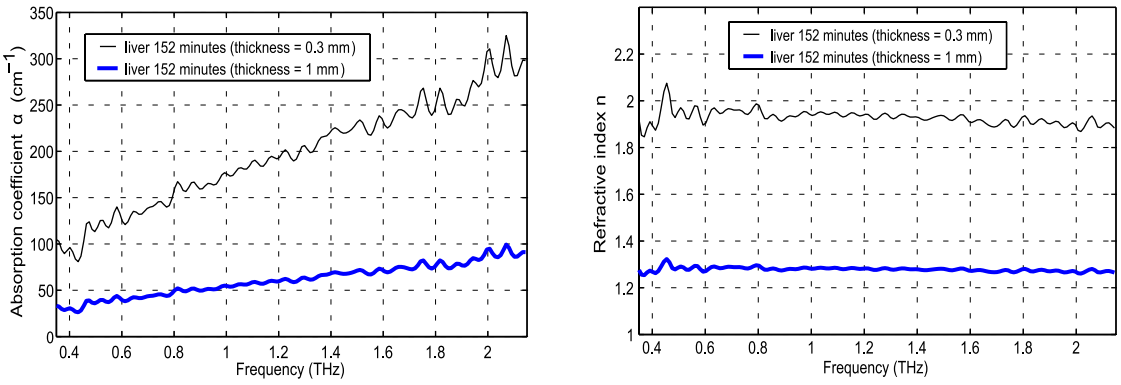

(a) Error limits of extracted absorption coefficient (b) Error limits of extracted refractive index

Figure 5.14: Uncertainties due to changes in thickness. Error in extracted optical properties of liver due to incorrect thickness. The fresh liver sample starts at a thickness of 1 mm and shrinks to 0.3 mm after 152 minutes. The top thin black plots are the correct versions, and the bottom thick blue plots show the incorrect result of assuming constant thickness of 1 mm.

Although it is necessary to monitor sample thickness, repeated contact between the fresh sample and measuring instrument, such as callipers, may accelerate sample deterioration. The supple nature of fresh biotissue also makes accurate measurements of thickness difficult, resulting in large errors in sample optical properties as seen in Fig. 5.14. Post-processing techniques dependent on biotissue optical properties, such as classification, would be severely hindered by these errors. As a biotissue sample dries, its texture changes to one that is more robust to handle, allowing quicker and more accurate measurements of sample dimensions. Sample handling and measurement issues are additional reasons to move toward dry biotissue samples.

5.5 Lyophilisation: A Solution to Biotissue Variability

As seen in Sections 5.3.1 and 5.4, fresh biotissue can be difficult to handle and prepare, whilst variations in hydration level and thickness result in THz measurements that are highly dependent on the duration of biotissue exposure to nitrogen. In this Section, alternative sample preparation techniques that are less susceptible to hydration changes will be introduced, and a possible solution will be presented and compared against results from fresh biotissue samples.

5.5.1 Common Preservation Methods for Biotissue

Two common methods of retaining the "freshness" of excised biotissue are to either immediately fix the sample in formalin and then embed it in paraffin, or snap freeze (rapid freeze) it below -75°C in a refrigerant such as liquid nitrogen, isopentane or isobutane. As mentioned in Section 5.1, formalin fixing may destroy protein structure. Biotissue structure can also be destroyed through slow freezing in a domestic freezer because of the formation of ice crystals in extracellular spaces, resulting in damage to cell membrane and constituents (Gage and Baust 1998, Schäfer and Kaufmann 1999).

Snap freezing of biotissue such as organs, usually involves immersing the biotissue in a cryo-mould containing a freezing medium, such as OCT compound[56] (from Tissue-Tek). The mould is then placed into the refrigerant. The freezing medium, which snap freezes together with the biotissue, provides mechanical support for the frozen biotissue and allows easier handling during slicing with a microtome. Since ice is more transparent to THz than liquid water (Ashworth *et al.* 2006), it is expected that THz signals from frozen samples will have much higher signal-to-noise ratio than that of fresh biotissue. However snap frozen samples thaw quickly at room temperature so samples must be measured inside a cryostat at temperatures below -75°C to prevent repeated thawing and refreezing, which may damage the biotissue samples.

One problem encountered in earlier trials with frozen biotissue is the thinness of slices. In most standard histology analysis, frozen biotissue samples are cut into thin slices with a microtome and mounted on microscopic slides for viewing under an optical microscope. Most microtomes can therefore achieve thicknesses of up to 50 μm—the same order of wavelength in the optical range ($\lambda = 10^{-6}$ m) but three orders less than in the THz range ($\lambda = 10^{-3}$ m). Terahertz measurements from our earlier trials with 20 μm thick sliced frozen samples mounted on polystyrene slides were not successful because the measured sample signal is similar to that of the empty polystyrene slide, hence little information is present. This is expected because 20 μm $\ll 1/\alpha$ (where $1/\alpha$ is the penetration depth of the sample), thus there is insufficient bulk for interaction with the THz signal (Born and Wolf 1999). Microtomes capable of cutting thicker slices exist but were not available for this study.

[56] OCT stands for Optimal Cutting Temperature. The OCT compound is composed of water-soluble glycols, and resins.

5.5.2 Why Lyophilisation?

Fresh samples preserve biological structure but contain high quantities of water whereas frozen samples thaw quickly, making THz measurements cumbersome (e.g. cryostat). One sample preparation technique that can encompass all the benefits of fresh and frozen methods is lyophilisation (freeze drying).

Figure 5.15: Phase diagram of water. Water in a snap-frozen sample prepared at room pressure starts out as ice crystals (*ice phase*) as marked by the blue triangle. When the sample is placed in a low pressure and low temperature environment, ice crystals in the sample sublimate directly from the solid state to gaseous state. This means that water in the sample moves from the ice phase to the vapour phase as marked by the red circle on the phase diagram; the liquid phase is completely bypassed. Lyophilisation therefore provides a means of removing ice crystals in the snap-frozen sample. After Science Education Resource Center (2007).

Lyophilisation involves snap freezing a sample as described in Section 5.5.1 and then placing the sample in a low-temperature (-74°C), low-pressure (or high-vacuum, 10–100 Pa) environment, which as shown in Fig. 5.15, causes ice crystals to sublimate. This process removes a high percentage of water from the sample (reports vary between 90% and $>$ 99% water removal depending on sample type) whilst retaining its structural and molecular integrity.

Lyophilisation is a well established reproducible drying technique for commercial food and pharmaceutical products, thus controlled techniques are well-developed and understood. An advantage of the use of lyophilisation is that standards in its use are defined and assist in maintaining reproducibility over an extended period of time (Thorpe *et al.* 2002, Hymas *et al.* 2005). If biotissue thickness and lyophilisation time

are kept constant, then lyophilised samples will be reproducible. In terms of biotissue integrity after lyophilisation, human blood platelets have been reported to successfully survive freeze drying (Wolkers *et al.* 2001, Tang *et al.* 2006). Biotissue preserved through lyophilisation appears to be ideally suited for THz spectroscopy.

5.5.3 Lyophilising and Mounting Biotissue for Measurement

To prevent the biotissue slices from curling up during snap freezing, it is still necessary to sandwich the slices that are to be lyophilised, but polyethylene plates without holes are used instead. Once sandwiched, the samples are dropped into a bath of isobutane that is seated in dry ice to keep the isobutane at -60°C. After snap freezing, the samples are transferred into a lyophiliser as shown in Fig. 5.16(a) and lyophilised via manifold drying (Fig. 5.16(b)) for 48 hours at -73.5°C, 212 mTorr ($\approx$ 28 Pa). As shown in Fig. 5.15 by the point marked by the red circle, these temperature and pressure settings ensure that water sublimates.

(a) The Virtis Freezemobile 25EL lyophiliser used in this study

(b) Vacuum vials used in manifold drying; test tubes containing biotissue samples are clearly visible

Figure 5.16: Lyophiliser. Manifold drying is used in this study to achieve lyophilisation. Snap frozen biotissue samples sandwiched between polyethylene plates are placed inside test tubes, which are in turn placed inside glass vials with airtight seals. The vials are then attached to the ports of the lyophiliser and dried for 48 hours.

The advantage of manifold drying in a lyophiliser is that the samples in the different vials dry out evenly; in other drying methods (e.g. batch and bulk drying), drying can become less effective in the vials furthest from the vacuum source.

After lyophilisation, the samples are stored in plastic screw cap test tubes that are sealed at the mouth with sealing film (Parafilm), and capped tightly. This is to prevent exposure to moisture which may cause destabilisation because lyophilised materials are hygroscopic. The test tubes are then refrigerated in a domestic refrigerator at $\approx 4^{\circ}$C until the moment of THz measurement.

As evident in Fig. 5.17, lyophilised biotissue becomes stiff and can be mounted with ease in the THz path. To ensure similar conditions for all biotissue types (fresh, lyophilised, necrotic) in this study, lyophilised samples are also mounted on polyethylene plates with holes using superglue at the edges.

(a) Fresh diaphragm (b) Lyophilised diaphragm

Figure 5.17: Visual and physical changes in lyophilised biotissue. Lyophilised biotissue becomes stiff hence is easier to handle than fresh biotissue.

5.5.4 Problems Encountered with Lyophilisation

The only problem encountered in this study involving lyophilised biotissue is that some samples developed cracks as shown in Fig. 5.18. This is likely due to incorrect lyophilisation duration. In an earlier study, samples were lyophilised for 12 hours but were found to be still too moist because their measured THz signals were below the noise floor (Section 5.2.2). In this study, all samples were lyophilised for 48 hours—this could have been too long for certain biotissue types. Cracked samples are not used in data analysis because the cracks may cause scattering or leakage of the THz signal, which will bias results. Recommendations for improvements to the lyophilisation process are provided in Section 5.6.1.

(a) Cracks on one of the lyophilised kidney samples

(b) Cracks visible on the underside of the same sample

Figure 5.18: Rejected lyophilised samples. The cracks in this sample are in the path of the THz signal, making the sample unsuitable for measurement.

5.5.5 Comparison: Lyophilised and Fresh Biotissue

In Sections 5.4.1 and 5.4.2, the impact of hydration changes in fresh biotissue was presented. Dry biotissue was recommended as an alternative to fresh, and THz spectroscopic measurements of nitrogen-dried biotissue were shown to have better bandwidths and dynamic ranges. The duration of nitrogen-drying varied according to the density of the biotissue, affecting the time taken for the improvement in bandwidth and dynamic range to plateau.

For dense samples such as stomach, diaphragm and kidney, the duration of drying required before cessation of improvements in the THz dynamic range can be in the order of several days. Recalling Section 5.5.2, lyophilisation is a quicker and more effective method of drying samples. Lyophilised samples are also easier to handle and measure (Section 5.5.3). Comparing Figs. 5.17 and 5.19, lyophilised biotissue visibly retains more structure whereas nitrogen-dried biotissue appears translucent and paper-like.

Figure 5.19: Nitrogen-dried fresh diaphragm. In addition to thinning and shrinkage, nitrogen-dried biotissue samples appear translucent. In this example, the hole in the polyethylene plate is visible through the sample.

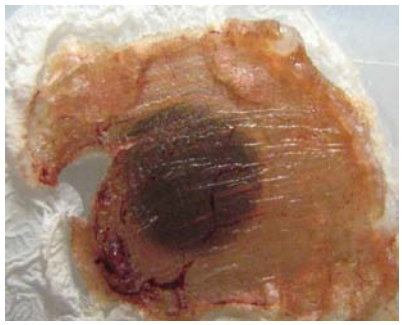

Fig. 5.20 presents the THz absorption coefficient of various biotissue samples in their nitrogen-dried and lyophilised forms. The nitrogen-dried samples are dried until there

are no further observable changes in hydration. The lyophilised samples are measured in their natural form immediately after removal from the test tubes (Section 5.5.3).

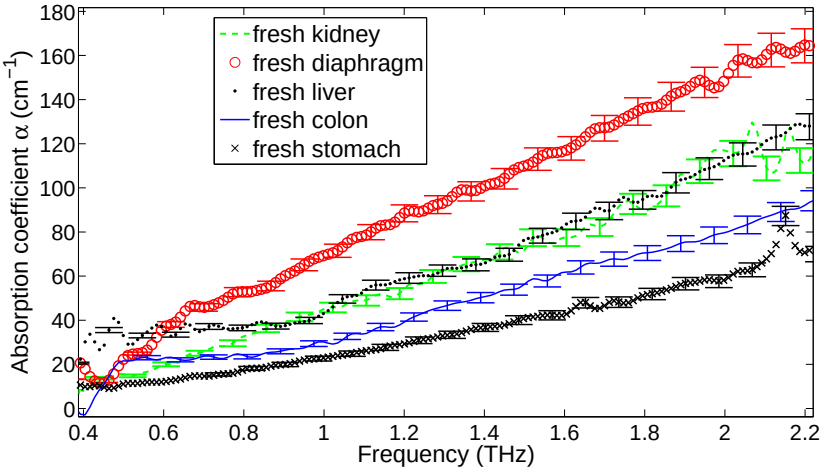

(a) Absorption coefficient α of fresh nitrogen-dried biotissue

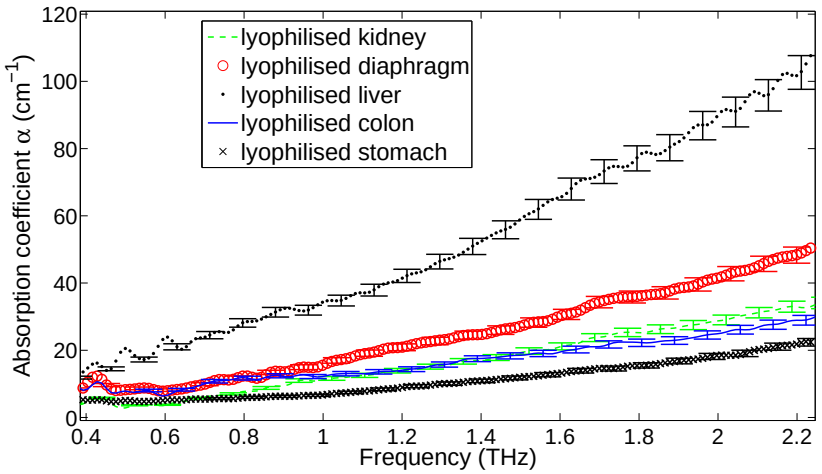

(b) Absorption coefficient α of lyophilised biotissue. Note that the ordinate scale of this figure differs from that of Fig. 5.20(a)

Figure 5.20: Absorption coefficient α of fresh versus lyophilised biotissue. Error bars show the spread of α over a $\pm$ 5% uncertainty in the sample thickness. (a) From 1.7 THz onwards, the α plots of nitrogen-dried samples are noisier than those of the lyophilised samples, indicating reduced THz bandwidth for the nitrogen-dried samples. (b) Wider THz bandwidth of lyophilised samples and distinct separation of the plots at the higher THz range.

With the exception of diaphragm biotissue, there is a lack of differentiability in the THz absorption coefficients of fresh nitrogen-dried biotissue. For example, plots of fresh nitrogen-dried kidney and liver overlap. Errors in the slope of these plots are

unlikely, because the thickness of nitrogen-dried samples can be measured accurately. Nonetheless, the thickness of each sample is averaged over five measurements taken at different points on the sample; error bars are included in Fig. 5.20 to account for a $\pm$ 5% uncertainty in the sample thickness.

As mentioned in Section 5.4.1, the rate of water removal via nitrogen-drying slows down over time. For nitrogen-dried diaphragm biotissue, its high THz absorption is indicative of high residual water content; this is expected as fresh diaphragm, being a type of muscle, is extremely dense thus is expected to dehydrate in nitrogen at a slower rate than the other biotissue types.

Water removal via lyophilisation appears to be effective as demonstrated by the fact that lyophilised diaphragm has lower THz absorption than nitrogen-dried diaphragm. This is also the case for the kidney, colon and stomach samples. However for liver, the absorption is only slightly reduced such that lyophilised liver is left with the strongest absorption of all the lyophilised samples. Since strong water absorption can be ruled out for lyophilised biotissue, one hypothesis for the strong absorption of lyophilised liver is that the incident THz radiation is scattered by the thousands of small units called lobules in liver (Hebel and Stromberg 1986, Standring *et al.* 2005). A similar hypothesis has been proposed by Wallace *et al.* (2006). Therefore, a possible extension beyond this Thesis of the work presented in this Chapter is the reconciliation of THz spectra with biotissue histology.

The gradients from the lyophilised samples differ although not distinctly at the lower THz range. The bandwidth of all lyophilised samples extend beyond 2 THz, whereas the absorption coefficient α plots of nitrogen-dried diaphragm, kidney, and stomach become noisier from 1.7 THz onwards, indicating that the measured THz signals of nitrogen-dried diaphragm, kidney, and stomach have dipped below the noise floor. Therefore, nitrogen-dried diaphragm, kidney, and stomach have reduced THz bandwidths when compared to the lyophilised samples.

5.5.6 Necrotic Samples as a Gauge for Biotissue Freshness

In this study, changes in hydration of fresh biotissue are observed over many hours hence it is necessary to examine a separate batch of control samples to gauge biotissue freshness over time. A third batch of biotissue slices is prepared according to the steps described in Section 5.3.1, but instead of Hank's buffer, this batch is placed in

non-glucose based phosphate buffer (phosphate buffered saline or PBS) to intentionally promote necrosis. The biotissue slices are packed, transported and mounted as described for fresh biotissue in Section 5.3 but are refrigerated with the PBS buffer in a domestic refrigerator until the moment of THz measurement.

5.5.7 Comparison: Necrotic, Lyophilised and Fresh Biotissue

Optical images of fresh and necrotic colon before and after nitrogen-drying are shown in Figs. 5.21(a)–5.21(d). There are visible changes in the colour and texture of necrotic colon. Bad odour is another evidence of necrosis. All necrotic samples in this study have visual and olfactory cues of necrosis.

The THz absorption coefficients of nitrogen-dried, lyophilised and necrotic samples are presented in Fig. 5.22. As highlighted in Section 5.5.6, necrotic samples are submerged in PBS buffer until the time of THz measurements. Like fresh biotissue, necrotic samples contain large quantities of water therefore nitrogen-drying is also required. Necrotic biotissue is similar to fresh biotissue insofar as the nitrogen-drying process is concerned. As seen from Figs. 5.21(b) and 5.21(d), nitrogen-drying causes shrinkage and thinning in both fresh and necrotic biotissue whereas lyophilised biotissue shown in Figs. 5.21(e) and 5.21(f) retains much of the original shape and texture of fresh biotissue.

With the exception of stomach, there are clear differences between the THz absorption of nitrogen-dried fresh and nitrogen-dried necrotic biotissue in Fig. 5.22. This is encouraging as it may indicate that *(i)* Hank's buffer has successfully sustained the fresh biotissue used in this study (this indication is further supported by the absence of olfactory cues as highlighted above), and *(ii)* fresh biotissue does not become necrotic during the nitrogen-drying process. Nitrogen-dried fresh biotissue is therefore still suitable for THz spectroscopy after the prolonged drying time.

Terahertz absorption of lyophilised biotissue appears to be similar to that of nitrogen-dried necrotic biotissue, which could either indicate that lyophilised biotissue has become necrotic or that necrotic biotissue becomes drier than fresh biotissue when exposed to nitrogen. Necrosis is unlikely to have developed in lyophilised biotissue given its minimal water content plus the storage conditions used in this study. The low THz absorption of necrotic biotissue could be due to protein denaturation, which

alters water binding capacity, resulting in dryer samples. However discussion of the histology of necrotic biotissue is outside the scope of this study.

5.6 Conclusion

This study has presented lyophilisation as an alternative to using fresh biotissue for THz spectroscopic measurements. Problems with handling fresh biotissue are highlighted and shown to contribute to large errors in calculation involving biotissue thickness. The high water content of fresh biotissue also creates time variability in the THz bandwidth and dynamic range. Complete water removal via nitrogen-drying gets progressively difficult and residual water is inevitably included in THz spectroscopic measurements of nitrogen-dried fresh biotissue. Ease of handling, fast and effective removal of water, structural and freshness preservation are benefits of lyophilisation.

With improved protocols for sample handling and lyophilisation, together with complementary information from fresh biotissue and histology, lyophilised biotissue may help move us several steps closer to fully understanding THz interaction with biotissue.

5.6.1 Future Work

As highlighted in Section 5.5.4, cracks formed in a few lyophilised samples. Further investigation is needed to explore optimal lyophilisation durations for specific biotissue types and if possible, quantify biotissue hydration. Monitoring changes in sample weights before and after lyophilisation (as well as before and after THz measurements) may be a good technique for tracking biotissue hydration.

In Sections 5.5.5 and 5.5.7, reconciling THz spectra with biotissue histology is proposed as one focus of future studies. As discussed in Section 5.5.1, histological studies tend to be conducted using formalin fixed samples mounted on microscopic slides. To incorporate formalin fixed samples into this study, samples will need to be divided into four: fresh, lyophilised, necrotic and fixed. When improved lyophilisation techniques are established such that good and consistent quality lyophilised biotissue are produced, then lyophilised biotissue can be compared with confidence against formalin fixed samples.

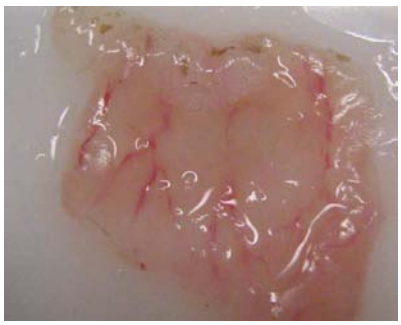

(a) Freshly excised rat colon: note the hole in the polyethylene plate behind the sample cannot be seen

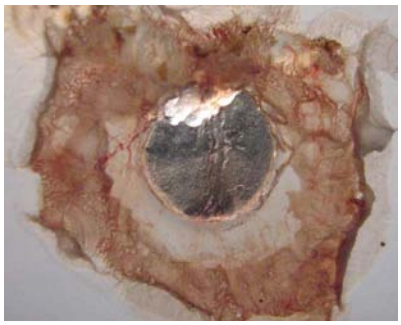

(b) Nitrogen-dried fresh rat colon: the hole in the polyethylene plate behind the sample can now be seen because of the sample's translucency

(c) Necrotic rat colon showing turbid discolouration and texture; the hole in the polyethylene plate behind the sample cannot be seen

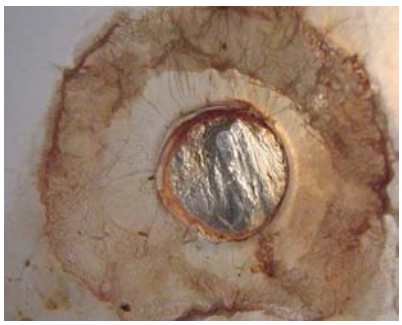

(d) Nitrogen-dried necrotic rat colon: the hole in the polyethylene plate behind the sample can now be seen because of the sample's translucency

(e) Lyophilised rat colon: the sample is opaque and retains much of the shape and thickness of fresh colon. Some shrinkage is visible but of less severity than for the nitrogen-dried samples

(f) Lyophilised rat colon viewed from underside: biotissue structure is retained as seen by the fibres in the sample

Figure 5.21: Optical images of rat colon samples. (a–d) Shrinkage and thinning in both fresh and necrotic biotissue due to nitrogen drying. (e–f) Biotissue structure is remarkably preserved in the lyophilised samples.

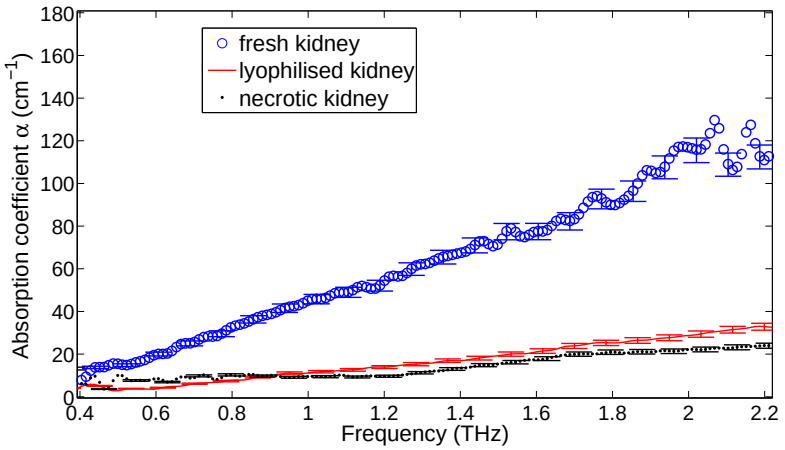

(a) Nitrogen-dried fresh, lyophilised and nitrogen-dried necrotic rat kidney

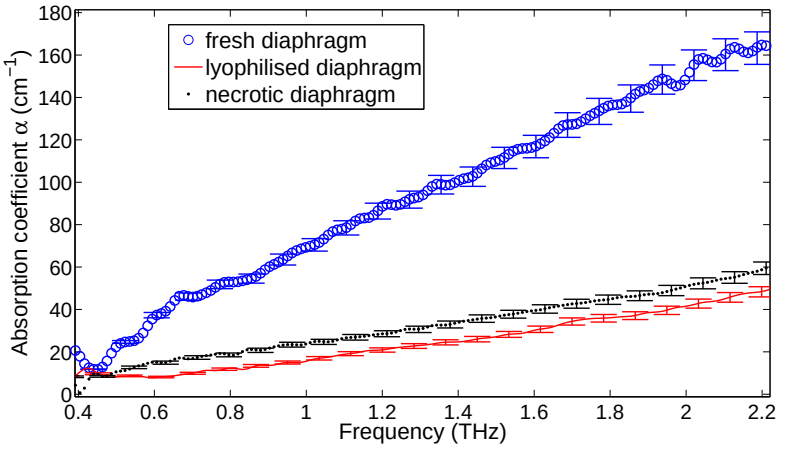

(b) Nitrogen-dried fresh, lyophilised and nitrogen-dried necrotic rat diaphragm

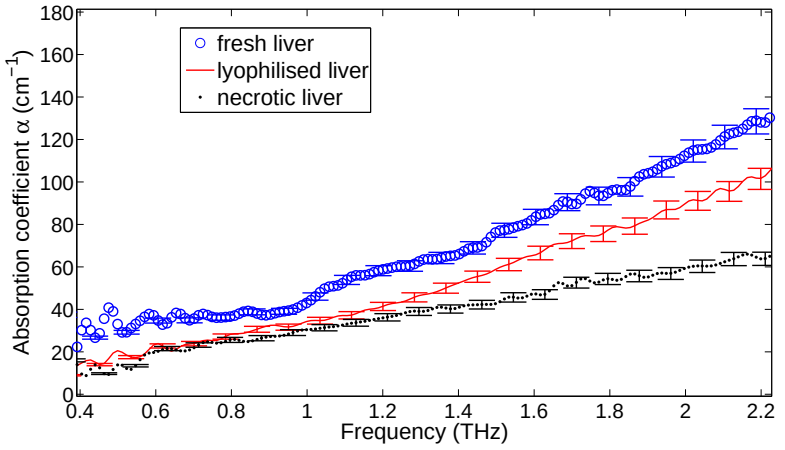

(c) Nitrogen-dried fresh, lyophilised and nitrogen-dried necrotic rat liver

Figure 5.22: Terahertz absorption coefficients α of nitrogen-dried fresh, lyophilised, and nitrogen-dried necrotic samples. Error bars show the spread of α over a $\pm$ 5% uncertainty in the sample thickness. Caption continued overleaf.

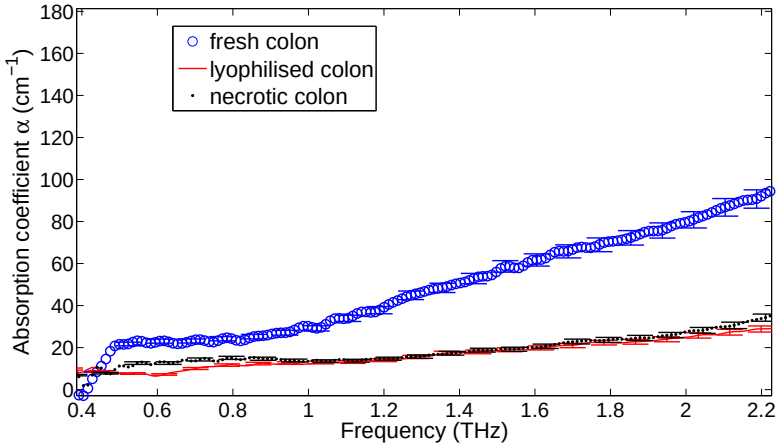

(d) Nitrogen-dried fresh, lyophilised and nitrogen-dried necrotic rat colon

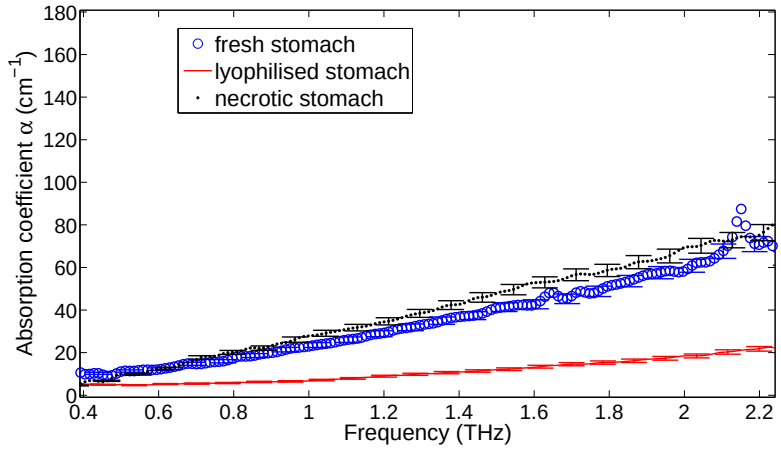

(e) Nitrogen-dried fresh, lyophilised and nitrogen-dried necrotic rat stomach

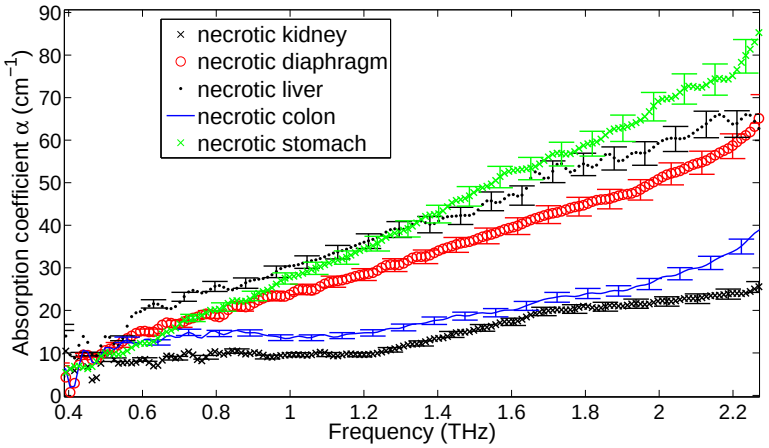

(f) All nitrogen-dried necrotic rat tissue samples

Figure 5.22: Terahertz absorption coefficients α of nitrogen-dried fresh, lyophilised, and nitrogen-dried necrotic samples (continued). This Figure is continued from the previous page. Error bars show the spread of α over a $\pm$ 5% uncertainty in the sample thickness. All samples, with the exception of stomach, show clear differences in THz absorption between nitrogen-dried fresh and nitrogen-dried necrotic biotissue.

5.7 Chapter Summary

The experimental investigation in this Chapter demonstrates the importance of establishing protocols for measuring fresh biotissue. Results from fresh biotissue measurements show that it is easy to misinterpret data due to high water content in the samples. An alternative to fresh samples is proposed in the form of lyophilised biotissue. Lyophilisation avoids problems arising from variability in hydration, thickness, freshness and structure. Additionally, lyophilised biotissue samples are easier to handle and mount than supple fresh ones. Lyophilisation is therefore a viable option for THz spectroscopic studies of biotissue.

Another possible alternative to fresh biotissue samples are snap-frozen ones. Frozen biotissue is, in theory, ideal because the strong THz resonant activity of liquid water is suspended when frozen (Ashworth *et al.* 2006), improving confidence that any resonant activity detected with THz radiation is caused solely by characteristics of the biotissue. Snap-frozen biotissue has the added advantage of containing smaller ice crystals than those in slow-frozen biotissue (frozen in a domestic freezer), thus snap-frozen biotissue samples are expected to suffer from less THz scattering. Furthermore, snap-frozen biotissue retain their shape if they are measured in conditions similar to their storage environment, making them less prone to the cracking encountered by lyophilised biotissue (Section 5.5.4).

These combined benefits of snap-frozen biotissue result in less uncertainties in THz measurements, making snap-frozen biotissue suitable for applications that aim to reveal the unique collective vibrational modes of a specific biotissue. In the next Chapter, one such application is presented. Healthy and diseased snap-frozen brain tissue are examined with THz spectroscopy. Experience gained from the study of fresh and lyophilised biotissue in this Chapter is utilised in the handling and measurement of snap-frozen biotissue. Results show some distinction in the THz absorption spectra, which could be attributed to pathological changes in the diseased tissue.